HYDRODYNAMIC FORCES ON STREAM-CROSSING BRIDGES – CONSIDERATION OF FLOW PARAMETERS, BRIDGE GEOMETRY, AND DEBRIS

By

Shah Md Imran Kabir

Dissertation

Submitted in partial fulfillment of the requirements

for the degree of Doctor of Philosophy at

The University of Texas at Arlington

May 2022

Arlington, Texas

Supervising Committee:

Habib Ahmari, Supervising Professor

Nick Fang

Michelle Hummel

Frank K Lu

ABSTRACT

This thesis examines the interaction of flood flow with bridge superstructures by considering the effects of the flow parameters, bridge geometry, debris, and bridge substructures. The hydrodynamic forces are expressed by using force and moment coefficient charts to portray the effect of bridge submersion, bridge position with respect to the channel bed, flood velocity, and bridge geometry.

Of the 580,000 bridges in the United States, 83% span streams and rivers that may subject them to floods and debris loads. Although bridges are designed to withstand hydrodynamic forces, the most frequent causes of failure are attributed to hydraulic events, including floods, debris, and drifts. The flood-induced hydrodynamic forces cause shear and overturn on bridge decks and may cause them to fail; therefore, the ability to resist hydrodynamic forces is a key factor in the design and construction of safe bridges.

Laboratory bridge models were developed to investigate the range of submergence (inundation ratio, h^*), flood velocity (Froude Number, Fr), and proximity to the channel bed (proximity ratio, Pr) of hydrodynamic force coefficients of bridge superstructures. The effects of the bridge geometry (i.e., width, height, and shape) were studied to determine their influence on the hydrodynamic force and moment coefficients and revealed that there were minimal to no effects on the drag coefficients (C_D), lift coefficients (C_L), and moment coefficients (C_M) when a proximity ratio of 3 or greater was selected. The experimental results revealed that an increase in Fr slightly reduced the force and moment coefficients, especially near the partially-inundated-to-fully-inundated transition ($h^* = 1$). It was also observed that the coefficients of drag, lift, and moment was significantly affected by the inundation ratio (h^*), especially in the transition from partially-

to fully-submerged states, i.e., $h^* = 0.75 – 1.25$. The experimental results showed that the force and moment coefficients can be affected by the width of the deck (aspect ratio, *Ar*), the height of the deck (blockage ratio, *Br*), and shape of the bridge superstructure.

Flow visualization, using the particle image velocimetry (PIV) technique, was used to investigate the flow structures of submerged and partially submerged bridge superstructures. Features of flow kinematics such as flow separation lines, reattachment points, wake width, and reattachment length were investigated in detail and correlated to the trends of hydrodynamic force coefficients. The drag force coefficients were directly proportional to the width of the wake region, and the lift force coefficients were dependent on the difference between the length of the flow separation at the top and bottom of the deck.

An attempt was also made to investigate the effects of debris and the presence of substructures on force coefficients. For this purpose, experiments were performed with two types of debris: flat plate and wedge debris. The results indicated that flat plate debris increased the drag force coefficients significantly, and wedge debris increased the overturning moment and moment coefficients. The results of the substructure model showed that the hydrodynamic force coefficients were conservative for partially submerged cases but not for fully submerged cases. This knowledge and understanding will help to create improved guidelines and standards for designing river-crossing bridges. Lessons from this study can be applied to the design of resilient bridges, retrofit of existing bridges, and more.

ACKNOWLEDGMENT

I am extremely grateful to my supervisor Dr. Habib Ahmari for accepting me into the graduate program and guiding me throughout my PhD program. This journey would not be possible without his constant motivation, encouragement, and guidance. I would also like to thank the members of my dissertation committee, Drs. Nick Fang, Michelle Hummel, and Frank Lu, for their valuable comments. In addition, I am grateful to Dr. Shih-Ho Chao, Maxfield Dean, Qazi Ashique Mowla, Fahad Pervaiz, Bhupendra, Mohammed Qays and my friends from other labs at UTA for their support during the experimental stage. Mr. Qays deserves a handful of thanks not just from me but from all the graduate students in the hydraulics and fluid mechanics lab.

A major portion of the material is based on work supported by the Texas Department of Transportation (Grant: 0 - 7068). Their support is gratefully acknowledged.

I must express my gratitude to my wonderful parents, brother, and family members for all their support and encouragement. Particularly, I would like to give credit to my mother, Nargis Begum, who sacrificed a great deal to see me where I am today, together with my aunt, Shamima Begum, who taught me the importance of education at a very young age.

Lastly, my wife, Fahmida Tasmia, deserves a special recognition. Without her, I would not have been able to complete this journey. My sincere thanks to my wife for always being by my side, pushing me to be the best that I can be. Furthermore, her family in Bangladesh has also been of great assistance during this journey. My PhD journey has been made more memorable by the wonderful friends I have made here in Arlington. Thanks to all of you.

DEDICATION

This work is dedicated to the two most important persons in my life, my mother and my wife.

CO-AUTHORSHIP

This thesis is part of the work conducted by the author to satisfy the requirements for a Ph.D. in civil engineering and includes performing laboratory experiments, analyzing data, examining research results, and preparing the material for manuscripts. Dr. Habib Ahmari supported and supervised the research, which resulted in the following manuscripts, with co-authorship as stated below.

- Journal Papers

Thesis Chapter	Title	Authors	Status
2	Experimental Study to Investigate the Effects of Bridge Geometry and Flow Condition on Hydrodynamic Forces	Kabir, S.M.I., Dean, M., Ahmari, H.	Submitted
3	Investigation of Flow Dynamics Around Submerged Bridges	Kabir, S.M.I., Mowla, Q.A., Ahmari, H.	Not submitted
4	Contribution of Debris and Substructures to Hydrodynamic Force on Bridges	Kabir, S.M.I., Ahmari, H.	Not Submitted

TABLE OF CONTENTS

LIST OF FIGURES

LIST OF TABLES

CHAPTER 1

INTRODUCTION

1.1 MOTIVATION

Floods are by far the most destructive natural disaster to infrastructure and affect the largest number of people (Nasim 2019). Stream crossing bridges are integral components of roadway infrastructure, and their design and construction have an impact on the efficiency of highway designs, the safety of travel, and the quality of the environment. Transportation infrastructures are responsible for moving people, goods, and services in urban areas, as well as ensuring connectivity within and between them, and when the system fails, it negatively impacts the local economy, evacuation procedures, and recovery efforts (Pregnolato et al. 2021).

River floods, especially flash floods that are caused by heavy and localized rain and are often accompanied by artificial and natural debris, pose a threat to river bridges (Kabir and Ahmari 2020). After a bridge deck has become submerged by fast-moving water, it is common for the bridge to collapse partially or completely (Oudenbroek 2018). Because of the complex configuration of bridges, their interaction with flood flow is a complicated physical phenomenon that involves hydrodynamics, overturning, and hydrostatic loads (Fang et al. 2018). Therefore, accurate estimation of flood-induced hydrodynamic loading is crucial for designing bridges and evaluating their vulnerability (Turner 2015).

In the U.S., the state and municipal departments of transportation (DOTs) design bridges, using manuals and guidelines provided by professional organizations and the government, such as the American Association of State Highway and Transportation Officials (AASHTO) (Flint et al.

2017). Several studies have indicated that the AASHTO Load and Resistance Factor Designs (LRFD) and other traditional methods of calculating hydrodynamic forces estimate the flood loading by considering constant coefficients for flood forces (Jordan 2015, Almarsi and Moqbel 2017). Results from physical and numerical modeling of hydrodynamic forces on river-crossing bridges, however, indicate the dependency of these coefficients on flow parameters such as inundation ratio, Froude number, proximity ratio, blockage ratio, etc. (Jempson 2000, Malavasi and Guadagnini 2003, Oudenbroek et al. 2018).

The characteristics of flow around a bridge superstructure are significantly affected by its length and height in the flow direction. Several researchers have shown that the geometry (i.e., width and height) of a rectangular cylinder affects the mean flow field and hydrodynamic forces (Malavasi and Guadagnini 2007, Chu et al. 2016, Thai 2019); nevertheless, force coefficients of a simple bluff body such as a rectangular cylinder cannot be applied to bridges with complex geometry. It has also been reported that the shape of bridge girders and the gap between them influence flow characteristics and hydrodynamic forces (Kerenyi et al. 2009, Kosa 2014, Matsuda 2001, Chen et al. 2014). To the author's knowledge, no study has comprehensively investigated the effects of flood flow by considering variations in bridge geometry and accounting for the complexity of the hydrodynamic forces to which the bridge is subjected. Moreover, the study of flow characteristics on actual bridge geometry is rarely addressed in the literature.

Flooded bridge superstructures are subject to pressurized (orifice) flow under the bridge deck and free (weir) flow over it. Under certain conditions, the flow may separate because of an obstruction (e.g., deck, girders, piers, etc.), and vortices of different sizes may appear along the bridge deck. A wake zone or blockage is produced by these separated boundary layers (Jempson 2000). The vortices generated in gaps between girders induce a local minimum pressure, leading to flow

instability and wave motions that make the largest contribution to hydrodynamic loading (Lin et al. 2012, Naudascher and Medlarz 1983). A strong correlation was observed between the flow pattern and the force coefficients around a circular or rectangular cylinder in free-surface flows (Malavasi and Blois 2007, Zhu et al. 2000), but the relationship between the mean flow pattern and the force coefficients on inundated bridge decks is yet to be discovered.

The existing literature on hydrodynamic forces on bridge decks is comprehensive but lacking in consideration of the effects of debris and substructures on superstructures' force coefficients. Prior works focused on substructures and superstructures separately (Oudenbroek et al. 2018); however, the presence of debris and substructures around a bridge deck made it challenging to accurately determine the force and moment coefficients.

1.2 BACKGROUND

Bridges are designed to withstand flood and debris loads; however, it has been reported that floods and bridge scour have caused more than 60% of the bridge failures in the U.S. (Hunt 2009, Ahamad et al. 2020). When flooding occurs during high flow events, bridges may become completely submerged or partially submerged, and flooding imposes considerable hydrodynamic forces on them, causing them to shear and overturn. Over the past 30 years, numerous bridges have been damaged by flooding in the U.S. and worldwide (Wardhana and Hadipriono 2003, Sousa and Bastos 2013, Taricska 2014, Fechter 2015, Byrne 2019).

According to the Structures Division of the New York State Department of Transportation and the National Bridge Failure Database, from 1966 to 2005, there were at least 1,502 documented bridge failures (Hunt 2009). Wardhana and Hadipriono (2003) investigated the history and causes of bridge failures in the U.S. and found that 503 bridges of various types failed between 1989 and

2000, Taricska (2014) reported a total of 329 bridge failures in the U.S. from 2000 to 2012, and Lee et al. (2013) investigated the causes of bridge failure in the U.S. from 1980 to 2012 and indicated that flood forces are the predominant reason for failure, although scour, overload, collision, internal forces, environmental degradation, fire, and earthquakes are also responsible (Fig. 1.1). Bridge failure can also be attributed to structural deficiencies and faulty connections between the superstructure and substructures (Wardhana and Hadipriono 2003, Padget et al. 2008).

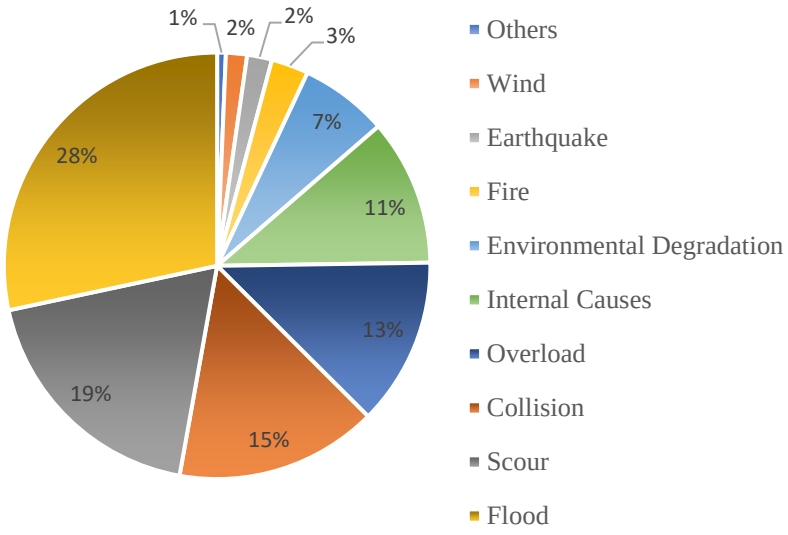

Fig. 1.1 Causes of bridge failure in the U.S. for the years from 1980 - 2012 (adapted from Lee et al. 2013)

According to the American Association of Civil Engineers' (ASCE) Infrastructure Report Card 2021, almost 42% of all bridges in the United States are 50 years old or older, and more than 46,154 (7.5%) of them are considered structurally deficient and in need of significant maintenance, rehabilitation, or replacement (ASCE 2021). The report also indicated that funds for rectifying the bridges are lacking, and there is already a backlog of $125 billion for bridge repair. This would be a serious matter anytime but is even more so amid an increase in the number and cost of flood catastrophes caused by climate change (Kopp et al. 2018).

The impacts of extreme weather events such as flooding have been exacerbated in recent years by urbanization (e.g., an increase in impermeable surfaces), inappropriate land use in flood-prone areas, and climate change (Pregnolato et al. 2021). Rainfall events are becoming more frequent and intense (Solomon et al. 2007), triggering bridge failure incidents worldwide as the hydrodynamic loadings generated from flooding exert force on them (McCall 2016, Dokoupil 2013, Byrne 2018, Cook et al. 2015). It is imperative that preventive measures be taken to mitigate bridge failures by investigating the flood forces on stream-crossing bridges; however, flood events are usually complex scenarios that require a physical model of the fluid-structure interactions to accurately evaluate the magnitude of the flood actions and hydrodynamic loads.

As the name implies, a physical model is a scale representation of a prototype (i.e., a full-scale structure) used during the design phase to optimize the structure's design and ensure its safety. Modeling physical systems play a crucial role in verifying solutions and providing information that cannot be obtained through analytical and numerical solutions. Physical model studies are also used to estimate the hydrodynamic forces acting on hydraulic structures such as bridges, culverts, and spillways, etc. The use of a physical model also aids decision-makers in visualizing the flow field before selecting an appropriate design (Chanson 2004). In the past, researchers performed physical modeling in laboratory flumes to investigate hydrodynamic forces and bridge failures caused by flooding (Jempson 2000, Kerenyi et al. 2009, Oudenbroek 2018). Since laboratory experiments are limited to certain geometries and flow conditions, numerical modeling has also been conducted to quantify the hydrodynamic forces exerted on bridge superstructures (Lin et al. 2012, Bricker and Nakayama 2014, Naderi 2018); however, the results from field observations or laboratory experiments are required for model validation and verification.

1.3 RESEARCH QUESTIONS AND OBJECTIVES

The overall objective of this research was to investigate the effects of flow characteristics and bridge geometry on flood-induced hydrodynamic forces. Due to the broad scope of this topic, the research addresses four specific research questions:

1. *In what ways and to what extent do the flow parameters (i.e., flow velocity and flow depth) influence hydrodynamic forces*?

The parameters of a stream's flow reportedly affect the hydrodynamic forces acting on a bridge. These parameters include the depth and velocity of the flow and the position of the bridge with respect to the streambed. Investigating the effect of these parameters on hydrodynamic forces will facilitate the development of accurate and improved guidelines and standards for designing resilient bridges.

2. *How does the geometry (i.e., deck width, girder height, and girder shape) of bridge superstructures affect hydrodynamic forces and force coefficients?*

The hydrodynamic responses of bridge superstructures are influenced by the geometry and shape of the deck and girders; however, the effects of bridge geometry on hydrodynamic forces have not been thoroughly investigated. Estimating the flood loads for each bridge is essential to designing a bridge that is safe and determining its vulnerability to flooding. The purpose of this study is to investigate flood-induced hydrodynamic forces for a variety of deck widths, girder heights, and beam shapes. Based on the results of this study, designers will be able select a bridge geometry and retrofit existing bridges to accommodate flood forces with minimal effects on hydrodynamic forces.

3. *What is the effect of flow conditions and bridge geometry on the mean flow field and how does it affect the hydrodynamic forces acting on the bridge? How are force coefficients related to flow kinematics?*

Hydrodynamic forces on submerged bridge decks result from an imbalance of dynamic pressure surrounding the decks. This study aims to investigate the interactions between the mean flow field and bridge structures of partially-to-fully submerged bridge geometries for different flood velocities. The bridge deck attachments (i.e., barriers, railings, and girders) disturb the flow structures (i.e., separated boundary layer, vortex, reattachment, and wake blockage) and have a significant effect on the flow and hydrodynamic characteristics of the bridge deck. Investigating the mean velocity field may provide a better understanding of the trend of hydrodynamic forces at various flow conditions and geometric variations.

4. *How does flow blockage caused by debris accumulation and substructures (i.e., piers and bent caps) affect hydrodynamic forces and coefficients of bridge superstructures?*

The accumulation of debris affects the entire flow pattern by causing a contraction in the flow that results in increased velocity around the submerged deck. Bridge substructures (e.g., piers and bent caps) may also alter the flow characteristics and hydrodynamic forces acting on bridge deck and railings. Therefore, this research question examines the combined effect of debris, superstructures, and substructures on flood forces. Successful integration of accumulated debris with flood force will result in more reliable guidelines for designing stream-crossing bridges.

1.4 THESIS OVERVIEW

This thesis is presented in manuscript form, with Chapters 2, 3, and 4 corresponding to a manuscript written by the author. Chapter 1 consists of the motivation of the study, a background of previous flood force investigations of bridge superstructures and existing literature and guidelines, and the objective of the research. Chapter 2 relates the investigation of flow parameters and bridge geometry on the hydrodynamic forces of bridge superstructures. Chapter 3 presents a laboratory study that was conducted to investigate the mean flow field around fully and partially submerged bridge superstructures, using the particle image velocimetry (PIV) technique. This chapter also investigates the relationship between hydrodynamic force coefficients and dimensionless parameters extracted from the mean flow field data. Chapter 4 presents a series of experiments that were performed to explore the effects of debris accumulation and the presence of substructures on the hydrodynamic force coefficients of bridge superstructures. This was achieved by comparing the results of experiments conducted on superstructures with debris and substructures with those of bridge superstructures without either of those conditions. Chapter 5 summarizes the conclusions of the thesis and provides suggestions and recommendations for future research.

The material in these chapters is supplemented by Appendices A, B, and C. Appendix A discusses the accuracy of measurements, Appendix B presents the dimensions and schematics of the selected bridge models, and Appendix C documents the steps that were taken to calculate the hydrodynamic force and moment coefficients from the flow and geometry measurements.

References

American Association of State Highway and Transportation Officials (AASHTO), 2017. AASHTO LRFD Bridge Design Specifications, 8th ed. Washington, DC.

Almasri, A. and Moqbel, S., 2017. Numerical evaluation of AASHTO drag force coefficients of water flow around bridge piers. *Journal of Engineering Materials and Technology*, *139*(2).

Ahamed, T., Duan, J.G. and Jo, H., 2020. Flood-fragility analysis of instream bridges–consideration of flow hydraulics, geotechnical uncertainties, and variable scour depth. *Structure and Infrastructure Engineering*, pp.1-14.

ASCE, 2021, Report Card for America's Infrastructure https*://infrastructurereportcard.org/wp-content/uploads/2020/12/National_IRC_2021-report-2.pdf Accessed: 2021-06-17*

Bricker, J.D. and Nakayama, A., 2014. Contribution of trapped air, deck superelevation, and nearby structures to bridge deck failure during a tsunami. *Journal of Hydraulic Engineering*, *140*(5), p.05014002.

Byrne, K. Major flooding on Llano River triggers bridge collapse near Kingsland, Texas [Online] Available at: https://www.accuweather.com/en/weather-news/major-flooding-on-llano-river-triggers-bridge-collapse-near-kingsland-texas/342859 [Accessed: 2 February 2020]

Chanson, H., 2004. *Hydraulics of Open Channel Flow*. Elsevier.

Chen, W.L., Li, H. and Hu, H., 2014. An experimental study on the unsteady vortices and turbulent flow structures around twin-box-girder bridge deck models with different gap ratios. *Journal of Wind Engineering and Industrial Aerodynamics*, *132*, pp.27-36.

Dokoupil, T., 2013. Colorado floods: A month later, mountain towns 'spooky' and deserted https://www.nbcnews.com/news/us-news/colorado-floods-month-later-mountain-towns-spooky-deserted-flna8c11417559 Accessed: 2021-06-07

Diehl, T.H., 1997. *Potential drift accumulation at bridges*. US Department of Transportation, Federal Highway Administration, Research and Development, Turner-Fairbank Highway Research Center.

Cook, W., Barr, P.J. and Halling, M.W., 2015. Bridge failure rate. *Journal of Performance of Constructed Facilities*, *29*(3), p.04014080.

Fang, Q., Hong, R., Guo, A., Stansby, P.K. and Li, H., 2018. Analysis of hydrodynamic forces acting on submerged decks of coastal bridges under oblique wave action based on potential flow theory. *Ocean Engineering*, *169*, pp.242-252.

Fechter, J. 2015. TxDOT: Two bridges completely wrecked in Central Texas floods, others damaged [Online] Available at: https://www.mysanantonio.com/news/local/article/TXDoT-Two-bridges-wrecked-in-the-Central-Texas-6294892.php [Accessed: 2 March 2020].

FHWA (Federal Highway Administration), 2009. Bridges, Structures, and Hydraulics. *23 CFR 650, subpart C*.

Flint, M.M., Fringer, O., Billington, S.L., Freyberg, D. and Diffenbaugh, N.S., 2017. Historical analysis of hydraulic bridge collapses in the continental United States. *Journal of Infrastructure Systems*, *23*(3), p.04017005.

Hunt, B.E., 2009. *Monitoring scour critical bridges* (Vol. 396). Transportation Research Board.

Jempson, M., 2000. Flood and debris loads on bridges. (PhD), Doctoral Thesis, University of Queensland.

Jordan, B., 2015. Analysis of bridges subjected to flood loadings based on different design standards. Bachelor dissertation. University of Southern Queensland. Australia.

Kerenyi, K., Sofu, T. and Guo, J., 2009. Hydrodynamic forces on inundated bridge decks (No. FHWA-HRT-09-028). Turner-Fairbank Highway Research Center.

Kopp E. R., Kunkel E. K., Nielsen-Gammon J., 2018. Fourth national climate assessment. (Chapter 2). U.S. Global Change Research Program. https://doi.org/10.7930/NCA4.2018

Kosa, K., 2014. Damage analysis of bridges affected by the tsunami in the Great East Japan Earthquake. *Journal of JSCE*, *2*(1), pp.77-93.

Kabir, S.M.I. and Ahmari, H., 2020. Evaluating the effect of sediment color on water radiance and suspended sediment concentration using digital imagery. *Journal of Hydrology*, 589, p.125189.

Lee, G.C., Mohan, S., Huang, C. and Fard, B.N., 2013. *A study of US bridge failures (1980-2012)*. Buffalo, NY: MCEER.

Lin, C., Kao, M.J., Hsieh, S.C., Lo, L.F. and Raikar, R.V., 2012. On the flow structures under a partially inundated bridge deck. *Journal of Mechanics*, *28*(1), pp.191-207.

Malavasi, S. and Guadagnini, A., 2003. Hydrodynamic loading on river bridges. *Journal of Hydraulic Engineering*, *129(11)*, pp.854-861.

Malavasi, S., Franzetti, S. and Blois, G., 2004, June. PIV investigation of flow around submerged river bridge deck. In *Proceedings of the International Conference of River Flows, Napoli, Italy* (pp. 601-608).

Malavasi, S. and Blois, G., 2007. Influence of the free surface on the flow pattern around a rectangular cylinder. In Ninth International Symposium on Fluid Control, Measurements and Visualization, Tallahassee, FL.

Malavasi, S. and Guadagnini, A., 2007. Interactions between a rectangular cylinder and a free-surface flow. *Journal of Fluids and Structures*, *23*(8), pp.1137-1148.

McCall, I. 2016. Flood Investigation Reports - Carlisle | Cumbria County Council https://www.cumbria.gov.uk/planningenvironment/flooding/flood_investigation_reports_carlisle.asp Accessed: 2021-06-07.

Matsuda, K., Cooper, K.R., Tanaka, H., Tokushige, M. and Iwasaki, T., 2001. An investigation of Reynolds number effects on the steady and unsteady aerodynamic forces on a 1: 10 scale bridge deck section model. *Journal of Wind Engineering and Industrial Aerodynamics*, *89*(7-8), pp.619-632.

Naderi, N., 2018. Numerical simulation of hydrodynamic forces on bridge decks. (Master dissertation, TU Delft)

Nasim, M., 2019. Damage Modelling of Reinforced Concrete Bridge Piers under Flood and Log Impact (Doctoral dissertation, RMIT University).

Naudascher, E. and Medlarz, H.J., 1983. Hydrodynamic loading and backwater effect of partially submerged bridges. *Journal of Hydraulic Research*, *21*(3), pp.213-232.

Oudenbroek, K., Naderi, N., Bricker, J.D., Yang, Y., Van der Veen, C., Uijttewaal, W., Moriguchi, S. and Jonkman, S.N., 2018. Hydrodynamic and debris-damming failure of bridge decks and piers in steady flow. *Geosciences*, 8(11), p.409.

Parola, A.C., Apelt, C.J. and Jempson, M.A., 2000. Debris forces on highway bridges (No. 445). Transportation Research Board.

Padgett, J., DesRoches, R., Nielson, B., Yashinsky, M., Kwon, O.S., Burdette, N. and Tavera, E., 2008. Bridge damage and repair costs from Hurricane Katrina. *Journal of Bridge Engineering*, *13*(1), pp.6-14.

Pregnolato, M., Bates, P., Winter, A.O., Mascarenas, D., Sen, A.D. and Motley, M.R., 2021. An integrated impact analysis for riverine bridges subjected to high river flows. In *Bridge Maintenance, Safety, Management, Life-Cycle Sustainability and Innovations* (pp. 1258-1264). CRC Press.

Solomon, S., Manning, M., Marquis, M. and Qin, D., 2007. Climate change 2007-the physical science basis: Working group I contribution to the fourth assessment report of the IPCC (Vol. 4). Cambridge University Press.

Sousa, J.J. and Bastos, L., 2013. Multi-temporal SAR interferometry reveals acceleration of bridge sinking before collapse. *Natural Hazards and Earth System Sciences*, *13*(3), pp.659-667.

Thai, T.K.C., 2019. Numerical simulation of the turbulent flow over submerged bridge decks. *Magazine of Civil Engineering*, *85*(1).

Taricska, M., 2014. An analysis of recent bridge failures (2000-2012). Master Thesis, The Ohio State University.

Wardhana, K. and Hadipriono, F.C., 2003. Analysis of recent bridge failures in the United States. *Journal of Performance of Constructed Facilities*, *17*(3), pp.144-150.

Zhu, Q., Lin, J.C., Unal, M.F. and Rockwell, D., 2000. Motion of a cylinder adjacent to a free-surface: flow patterns and loading. *Experiments in Fluids*, *28*(6), pp.559-575.

CHAPTER 2

EXPERIMENTAL STUDY CONDUCTED TO INVESTIGATE THE EFFECTS OF BRIDGE GEOMETRY AND FLOW CONDITION ON HYDRODYNAMIC FORCES

ABSTRACT

Floods are reported as the most frequent cause of bridge failure in the U.S. and around the world despite bridges being designed to pass the design flow while maintaining a minimum freeboard. Floodwater exerts forces on bridges that shear and overturn their decks and may cause them to fail. When a bridge fails, it loses its total or partial serviceability, causing fatalities, delays in emergency transportation and evacuation efforts, and economic losses. An accurate estimation of hydrodynamic forces on a bridge superstructure, therefore, is vital to assess its vulnerability to flooding. The purpose of this study is to investigate the effects of bridge geometry and flow conditions on hydrodynamic forces. A series of experiments on bridge-scale models were performed in a laboratory flume to analyze the response of the drag, lift and moment coefficients on the bridge geometry (deck width, and girders' height and shape) and flow conditions (inundation ratio, proximity ratio, blockage ratio, and Froude number). The experimental results showed that hydrodynamic force and moment coefficients are dependent on the extent of the bridge submergence, Froude number, and proximity of the bridge to the streambed. The relationship between bridge geometry and force coefficients indicated that bridges' geometric features influence the flow field, as well as drag, lift, and moment coefficients.

Author Keywords: River-crossing bridges, Hydrodynamic forces, Submergence, Bridge geometry, Bridge failure, Flood flow

2.1 INTRODUCTION

Floods are by far the most destructive natural disasters to infrastructures (Nasim 2019). Stream-crossing bridges are crucial elements of road infrastructures that are vulnerable to flooding, and bridge failures cause significant economic losses and delay the rescue and reconstruction of disaster-stricken areas (Fang et al. 2018). Over the past 30 years, bridges in the U.S. and globally have been partially damaged or have completely failed because of flooding (Wardhana and Hadipriono 2003, Sousa and Bastos 2013, Taricska 2014, Fechter 2015, Byrne 2019). Wardhana and Hadipriono (2003) investigated the history and causes of bridge failures in the U.S. and found that 503 bridges of various types failed between 1989 and 2000. Taricska (2014) reported a total of 329 bridge failures in the U.S. from 2000 to 2012. Most of the failures were caused by major flood events (Ahamed et al. 2020), as bridge superstructures may become fully or partially submerged during high flow events, and the hydrodynamic forces result in shearing and overturning the bridge elements.

An accurate estimation of the hydrodynamic forces on a bridge superstructure is essential to assessing its vulnerability to flooding. Stream-crossing bridges experience hydrostatic, buoyant, and hydrodynamic forces. Hydrostatic force (F_h) for an inundated bridge is created by the hydrostatic pressure on the upstream and downstream of the deck; buoyant force (F_B) is equal to the weight of the water displaced by submerged bridge elements; and hydrodynamic forces include drag force (F_D), which is created by the pressure of the flowing water in the flow direction and lift force (F_L), which is produced by the pressure of flowing water in the normal direction of the flow. Bridges may also experience overturning moments (M_{cg}) that are created by uneven forces applied on a bridge. Flood forces and overturning moments exerted on a bridge superstructure are

schematically shown in Fig. 2.1. Eqns. 2-1 to 2-5 may be used to calculate the forces and overturning moment.

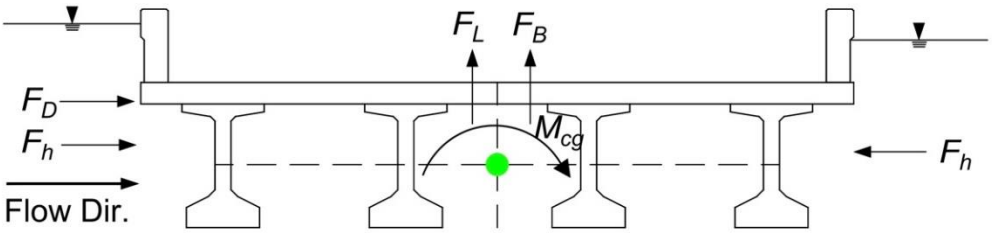

Fig. 2.1 Schematic of forces and overturning moment exerted by flood on a stream-crossing bridge superstructure

$$\boldsymbol{F_h = \frac{1}{2}\rho_w g h A} \quad \text{(hydrostatic force)} \tag{2-1}$$

$$\boldsymbol{F_B = \rho_w g \forall} \quad \text{(buoyant force)} \tag{2-2}$$

$$\boldsymbol{F_D = \frac{1}{2}\rho_w C_D A_D V^2} \quad \text{(drag force)} \tag{2-3}$$

$$\boldsymbol{F_L = \frac{1}{2}\rho_w C_L A_L V^2} \quad \text{(lift force)} \tag{2-4}$$

$$\boldsymbol{M_{cg} = \frac{1}{2}\rho_w C_M L W^2 V^2} \quad \text{(overturning moment)} \tag{2-5}$$

In these equations, ρ_w is water density; g is gravitational acceleration; h is the depth of the water; A is the projected area normal to the upstream and downstream faces of the submerged portion of the bridge superstructure; A_D is the projected area of the submerged portion of the superstructure upon which drag force is exerted and normal to the flow; A_L is the projected area of the submerged superstructure on which the lift force acts and is parallel to the flow; $\forall$ is the volume of superstructure elements submerged; V is the depth-averaged approach flow velocity; L and W are the bridge deck length and width, respectively; and C_D, C_L, and C_M are drag force, lift force, and moment coefficients.

Drag force or pressure drag is significant for bluff bodies like bridge superstructures. As flow separates from a bridge obstruction, a wake zone or blockage is produced by the separated boundary layers of the free surface, causing variations in the water level and pressure at the front and rear ends of the deck (Jempson 2000). The variations in the water level create an imbalance of the dynamic pressure upstream and downstream of the submerged body that results in drag force or pressure drag (Malavasi and Guadagnini 2007). Similarly, lift force is the result of changes to the pressure distribution at the top and bottom sides of the deck; moment is affected by changes to the pressure acting on all sides of the deck (Jempson 2000).

The drag force coefficient is a non-dimensional value that is the ratio of the drag force to the product of the free stream dynamic pressure and wetted area. Eqn. 2-3 can be re-written as follows for calculating the drag force coefficient:

$$C_D = \frac{F_D}{(0.5\rho_w V^2)A_D} \tag{2-6}$$

where F_D in the numerator is the result of the net pressure between the upstream and downstream sides of the deck times the wetted area in the direction of the flow. The $0.5\rho_w V^2$ term in the denominator is the free stream dynamic pressure. Similarly, the relationships for the lift force and moment coefficients can be derived by rearranging Eqn. 2-4 and Eqn. 2-5, respectively.

$$C_L = \frac{F_L}{(0.5\rho_w V^2)A_L} \tag{2-7}$$

$$C_M = \frac{M}{(0.5\rho_w V^2)\, A\, W} \tag{2-8}$$

In Eq. 2-8 $A = L\,W$, and W is used as an additional length to make the moment coefficient nondimensional.

The coefficients of hydrodynamic forces and overturning moments are essential information for designing bridges under flood forces. They are usually parameterized as a function of the inundation ratio (h^*), proximity ratio (*Pr*), and Froude number (*Fr*). A schematic representation of these parameters is illustrated in Fig. 2.2.

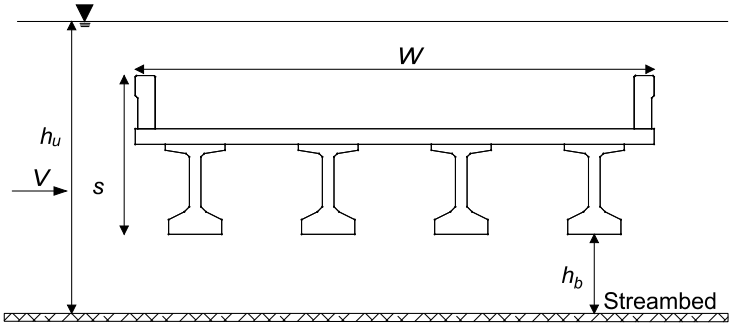

Fig. 2.2 Schematic of a fully submerged bridge deck

The inundation ratio (h^*) is defined as the water depth measured from the low chord of a bridge girder ($h_u - h_b$) to the height of a bridge superstructure (*s*) and is expressed as

$$h^* = \frac{h_u - h_b}{s} \tag{2-9}$$

The proximity ratio (*Pr*) is defined as the ratio of the distance of a bridge low chord from the channel bottom (h_b) to the height of a bridge superstructure (*s*) and is expressed as

$$Pr = \frac{h_b}{s} \tag{2-10}$$

The Froude number (*Fr*) is defined as the ratio of the inertia force and gravity force and is expressed as

$$Fr = \frac{V}{\sqrt{g h_u}} \tag{2-11}$$

The height of the bridge superstructure and its length in the flow direction may affect hydrodynamic loading on the deck. In order to estimate their effects on the force and moment coefficients, these geometric features can be parameterized as aspect ratio and blockage ratio.

The aspect ratio (*Ar*) is defined as the streamwise length of the bridge deck (*W*), i.e., the distance between the outer edges of both railings to the height of the bridge deck (*s*) and expressed as

$$Ar = \frac{W}{s} \tag{2-12}$$

The flow blockage ratio (*Br*) may be defined as the ratio of the projected surface area of the bridge superstructure to the flow area. When widths of the bridge superstructure and stream are equal, the blockage ratio is equal to

$$Br = \frac{s}{h_u} \tag{2-13}$$

In the U.S., the state and municipal departments of transportation (DOTs) design bridges using manuals and guidelines provided by professional organizations and government agencies such as the American Association of State Highway and Transportation Officials (AASHTO) (Flint et al. 2017). The AASHTO load and resistance factor designs (LRFD) and other traditional methods calculate hydrodynamic forces by considering the constant drag and lift force coefficients (Jordan 2015, Almarsi and Moqbel 2017). Results from previous physical modeling of hydrodynamic forces on river-crossing bridges, however, indicate the dependency of these coefficients on the inundation ratio, Froude number, proximity ratio, and bridge geometry (Jempson 2000, FHWA 2009). The complex behavior of flood forces on bridge superstructures is often studied in the laboratory via physical models. A summary of recent studies that utilized laboratory experiments to investigate flood forces on bridges follows.

Jempson (2000) studied hydrodynamic forces on scale models of bridge superstructures and piers. The superstructures were comprised of two prestressed concrete girders, a steel plate girder, a spread box beam, an adjacent box beam, a steel truss bridge, and a box girder. The results of their study were expressed as design charts for C_D, C_L, and C_M and revealed that the coefficients depend on the relative submergence S_R (a parameter similar to the inundation ratio), Froude number (Fr), and proximity ratio (Pr). The length-to-height ratio (a parameter similar to aspect ratio) of the bridge superstructures was kept constant at 4. Variations in the force and moment coefficients of bridges with different aspect and blockage ratios were inconclusive in their study.

Malavasi and Guadagnini (2003, 2007) performed physical modeling experiments to estimate hydrodynamic loading on partially and fully submerged rectangular cross-sections of bridge models. The results indicated that the force coefficients were considerably impacted by the inundation ratio and deck Froude number ($F_S = V/\sqrt{gs}$), and the free surface and bottom boundary caused drag and lift forces different from what would be expected from an identical geometry in an unbounded flow situation. Since these results were obtained from a cylindrical, rectangular cross-section model, they are not directly applicable to bridge superstructure geometry in the field.

The FHWA (2009) investigated hydrodynamic forces on bridges with three types of decks (six-girder, three-girder, and streamlined) under different flow conditions and inundation ratios, and the results showed that the Froude number and type of bridge deck influence force and moment coefficients. The design charts developed in their study did not consider the effects of the proximity ratio on force and moment coefficients.

The characteristics of flow around bridge superstructures are significantly affected by the bridge length in the flow direction. Several researchers conducted experiments to investigate hydrodynamic loading and the flow field around rectangular cylinders with different deck aspect ratios (Ar) (Zhong et al. 2019, Thai 2019). Thai (2019) reported that the drag force coefficient showed a maximum at Ar = 2 and decreased as the Ar increased. Chu et al. (2016) pointed out that the drag force coefficient increases as the blockage created by the height of the rectangular deck increases. The shape and size of the girders also influence the flow characteristics and hydrodynamic forces (FHWA 2009, Kosa 2014).

Researchers have also investigated the hydrodynamic force coefficients of a constant deck width, girder geometry, and certain flow conditions but did not consider the effects of flow parameters, aspect ratio, blockage created by girders, or the shape and size of the bridges. This research aims to investigate the effects of flow condition and bridge deck geometry on hydrodynamic force and moment coefficients of river-crossing bridges under flood action. The results of the physical modeling can be used to calibrate and validate numerical models, both computational fluid dynamics (CFD) and structural analysis, that can reproduce structural responses of bridges under different flood conditions. The experimental results can also be used to develop mitigation measures for retrofitting existing bridges and designing new bridges with geometries that have minimal effects on the flow structure and hydrodynamic forces.

2.2 MATERIALS AND METHODS

2.2.1 Scale Bridge Models

Physical models are commonly used to estimate the hydrodynamic forces on hydraulic structures such as bridges, culverts, spillways, etc. When surface tension and compressibility can be

neglected in fluid dynamics, the Reynolds number (*Re*) and Froude number (*Fr*) are the most influential force ratios that should be considered in designing a physical model. Inertia force and gravity govern the flow in open channels, and the drag coefficients do not change significantly across the range of the Reynolds numbers usually observed in the lab ($Re > 10^4$) and field data ($Re > 10^6$) (Oudenbroek 2018). Therefore, Froude number scaling was used to design physical models of bridge elements in this study, and the geometrical parameters of the bridge models were selected based on the experimental facility's ability to mimic the field conditions. A geometric reduction scale of 1:50 was employed, allowing for the reproduction of typical field scenarios. The bridge superstructure models were made of aluminum because its weight (2.7 g/cm^3) is similar to that of reinforced concrete (2.5 g/cm^3).

The effects of flood forces on bridges were assessed through physical modeling in a laboratory setup, and actual bridge geometry and flood flow conditions were assessed to estimate the significance of bridge geometry and flow parameters on hydrodynamic force and overturning moment coefficients. Two types of deck widths were selected to develop different aspect ratios, and four types of girders/beams were selected to reproduce different blockage ratios and girder shapes and heights. Finally, solid railings were selected to generate the maximum loading surface during flooding. The selected superstructure shapes represent the common bridge geometry found in the field. Table 1 summarizes the prototype, model dimensions, and associated parameters of bridges tested in this study. In the first column of Table 2.1, the bridge attributes include the names of the structural elements in parentheses, according to TxDOT specifications. Detailed drawings of the bridge elements are presented in Appendix B.

Table 2.1. Summary of Geometry of Bridge Models

Bridge Attribute	Prototype Dimension (cm)	Model Dimension (cm)	Parameter
Deck width (W26)	1402.08	28.04	Aspect ratio
Deck width (W46)	792.48	15.85	Aspect ratio
I-girder height (TX54)	137.16	2.74	Blockage ratio
I-girder height (TX28)	71.12	1.42	Blockage ratio
Box beam height (BB28)	71.12	1.42	Girder shape
Railing height (T221)	81.28	1.62	-

2.2.2 Test Facility and Experimental Procedures

Experiments were performed in a 5-m long, 0.3-m wide, and 0.45-m deep Plexiglas recirculating flume in a laboratory. The flow in the flume was maintained by its recirculatory pumping system and two external pumps. The flume was set horizontal, and the water depth was controlled by an adjustable tailgate. The flow rate supplied by the external pumps was measured using the digital SonoTrac ST30 ultrasonic flowmeter that was attached to the flume's inlet pipe. The orifice method was used to measure the discharge supplied by the recirculatory pumping system. The point velocity upstream of the bridge was measured at the beginning of each experiment, using a three-dimensional acoustic doppler velocimeter (ADV). The flow depth was recorded, using a point gauge upstream of the superstructure and by measuring tapes affixed to the flume wall. Forces in three directions and moments were measured using Interface-Model 3A100-100N-D11 with 100 N capacity load cell and Interface-Model MRT2 torque cell with 10 N-m capacity. The measurement uncertainty of the load and torque cell are briefly discussed in Appendix A. A mounting frame was designed and constructed to house the load and torque cells, isolate them from external vibrations, and keep them elevated above the surface of water surface due to their vulnerability to submersion. The cells were secured to the bridge deck via two vertical support plates (Fig. 2.3).

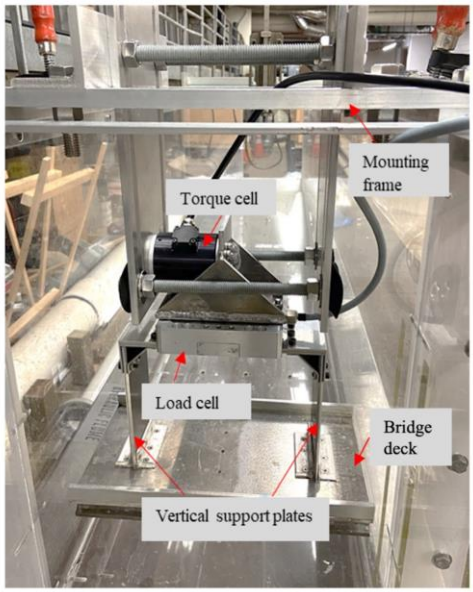

Fig. 2.3 Experimental setup including load and torque cells, mounting frame, and vertical support plates

The experiments were performed by attaching the bridge model superstructure to the mounting frame via two vertical support plates (Fig. 2.3). The frame was firmly fastened to the flume's top railing to prevent any movement or vibrations from occurring while transferring forces to the load and moment cells. The frame was secured to the flume, with care taken to ensure that the clearance between the flume walls and both sides of the bridge deck was sufficient to avoid any friction. The pumps were activated, and the valves on the flume inlet pipes were opened until the desired flow rate was achieved. Preliminary tests were conducted to evaluate the performance of the load cell and to estimate the forces during the data acquisition process. Force data acquired at a 1.25 Hz frequency displayed acceptable stability in mean and variance of force and moment values within two minutes of the beginning of the acquisition process. Before recording the force data, the load and moment cell readings were zeroed, as the water level was kept below the bridge model. The height of the flume's tailgate was set to reach the lowest inundation ratio. Once the bridge model elevation and flow rate were set at the desired test conditions, the force and moment data were

recorded for two minutes. The bridge was lowered in steps for higher inundation ratios, and the same procedure was followed for each inundation ratio.

The experiments replicated bridges without middle piers and bent caps that span a stream. They were performed for a series of inundation ratios ranging from 0.25 to 2.5 with increments of 0.25, depending on the superstructure's height and distance from the channel floor, i.e., $3 \leq Pr \leq 5.25$. The flow condition was characterized by Froude numbers of 0.20, 0.27, and 0.34, corresponding to the observed floods in the field.

2.3 RESULTS AND DISCUSSION

The readouts of the load and torque cells were corrected to calculate the net hydrodynamic forces and moments exerted on the bridge models. The hydrostatic force (F_h) was subtracted from the recorded total streamwise force to calculate the drag force (F_D). The buoyant force (F_B) was deducted from the measured vertical force to calculate the lift force (F_L) acting on the bridge deck. The torque cell readout moment was corrected to consider the centroidal moment (M_{cg}) with respect to the bridge deck system's center of gravity. After the corrections were made, the drag (C_D), lift (C_L), and moment (C_M) coefficients were calculated using Eqns. 2-6 to 2-8. The detailed steps taken to calculate the force and moment coefficients are illustrated in Appendix C. The variations of the coefficients as a function of Froude number (Fr), inundation ratio (h^*), proximity ratio (Pr), aspect ratio (Ar), blockage ratio (Br), and shapes of the girder are presented in the following.

2.3.1 Comparison with Previous Studies

The results of the present study of four-girder and six-girder bridge models were compared with the results from two previous laboratory experiments. The first experimental results were acquired from laboratory tests on a six-girder bridge deck and railing (FHWA 2009); the second were obtained for a four-girder bridge deck and railing (Jempson 2000). The flow condition and geometry of the bridge models investigated in this research were designed to be similar to those of the previous studies. The bridge model type, *Ar*, *Br*, and *Fr* for the three studies are presented in Table 2.2.

Table 2.2 Hydraulic and Geometric Comparison of the Present Study and Previous Studies

Study	**Bridge model**	**Aspect ratio (*Ar*)**	**Blockage ratio (*Br*)**	**Froude no. (*Fr*)**
Present work	6-girder	7.9	0.18	0.34
FHWA (2009)	6-girder	4.48	0.23	0.32
Present work	4-girder	4.5	0.18	0.34
Jempson (2000)	4-girder	4.0	0.16	0.30

The C_D and C_L values were plotted against the inundation ratio (h^*) shown in Fig. 2.4 to compare the results from the current experiment and the FHWA (2009) study of a six-girder bridge. A good agreement in the general trend of C_D was observed between these two studies, although it can be seen in Fig. 2.4a that the C_D for the current study was marginally greater than the FHWA's results for $h^* \leq 0.5$ and noticeably higher for $h^* > 1.0$. One of the distinctions between the FHWA study and the current study is the type of railing used in the experiments, which may account for higher C_D values under fully submerged conditions. While the railing in the FHWA study had voids, the one in the present study was solid, and the additional surface area contributed to higher drag coefficients. The difference between the blockage ratios in the two studies might have caused the C_D to be slightly higher in the present study. Fig. 2.4b shows that the C_L values in the present study

are much lower than the FHWA results, which could be explained by the differences in the aspect and blockage ratios in the two studies, as illustrated in Table 2.2. Moreover, the FHWA study did not consider the effect of the proximity ratio on the force coefficient, even though closer proximity at a higher inundation ratio might increase the C_L.

The results of the 4-girder bridge deck study in this research were compared with the experimental results performed by Jempson (2000) on a four-girder deck. The C_D comparison chart (Fig. 2.5a) shows good agreement between the two studies, and both show a trend of C_L directing upward as h^* increases for a fully submerged deck (Fig. 2.5b). Jempson found larger negative C_L values from his experiments but did not fully explain the comparatively larger lift coefficients. The moment coefficient (C_M) values due to flood loads significantly depend on the line of action of the resultant force. Hence, due to the variations in the methods used to choose the line of action in calculating C_M, the authors discarded the direct comparison of C_M with previous studies.

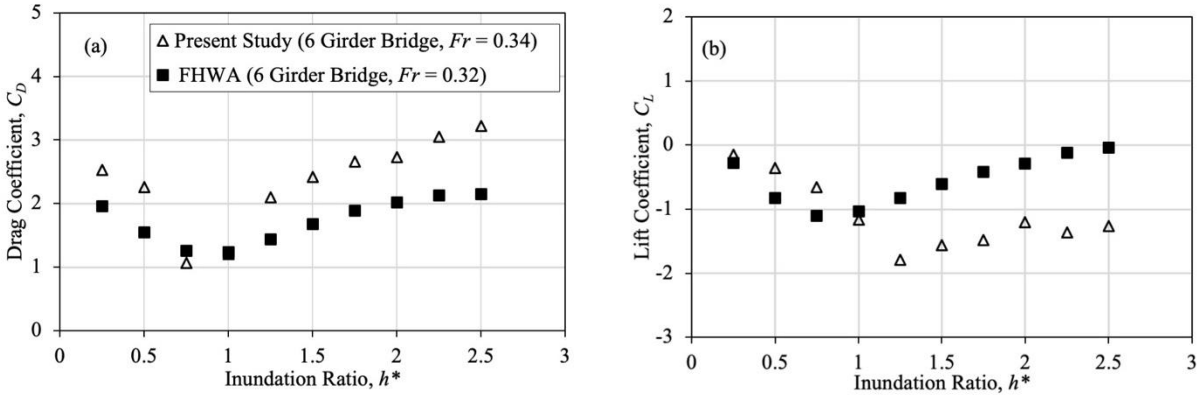

Fig. 2.4 Comparison of the present study with FHWA (2009) results: (a) drag coefficient (C_D), and (b) lift coefficient (C_L)

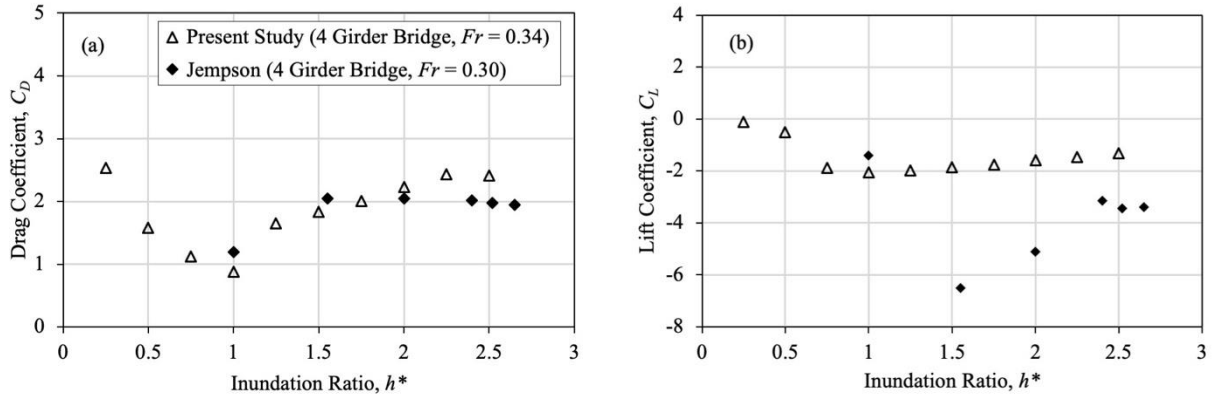

Fig. 2.5 Comparison of the present study with Jempson (2000) results: (a) drag coefficient (C_D), and (b) lift coefficient (C_L)

2.3.2 Effect of Flow Parameters

The flow pattern in the vicinity of the bridge may be influenced by flow conditions such as the Froud number, bridge submergence, and proximity of the bridge superstructure to the free surface and streambed that may affect the hydrodynamic forces. A series of experiments were performed to investigate the dependency of hydrodynamic force coefficients on these parameters. The dependency of C_D, C_L, and C_M on varying Froude numbers (Fr) and inundation ratios (h^*) was also investigated.

2.3.2.1 Proximity Ratio

Jempson's (2000) experimental results showed that drag and lift coefficients are affected by the proximity ratio; however, the influence of the proximity ratio on C_M was inconclusive in his study. Moreover, the velocity field varies, based on the bridge proximity, which may affect the drag, lift, and overturning moment. Therefore, it was necessary to investigate the significance of the proximity ratio on force and moment coefficients of a submerged bridge superstructure. Load and torque cells were used to measure the hydrodynamic loading of a four-girder bridge model with

Ar = 4.5 and Br = 0.18. The proximity ratios (Pr) of 1.09 to 5.07 were considered, as this is the range of Pr observed in the field (Ahmari et al. 2021). The bridge model was tested for inundation ratios (h^*) of 1 and 2 at a constant Froude number (Fr = 0.20).

Fig. 2.6 shows the variations of the drag, lift, and moment coefficients with the proximity ratio. For Pr < 2.5, the drag coefficient (C_D) showed a decreasing trend as the proximity ratio increased and reached constant values of 1 and 2.5 at h^*= 1 and h^*= 2 when the Pr was greater than 2.5 (Fig. 2.6a). At lower Pr values, the flume bed restrains the expansion of the streamlines around the bridge (i.e., wake blockage), which causes a decrease in pressure in the wake area and an increase in flow velocity below the deck and, consequently, an increase in C_D. Fig. 2.6b illustrates that for Pr < 2.5, the C_L decreased at h^*= 1 but increased at h^*= 2. For Pr > 2.5, the C_L leveled off, approaching values of -2.5 and -1.5 for h^*= 1 and h^*= 2, respectively. C_L was greater for h^*= 1 than for h^*= 2, possibly due to the separated boundary layer generating more suction (i.e., negative pressure) beneath the deck. Fig. 2.6c demonstrates that as the Pr increased from 1.09 to 2.5, the absolute values of C_M decreased for both h^*= 1 and h^*= 2. At both inundation ratios, the C_M approached a constant value (≈ ± 0.05). Based on these findings, a minimum Pr of 3 was maintained in the bridge model experiments to prevent the flume bed from affecting the force and moment coefficients.

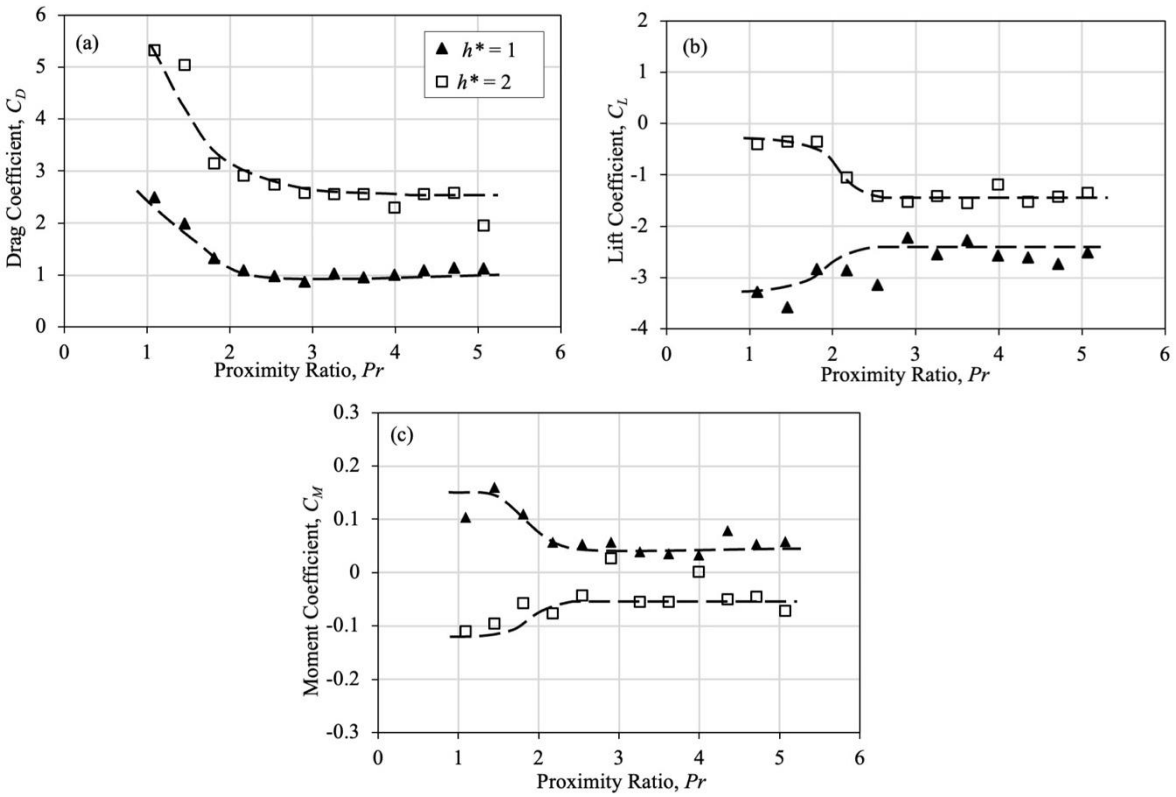

Fig. 2.6 Dependency of force and moment coefficients on proximity ratio: (a) drag coefficient (C_D), (b) lift coefficient (C_L), and (c) moment coefficient (C_M) (Ar = 4.5, Br = 0.18, Fr = 0.20)

2.3.2.2 Froude Number

To examine the significance of the Froude number on the force coefficients of bridge superstructures, experiments were performed with a bridge model that had four I-girders with Ar = 4.5 and Br = 0.18. Fig. 2.7 shows the mean streamwise force (i.e., hydrostatic and drag forces), vertical force (i.e., buoyant and lift forces) and overturning moment measured during the experiment. It is evident from Fig. 2.7a that the streamwise force increases with Fr and h^*. Fig 2.7b indicates that vertical lift force experiences a dip around the transition region from partial to full submergence (i.e., $0.75 < h^* < 1.25$). A higher Fr (= 0.34) results in the maximum absolute vertical force; the force reduces as the Fr diminishes. As shown in Fig. 2.7c, the maximum overturning moment occurs when Fr is 0.34, the minimum when Fr is 0.20, and the average when

Fr is 0.27. In addition, Fig. 2.7c shows that the overturning moment decreases (becomes more negative) as the *h** increases.

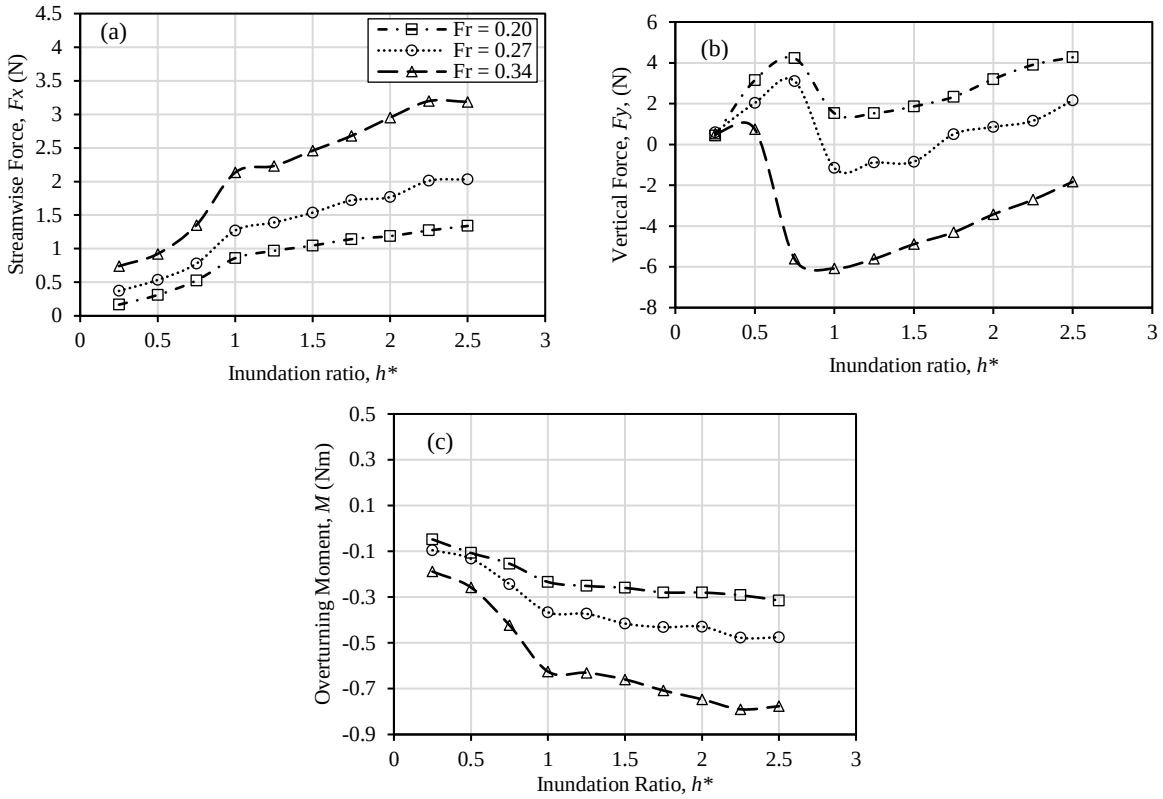

Fig. 2.7 Measured forces and moments for *Fr* of 0.20, 0.27, and 0.34 at various inundation ratios, *h**: (a) streamwise force (*Fx*), (b) vertical force (*Fy*), and (c) overturning moment (*M*)

The variations of C_D, C_L, and C_M with *Fr* numbers of 0.20, 0.27, and 0.34 at a constant *Pr* of 3.0 are shown in Fig 2.8. Fig. 2.8a illustrates a decreasing trend of the C_D with a decrease in the *Fr* for all the inundation ratios; the rate of decrease was more prominent for $h^* = 2.5$. This phenomenon could be explained by the fact that as the *Fr* increases, the surface area of the fluid-structure interaction becomes larger and the low-pressure region (i.e., wake region) reduces, which results in lower C_D values.

Greater absolute values of C_L were obtained as the *Fr* number increased (Fig. 2.8b). The rate of increase in C_L was more significant when $h^* = 2$. C_L increased from -0.45 for *Fr* = 0.2 to -1.31 for

Fr = 0.34. The dynamic pressure imbalance between the upper and lower sides of the deck produced the lift force on the deck; the downward C_L (negative lift coefficient) at higher a *Fr* number (= 0.34) was larger than that at a lower *Fr* number (= 0.20). This phenomenon was also observed in a study performed by Chu et al. (2016) on a rectangular deck. The C_M variation showed a mixed trend with an increase in *Fr* (Fig. 2.8c). For h^* = 0.5, the absolute values of C_M decreased to zero as the *Fr* increased from 0.2 to 0.27, then increased with an increase in *Fr*. For h^* =1 to 2.5, the C_M increased with an increase in *Fr*. This mixed behavior is because the C_M value is determined by the combined effects of changes in the forces exerted on all sides of a bridge superstructure and their point of action with reference to the deck centroid; therefore, a small difference in the flow pattern changes C_M.

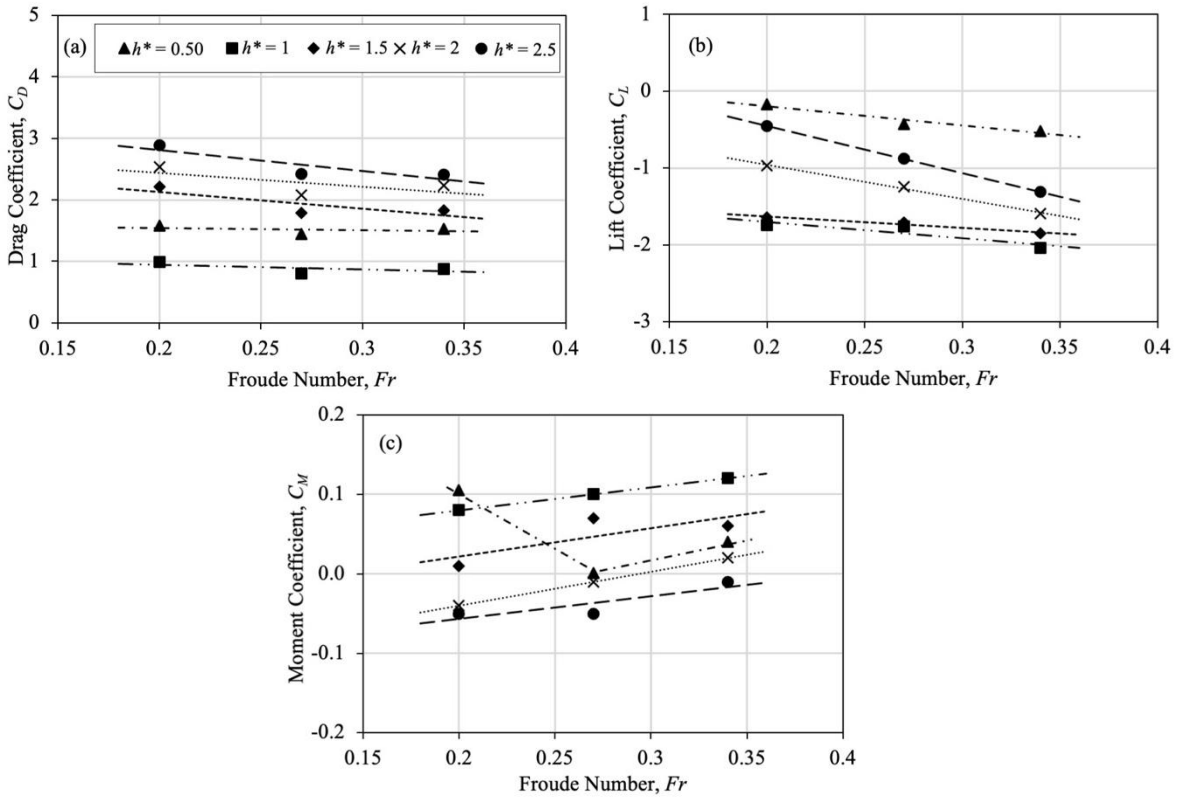

Fig. 2.8 Relationship between force and moment coefficients and Froude number (*Fr*) for inundation ratio (h^*) of 0.50, 1, 1.5, 2, and 2.5: (a) drag coefficient (C_D), (b) lift coefficient (C_L), and (c) moment coefficient (C_M) (*Ar* = 4.5, *Br* = 0.18)

2.3.2.3 Inundation Ratio

The results of the force and moment coefficients obtained from experiments conducted on bridge models with six I-girders were plotted against the inundation ratio and are shown in Fig. 2.9. The experiment was conducted for the *Fr* numbers of 0.20 and 0.34, *Br* = 0.18, and *Ar* = 7.9. The C_D values are illustrated against the h^* values in Fig. 2.9a, which shows that the C_D decreased as the inundation increased from partial to full submersion ($0.25 \leq h^* \leq 1$) for both *Fr* numbers. When the upstream water level crossed the top of the railing ($h^* > 1$), the C_D began to increase, and it continued increasing until it reached a plateau of $h^* \approx 2.5$. At $h^* < 1.0$, the wetted area increased with deck submersion; however, the mean velocity did not increase for the constant *Fr*, resulting in a decrease in the C_D. In contrast, the railing on the downstream side of the deck contributed to the drag force when $h^* > 1$, but the fluid-structure reference area remained constant with submersion, resulting in an increase in the C_D.

An overall negative C_L (pull-down) was observed for all values of h^* (Fig. 2.9b). The C_L showed a decreasing trend (increase in the absolute value of C_L) until $h^* = 1.25$, and it increased as the submergence increased (decrease in the absolute value of C_L) for both *Fr* values. For smaller inundation values ($h^* = 0.25 - 1$), water passed under the bridge, and flow separation occurred below the deck, resulting an increase in negative pressure below the deck and an increase in the negative lift force. For $h^* = 1 - 2.5$, the C_L values became less negative as the water level overtopped the railing, and the negative pressure below the deck was reduced by the pressure distribution on the top of the deck, resulting in reduced lift force. Other studies have described a similar behavior of the C_L with a change in the pressure distribution on the top and bottom of a rectangular deck (Malavasi et al. 2004, Chu et al. 2016).

Fig. 2.9c illustrates variations of C_M with h^* for both *Fr* values. Unlike C_D and C_L, the C_M diagram is concave upward. Jempson (2000) espoused that the positive moment is generated by the fluid-structure interaction on the upstream and downstream faces of the deck, and the negative moment is caused by the pressure distribution on the underside of the deck. In the present study, an increasing trend of C_M was observed for $h^* \leq 1.25$, as a result of the flow interaction with the upstream and downstream girder, deck, and railing. A decreasing trend of C_M was observed for higher inundation ratios ($h^* = 1.25 – 2.5$) due to the contribution of underside negative pressure on the deck that resulted in less positive moment for both *Fr* values.

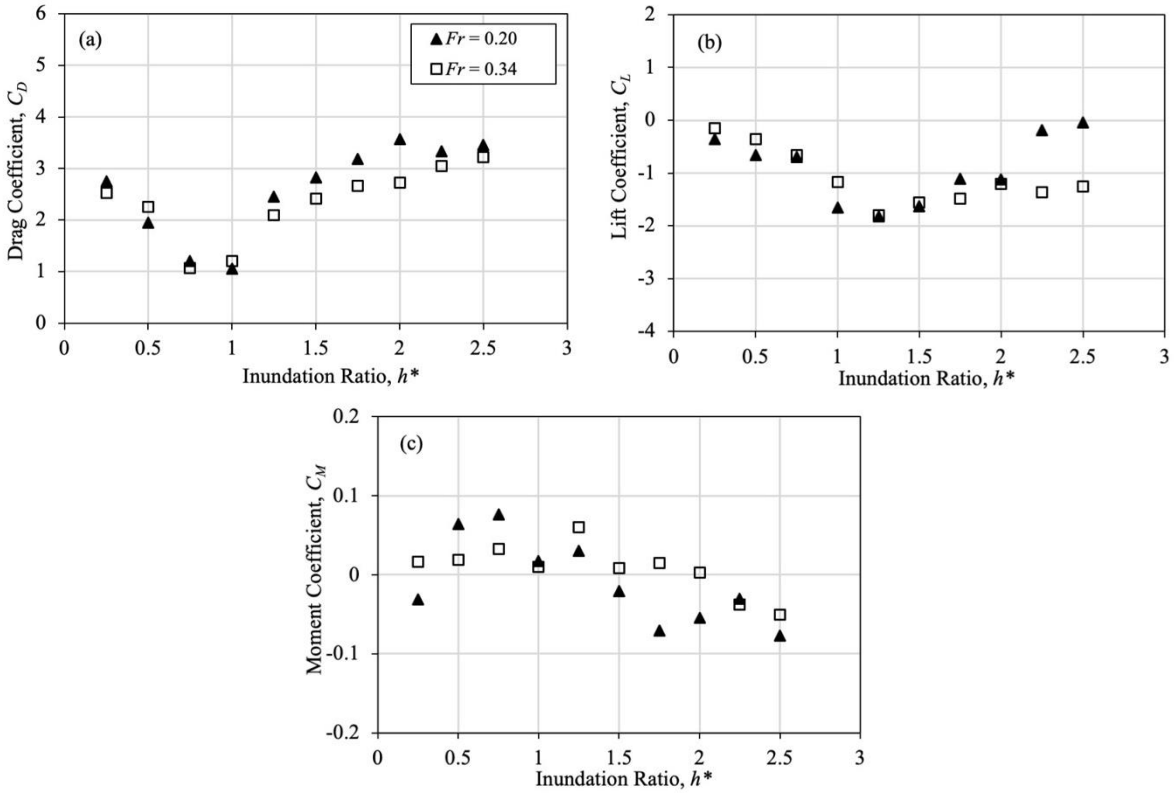

Fig. 2.9 Dependency of force and moment coefficients with inundation ratio, h^*: (a) drag coefficient (C_D), (b) lift coefficient (C_L), and (c) moment coefficient (C_M) (Br = 0.18, Ar = 7.9)

2.3.3 Effect of Bridge Geometry

Bridge geometry affects the flow field and velocity profiles, which can significantly influence the coefficients of hydrodynamic forces (FHWA 2009). In other words, the hydrodynamic response of bridge superstructures depends on the shape of the deck, and girder types and their spacing. This section presents the effects of deck width and girder height on the hydrodynamic forces and force and moment coefficients. As described before, the bridge deck width and girder height may be expressed as the aspect ratio (*Ar*) and blockage ratio (*Br*), respectively. The effect of girder shapes has been also investigated in this study, using typical I-girders and box beams.

2.3.3.1 Aspect Ratio

Zhong et al. (2019) performed numerical simulations of free surface flow over submerged rectangular cylinders to study the effects of the *Ar* on the C_D and C_L; however, their experiments were carried out on a rectangular deck, so the relationships between the *Ar* and force coefficients are not applicable to bridges with girders and railings. The influence of *Ar* on force coefficients of actual bridge decks remains unknown; therefore, it was necessary to explore the role of *Ar* on force and moment coefficients of a submerged bridge. In this experiment, a four-girder bridge model with *Ar* = 4.5 and a six-girder bridge model with *Ar* = 7.9 were used to simulate hydrodynamic forces (Fig. 2.10) for *Fr* of 0.34. Fig. 2.11 (a-c) illustrates the measured streamwise horizontal force, vertical force, and overturning moment on both decks. It is evident from the figure that a higher *Ar* (= 7.9) produces more streamwise force, vertical force, and overturning moment than a lower *Ar* (=4.5) for all *h**, except that the vertical forces in the partial submergence region are smaller for *Ar* of 7.9. This might be due to the wavy water surface reattaching midway below the deck (*Ar* = 7.9) which reduces the negative vertical force of partial submergence regions.

The water level upstream and downstream of the bridge deviated from the undisturbed water level, as schematically shown in Fig. 2.12. Based on the water depth measured during experiments, the relative water depth variations (i.e., $R_h = (h_{u'} - h_{d'})/s$) were calculated and plotted against h^* and are shown in Fig. 2.13. In this relationship, $h_{u'}$ and $h_{d'}$ are the water depths just upstream and downstream of the bridge. The relative water depth variations in Fig. 2.13 indicates the differences in upstream and downstream water depths that lead to a dynamic pressure imbalance between the two sides of the deck. This phenomenon might explain the drag force on the bridge model.

The dependency of C_D on h^* at the constant Fr = 0.34 and Ar of 4.5 and 7.9 is presented in Fig 2.14a. The experimental results showed that the C_D increased up to 3.2 for the Ar = 7.9. Both decks showed a minimum C_D at h^*= 1, and the C_D decreased to 0.88 for Ar = 4.5. It is also evident from this figure that for $h^* \geq 1$, the bridge model with Ar = 7.9 produced a higher drag coefficient than the bridge with Ar = 4.5. From Fig. 2.13, it can be observed that the water surface elevation variation (R_h) was greater for the bridge model with an Ar = 7.9 than for the bridge model with Ar = 4.5, which produced larger drag for the bridge model with an Ar of 7.9. The numerical results presented by Zhong et al. (2019) that showed that a rectangular deck with a smaller aspect ratio (Ar =1) produces a greater drag coefficient than a deck with a higher aspect ratio (Ar = 3) are not in agreement with the experimental results of this study. In the current study, a deck with four equally spaced girders and an Ar = 4.5 and a deck with six equally spaced girders and an Ar = 7.9 affect the velocity field significantly and contribute to the generation of drag force (Naudascher and Medlarz 1983). This phenomenon is the reason for the difference between the C_D – Ar relationship for a rectangular deck presented by Zhong et al. (2019) and for the actual bridge deck in the present study.

Fig. 2.14b demonstrates the effects of Ar on C_L and shows that for both Ar values, the absolute value of C_L increases rapidly for $h^* < 1.25$ and then decreases gradually. It can also be observed from this figure that the C_L for the $Ar = 4.5$ bridge model was slightly higher than that of the deck with $Ar = 7.9$ under the same flow conditions. As h^* increased ($h^* > 1.25$), the negative pressure below the deck was equilibrated by the overflowing water on top of the deck, which reduced the negative C_L. Because of the larger deck width, this phenomenon was more significant for the bridge model with $Ar = 7.9$, which resulted in less negative C_L values.

The C_M variations for bridges with different Ars were plotted in Fig. 2.14c. For a narrow deck with an Ar of 4.5, the peak C_M was observed at $h^*=1$. Overall, the narrow deck had a slightly higher C_M for all inundation ratios than the wider deck ($Ar = 7.9$). The C_L values more negative for the deck with $Ar = 4.5$, which demonstrates that the C_M values of both deck types are affected by changes in the C_L values. Therefore, the greater C_L values of the narrow deck ($Ar = 4.5$) contributed significantly to producing larger C_M values.

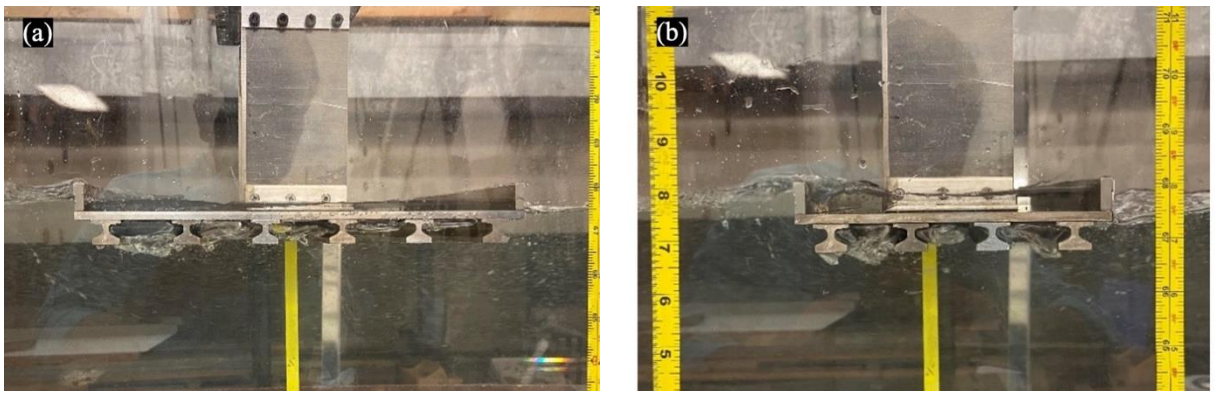

Fig. 2.10 Bridge superstructure scale models with blockage ratio $Br = 0.18$ and aspect ratio of: (a) $Ar = 7.9$ (six-girder bridge model), and (b) $Ar = 4.5$ (four-girder bridge model)

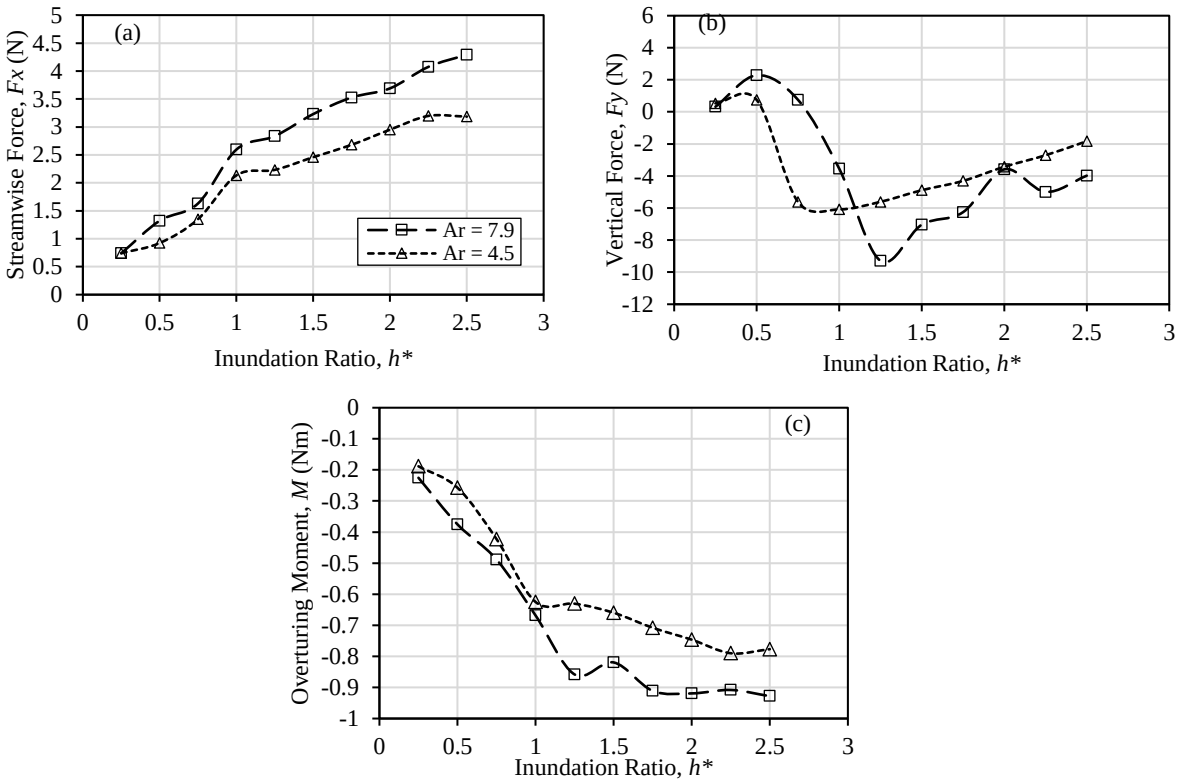

Fig. 2.11 Measured forces and moment for *Ar* of 7.9 and 4.5: (a) streamwise force (*Fx*), (b) vertical force (*Fy*), and (c) overturning moment (*M*)

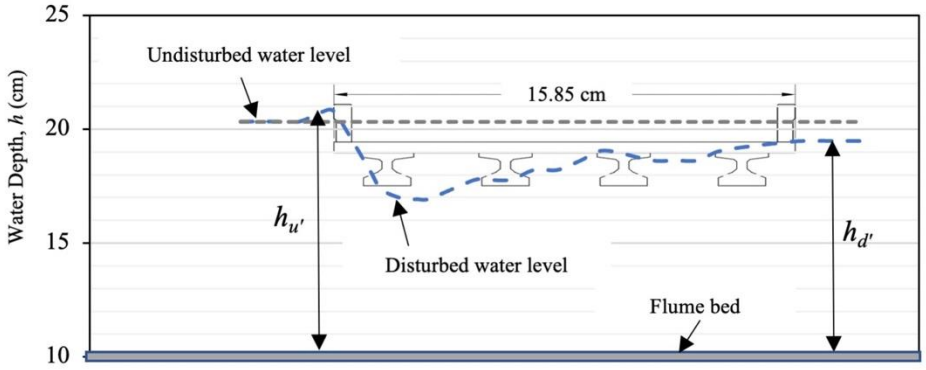

Fig. 2.12 Schematic of water surface profile at inundation ratio *h** = 0.75 for the four-girder bridge model (*Ar* = 4.5)

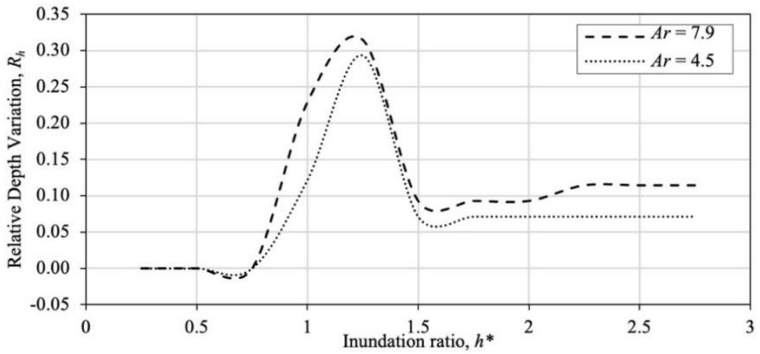

Fig. 2.13 Relative water depth (R_h) variation for four-girder bridge model (Ar = 4.5) and six-girder bridge model (Ar = 7.9)

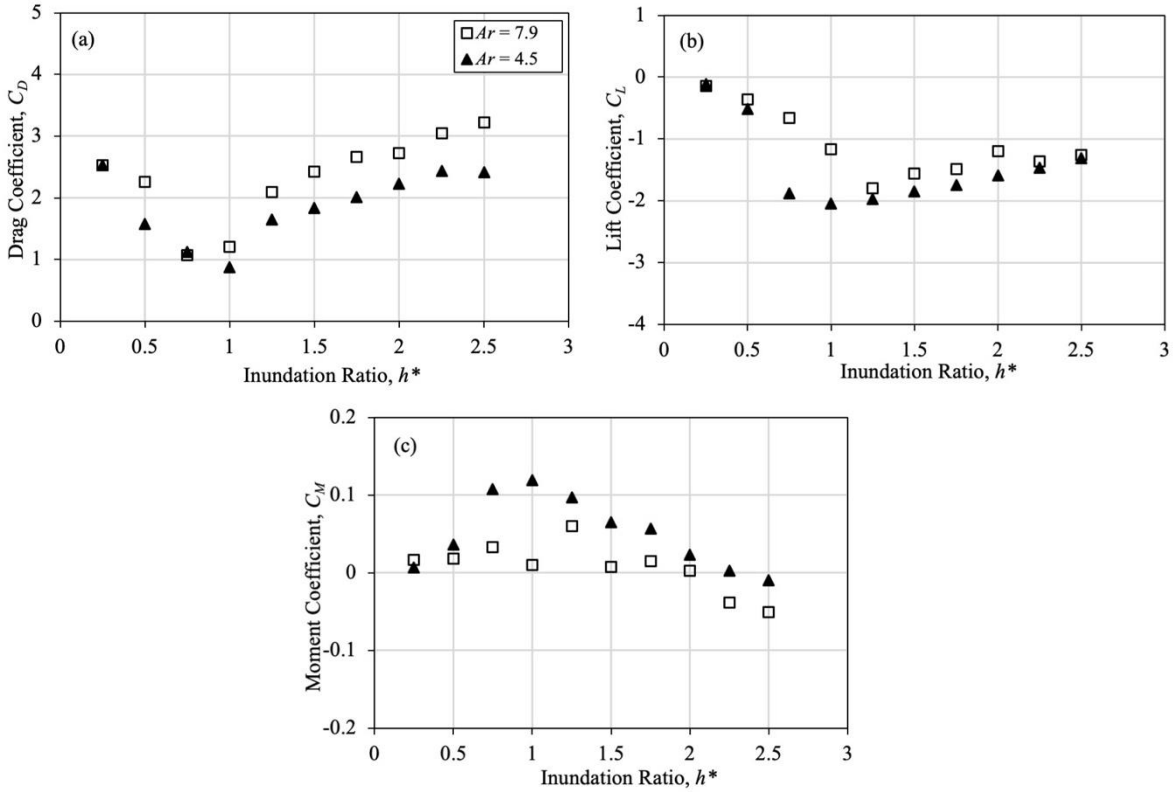

Fig. 2.14 Dependency of force and moment coefficients on the aspect ratio (Br): (a) drag coefficient (C_D), (b) lift coefficient (C_L), and (c) moment coefficient (C_M)

2.3.3.2 Flow Blockage Ratio

The girder height also makes an important contribution to the flow field. A previous study on the effect of a blockage created by a rectangular deck illustrated the significance of the blockage ratio on drag and lift coefficients (Chu et al. 2016). This section focuses on the effect of flow blockages

created by bridge girders on hydrodynamic forces, as well as force and moment coefficients. Two bridge models with I-girders of different heights were selected. The experiments were conducted on a four-girder bridge with a narrow deck (Ar = 4.5) and Fr of 0.27. The Br of the bridge models were 0.18 and 0.20 (Fig. 2.15). Fig. 2.16 (a-c) shows the measured streamwise force, vertical force, and overturning moment for both Br. It can be seen from this figure that a higher blockage ratio (Br = 0.20) produced a larger streamwise force, vertical force, and overturning moment than a lower blockage ratio (Br = 0.18), except for the vertical forces in the partial submergence region of both decks, where they responded to similar vertical forces. Fig. 2.17 illustrates the relative water depth variations for both blockage ratios. The flow blockage created by the bridge height disrupted the water depth upstream and downstream of the bridge. As can be seen from the figure, the relative water depth variation (R_h) was greater for Br = 0.20 due to the larger difference in the elevation of the water surface at the upstream and downstream sides of the deck. The force coefficients were calculated and compared for $h^* \geq 1$ to produce constant blockages for both models.

Fig. 2.18a demonstrates the relationship between the drag coefficient (C_D) and inundation ratio (h^*) at blockage ratios (Br) of 0.20 and 0.18 and shows that the C_D for the bridge model with a Br = 0.20 was greater than the bridge model with Br = 0.18 for fully submerged bridges ($h^* > 1$). The asymmetric flow depth at the leading and trailing ends of the bridge superstructure produced a dynamic pressure imbalance between the front and rear faces of the deck, as well as a greater drag coefficient for the bridge model with a larger Br, as the water level separation was greater. This result agrees with the study performed by Malavasi and Guadagnini (2007), which revealed that the drag coefficient, C_D, increases as the blockage ratio increases when $Br > 0.14$ and C_D remains constant (= 1.62) for $Br < 0.14$.

The dependency of C_L on Br is shown in Fig. 2.18b. The C_L shows slightly greater values for the bridge model with taller girders (Br = 0.20) due to the greater pressure imbalance created at the top and bottom sides of the deck during fully submerged conditions. Fig. 2.18c illustrates the effect of Br on C_M. The C_M values were slightly larger for the bridge model with a shorter girder (Br = 0.18). The combined actions of drag and lift forces produced smaller C_M values for the bridge with the taller girder (Br = 0.20) than the shorter one (Br = 0.18).

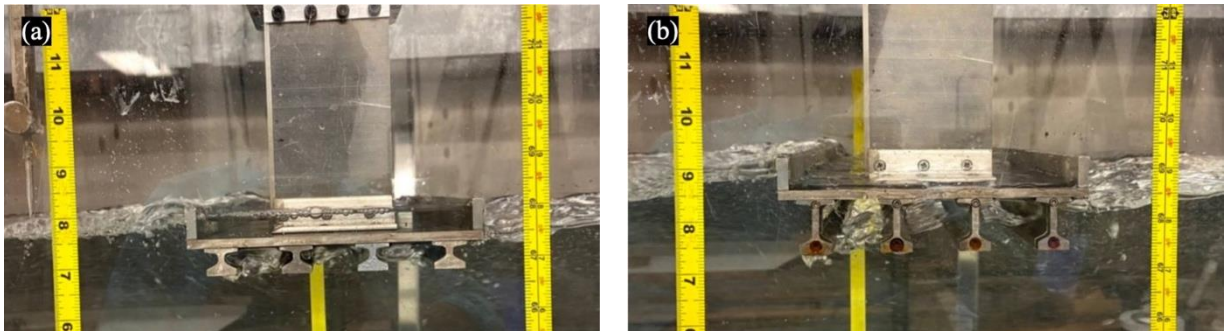

Fig. 2.15 Bridge superstructure scale models with blockage ratios of: (a) Br = 0.18 and (b) Br = 0.20 (Ar = 4.5, Fr = 0.27)

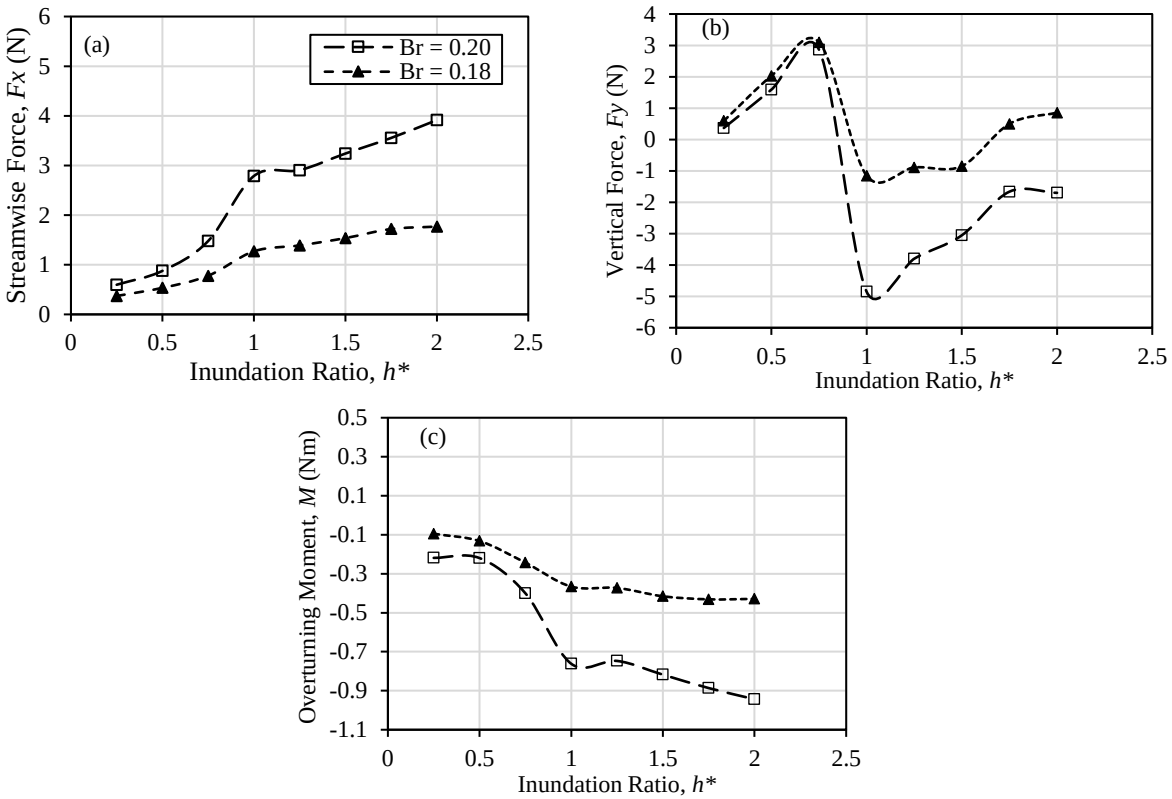

Fig. 2.16 (a) Streamwise force (*Fx*), (b) vertical force (*Fy*), and (c) overturning moment (*M*) on bridge deck with *Br* of 0.20 and 0.18

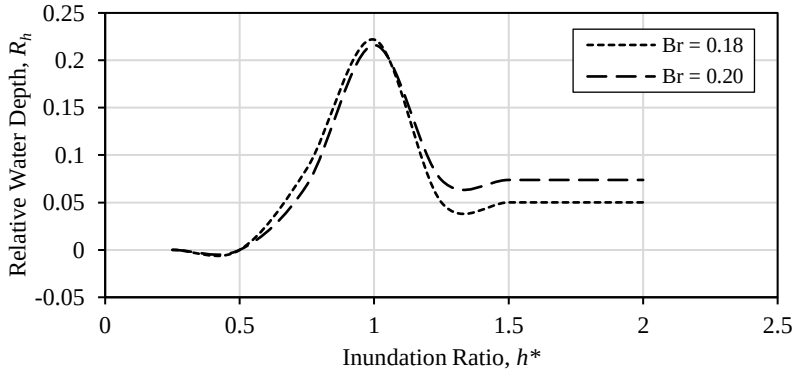

Fig. 2.17 Relative water depth (R_h) variation for blockage ratio (*Br*) of 0.20 and 0.18

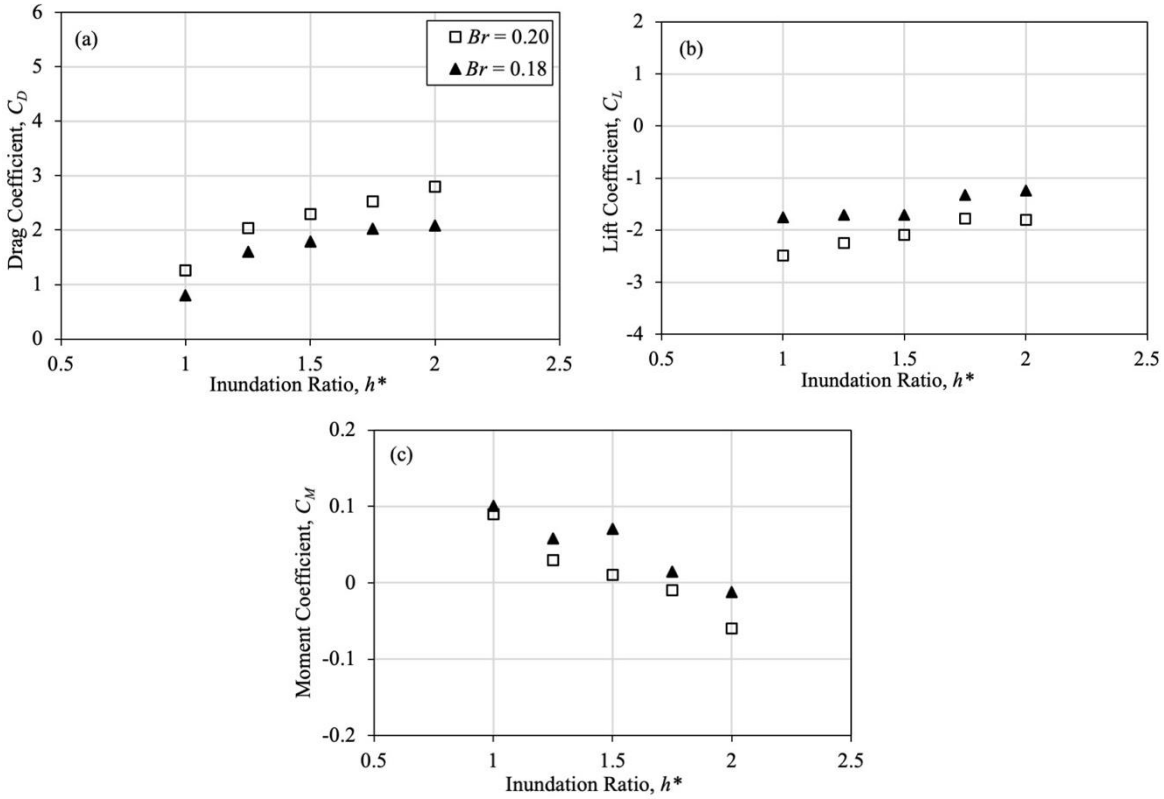

Fig. 2.18 Dependency of force coefficients on the blockage ratio (*Br*): (a) drag coefficient (C_D), (b) lift coefficient (C_L), and (c) moment coefficient (C_M)

2.3.3.3 Girder Shape

The geometry of bridge girders/beams also impact the flow field around submerged bridges.; therefore, this section focuses on how it affects the force and moment coefficients. The force and moment coefficients were studied by comparing the values of drag, lift, and overturning moment coefficients for an I-girder and a box beam with the same submergence ratio and flow conditions.

The I-girder was comprised of flanges at the top and bottom and a web in the middle (Fig. 2.19a); the box beam was a hollow square-shaped beam with exterior edges that was filled with foam material to prevent water intrusion (Fig. 2.19b). The I-girder and box beam bridge models had the same blockage ratio (*Br* = 0.18) and aspect ratio (*Ar* =7.9) and were simulated under the same flow

condition with Fr = 0.34. Fig. 2.20 (a-c) depicts the streamwise force, vertical force, and overturning moment on the deck of both girders, where it can be seen that the deck of the I-girder experienced stronger streamwise and vertical force than that of the box beam. On the other hand, the measured overturning moment was larger for the box beam than for the I-girder.

Fig. 2.21 shows the R_h variations for the I-girder and box beam and illustrates the asymmetry between the upstream and downstream flow depths for both bridge models. R_h reached as high as 0.22 for the I-girder, but only 0.11 for the box beam. The water surface upstream and downstream of the deck of the box beam was less disturbed, as the box beam resembles a rectangular deck with no hollow spaces below the deck to disturb the flow. On the other hand, the water level for the I-girder bridge deck was significantly higher upstream of the deck and abruptly dropped on the downstream side as a result of its less streamlined shape.

Figs. 2.22 compares the experimental results of the force and moment coefficients for both geometries. The plot of the drag coefficient (C_D) against the inundation ratio (h^*) shows that C_D is a function of the shape of girders/beams (Fig. 2.22a). Due to the larger R_h variation in the I-girder, it experiences a larger dynamic pressure imbalance between the front and rear end of the deck, which creates a wider wake region for the I-girder and is responsible for the greater C_D for the I-girder. Fig. 2.18b illustrates the dependency of C_L on bridge geometry by showing that the I-girder and box beam produced similar C_L values. This is because the dynamic pressure between the top and bottom of the deck was similar for both types of bridge models. Fig. 2.22c depicts the dependency of C_M values on the shape of girders/beams. The maximum moment coefficient was observed for the box beam at inundation ratio of $h^* = 1$, and the combined effects of the drag and lift force caused the greater C_M for the box beam.

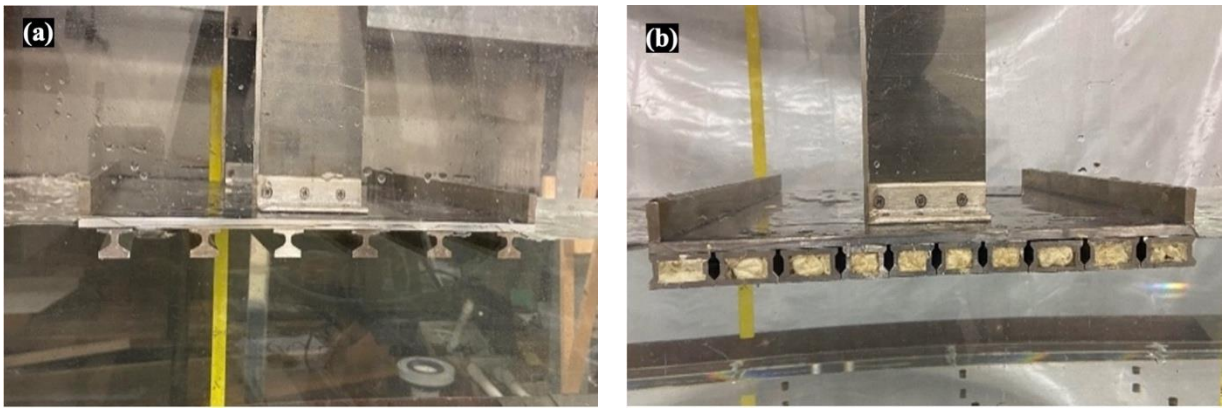

Fig. 2.19 Bridge superstructure scale models with (a) I-girder, (b) box beam

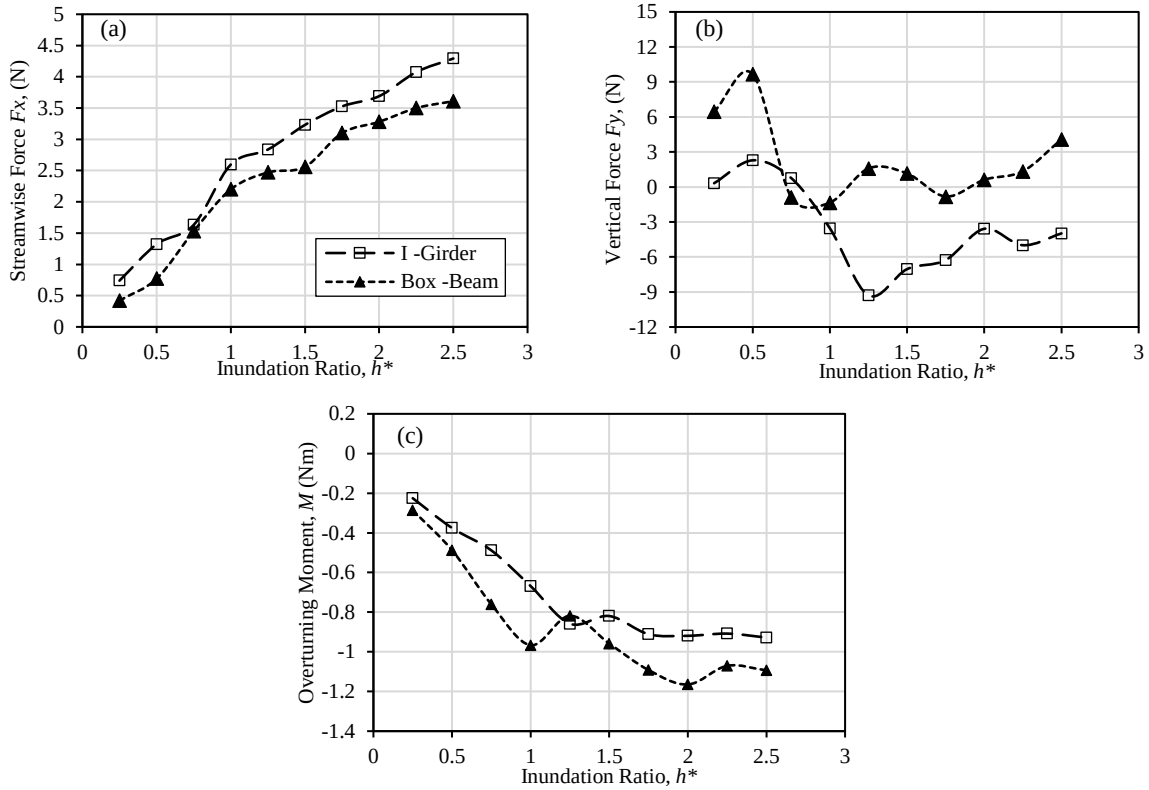

Fig. 2.20 Measured forces and moment for I-girder and box beam: (a) streamwise force (*Fx*), (b) vertical force (*Fy*), and (c) overturning moment (*M*)

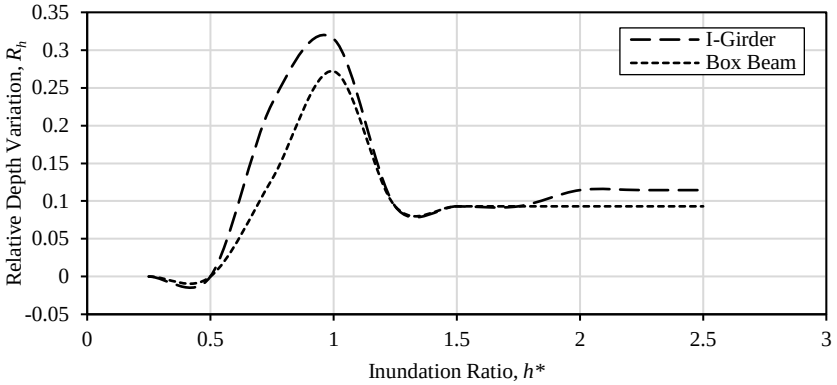

Fig. 2.21 Relative water depth (R_h) variations for I-girder and box beam shapes

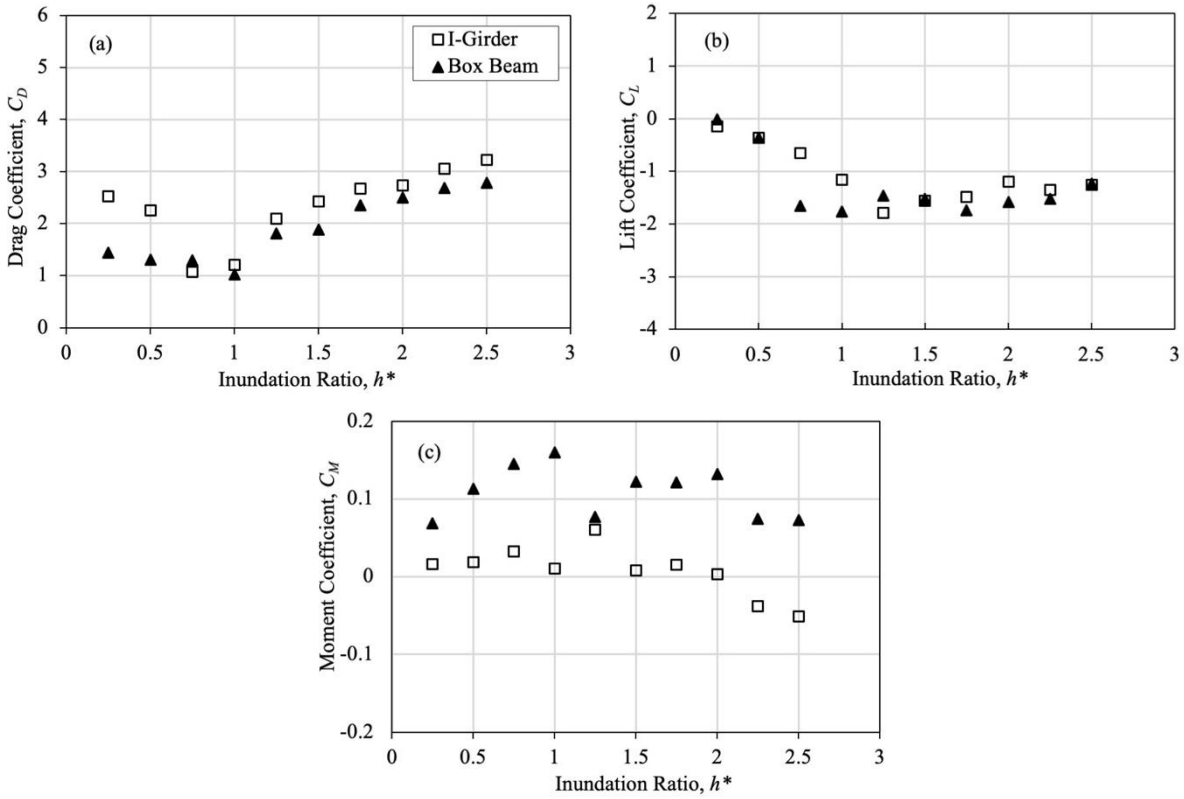

Fig. 2.22 Dependence of the force coefficients on the girder shape: (a) drag coefficient (C_D) (b) lift coefficient (C_L), and (c) moment coefficient (C_M)

2.4 CONCLUSION

Knowledge of the interactions between bridge superstructures and flood flow conditions is critical to understanding hydrodynamic forces on bridges, and the two key features to be considered are

the flow parameters and the geometry of the bridge. These aspects were investigated in this study in terms of their effects on the drag, lift, and moment coefficients. Small-scale bridge models were developed to reproduce typical geometric and flow conditions in the laboratory, and changes in the hydrodynamic forces and moment coefficients were examined against the proximity ratio, inundation ratio, Froude number, aspect ratio, blockage ratio, and girder shapes. The proximity ratio experiments on a typical four I-girder bridge superstructure confirmed that the position of the bridge deck with respect to the streambed greatly influences the force and moment coefficients. There were minimal-to-no effects on the C_D, C_L, and C_M when a proximity ratio of 3 or greater was selected. The experimental results revealed that an increase in the *Fr* reduces the force and moment coefficients due to the reduction in the fluid-structure interaction area. It was also observed that the coefficients of the drag, lift, and moment were significantly affected by the inundation ratio (h^*), especially in the transition from partially- to fully submerged states, i.e., h^*= 0.75 – 1.25.

The experimental results showed that the force and moment coefficients can be affected by the aspect ratio, flow blockage, and shapes of the bridge superstructures. The water surface on the upstream and downstream of the bridge deck varied with the bridge geometry, which contributed to the variations in the force coefficients. The difference in the relative water depth of the area upstream and downstream of the deck was greater, which created a pressure imbalance on the deck and produced higher drag force coefficients (C_D). Because of this phenomenon, the I-girders produced greater C_D than the box beam with the same blockage and aspect ratio and Froude number. The lift coefficient (C_L) showed a slight variation with a change in the aspect ratio (*Ar*), where more negative C_L values were observed for a smaller *Ar*. There was no significant difference in the C_L of the two types of girders, due to similar dynamic pressure variations on the upper and

lower sides of the deck. Therefore, it could be concluded that C_L is minimally affected by the shape of the girder with the same deck width. The C_L varied, however, with changes in the *Br*, due to differences in the pressure on the top and bottom of the deck. The narrow deck ($Ar = 4.5$) produced a higher moment coefficient (C_M), but with slight dominance by the lift force, at the center of gravity of the superstructure due to the combined actions of the drag and lift forces. The blockage ratio showed no significant variation for C_M. The box beam produced greater C_M than the I-girder, due to the combined actions of the drag and lift coefficients on the deck. Therefore, it may be concluded that the magnitude of the moment coefficient is highly dependent on the shape of girders/beams.

Based on the outcome of these experiments, it can be concluded that it is essential to consider the effects of the proximity ratio, the Froude number, and the type of superstructure when designing river-crossing bridges. Further studies using flow visualization techniques are necessary to fully explain the characteristics of C_D, C_L, and C_M and to better understand the nature of flow around different bridge geometries. This study provides a great deal of information on the effects of bridge geometry and flow parameters on hydrodynamic force and moment coefficients, thus improving our understanding of this area of research and providing new ground for further experiments.

Acknowledgments

This research was made possible through funding from the Texas Department of Transportation (TxDOT): Project Number 0-7068. The authors would like to thank Chris Glancy, Martin Dassi, and the TxDOT research team for their support and technical discussions.

Notations

The following symbols are used in this paper:

A = Projected area of the submerged object

A_D = projected area of the submerged bridge normal to the flow

A_L = Projected area of the submerged bridge parallel to the flow

Ar = Aspect ratio

Br = Blockage ratio

C_D = Drag coefficient

C_L = Lift coefficient

C_M = Moment coefficient

F_B = Buoyant force

F_D = Drag force

F_h = Hydrostatic force

F_L = Lift force

Fr = Froude number

F_S = Deck Froude number

g = Gravitational acceleration

h_b = Distance from the streambed to the low chord of the girder

h_u = Depth of the water

$h_{u'}$ = Depth of elevated water surface at the upstream side of the deck

$h_{d'}$ = Depth of the dropped water surface at the downstream side of the bridge

h^* = Inundation ratio

L = Length of the bridge

M_{cg} = Overturning moment

Pr = Proximity ratio

R = Reynolds number

s = Height of the bridge superstructure

R_h = Relative water depth variation

V = Depth-averaged approach flow velocity

W = Width of the bridge

ρ_w = Water density

$\forall$ = Volume of submerged bridge elements

References

Almasri, A. and Moqbel, S. 2017. Numerical evaluation of AASHTO drag force coefficients of water flow around bridge piers. *Journal of Engineering Materials and Technology*, 139(2).

Ahamed, T., Duan, J.G. and Jo, H. 2020. Flood-fragility analysis of instream bridges–consideration of flow hydraulics, geotechnical uncertainties, and variable scour depth. Structure and Infrastructure Engineering, pp.1-14.

Byrne, K. Major. Flooding on Llano River triggers bridge collapse near Kingsland, Texas [Online] Available at: https://www.accuweather.com/en/weather-news/major-flooding-on-llano-river-triggers-bridge-collapse-near-kingsland-texas/342859 [Accessed: 2 February 2020]

Chu, C.R., Chung, C.H., Wu, T.R. and Wang, C.Y., 2016. Numerical analysis of free surface flow over a submerged rectangular bridge deck. *Journal of Hydraulic Engineering*, 142(12), p.04016060.

Fang, Q., Hong, R., Guo, A., Stansby, P.K. and Li, H., 2018. Analysis of hydrodynamic forces acting on submerged decks of coastal bridges under oblique wave action based on potential flow theory. Ocean Engineering, 169, pp.242-252.

Fechter, J. 2015. TxDOT: Two bridges completely wrecked in Central Texas floods, others damaged [Online] Available at: https://www.mysanantonio.com/news/local/article/TXDoT-Two-bridges-wrecked-in-the-Central-Texas-6294892.php [Accessed: 2 March 2020].

FHWA (Federal Highway Administration). 2009. Bridges, structures, and hydraulics. 23 CFR 650, subpart C.

Flint, M.M., Fringer, O., Billington, S.L., Freyberg, D. and Diffenbaugh, N.S. 2017. Historical analysis of hydraulic bridge collapses in the continental United States. *Journal of Infrastructure Systems*, 23(3), p.04017005.

Jempson, M., 2000. Flood and debris loads on bridges. (Doctoral thesis), University of Queensland.

Jordan, B. 2015. Analysis of bridges subjected to flood loadings based on different design standards. (Bachelor dissertation) The University of Southern Queensland. Australia.

Kosa, K., 2014. Damage analysis of bridges affected by the tsunami in the Great East Japan Earthquake. *Journal of JSCE*, 2(1), pp.77-93.

Malavasi, S. and Guadagnini, A. 2003. Hydrodynamic loading on river bridges. *Journal of Hydraulic Engineering*, 129(11), pp.854-861.

Malavasi, S., Franzetti, S. and Blois, G., 2004, June. PIV investigation of flow around submerged river bridge deck. In Proceedings of the International Conference of River Flows, Napoli, Italy (pp. 601-608).

Malavasi, S. and Guadagnini, A., 2007. Interactions between a rectangular cylinder and a free-surface flow. *Journal of Fluids and Structures*, 23(8), pp.1137-1148.

Nasim, M. 2019. Damage modelling of reinforced concrete bridge piers under flood and log impact (Doctoral dissertation), RMIT University.

Naudascher, E. and Medlarz, H.J., 1983. Hydrodynamic loading and backwater effect of partially submerged bridges. *Journal of Hydraulic Research*, 21(3), pp.213-232.

Oudenbroek, K., 2018. Experimental research on hydrodynamic failure of river bridges on spread footings. (Master's Thesis) Delft University of Technology, Delft, The Netherlands.

Sousa, J.J. and Bastos, L. 2013. Multi-temporal SAR interferometry reveals acceleration of bridge sinking before collapse. Natural Hazards and Earth System Sciences, 13(3), pp.659-667.

Taricska, M., 2014. An analysis of recent bridge failures (2000-2012). (Master Thesis) Ohio State University.

Thai, T.K.C., 2019. Numerical simulation of the turbulent flow over submerged bridge decks. *Magazine of Civil Engineering*, 85(1).

Wardhana, K. and Hadipriono, F.C. 2003. Analysis of recent bridge failures in the United States. *Journal of Performance of Constructed Facilities*, 17(3), pp.144-150.

Zhong, W., Deng, L. and Xiao, Z., 2019. Flow past a rectangular cylinder close to a free surface. Ocean Engineering, 186, p.106118.

CHAPTER 3

INVESTIGATION OF FLOW DYNAMICS AROUND SUBMERGED BRIDGES

Abstract

Floods are the most common cause of bridge failures, thus studies of bridge superstructures' hydrodynamic properties and how they interact with floods are essential for designing safe and resilient bridges. Current research on the interactions between flow and bridges is limited to the study of flow around generalized rectangular cylinders; therefore, this study aims to investigate the flow field around submerged bridge decks with typical bridge geometry to establish relationships between the flow field and hydrodynamic force coefficients. We examine the structure of flow around scale bridge models in a laboratory setting, using particle image velocimetry (PIV), and conduct experiments with Froude numbers of 0.20 and 0.34 and inundation ratios of 0.5, 1.0, and 1.5 (i.e., transition from partially to fully submerged conditions). PIV data was utilized to estimate the mean velocity field, streamlines, and flow structures (i.e., separation, wake region, reattachment, and vortices). The dimensionless parameters of flow kinematics were also estimated from the PIV data to develop a relationship with the hydrodynamic forces applied to different bridge geometries. The results of this study indicate that hydrodynamic force coefficients are significantly influenced by the extent of the wake region and the presence of vortices within it. These findings support the long-standing belief expressed by many prominent researchers that the formation of a flow separation region is directly related to the hydrodynamic forces of submerged decks.

Keywords: PIV Measurements, Extreme Flood Events, Bridge Design, Hydrodynamic Force Coefficients, Flow Structure

3.1 INTRODUCTION

Climate change and the recent increase in urbanization have resulted in more frequent extreme riverine and coastal flooding (NRC 2008, Wright et al. 2012, Gill et al. 2007, Yoon et al. 2019), causing river-crossing bridges to become partially or fully submerged. The interaction between the flow and the bridge superstructure is known as pressure flow conditions for partially submerged cases and weir flow conditions for fully submerged conditions. The bridge deck intensifies the velocity and changes the flow and turbulence around bridges by restricting the flow conveyance (Carnacia et al. 2019). Flow field distortion affects the pressure distribution as well as the forces acting on submerged bodies (Malavasi and Blois 2007).

The flow characteristics around rectangular cylinders have been widely investigated, revealing that a rectangular deck acts as a bluff body when is fully submerged. Depending on the flow characteristics, the boundary layer around a bluff body may include the following zones: *separation points, stagnation points, reattachment point, and wake area* (Naderi 2018). Separation points on a submerged deck occur where the flow boundary layer separates from the submerged body – in this case, the upstream edges of the deck. The stagnation point is where the maximum pressure occurs, and the fluid velocity is zero. A reattachment point is where the boundary layer either reattaches to a solid surface or re-consolidates with the channel flow. The wake area is defined as the low-pressure area that is created when the boundary layer separates from the solid body. Fig. 3.1 shows the schematics of flow characteristics around a rectangular bluff body.

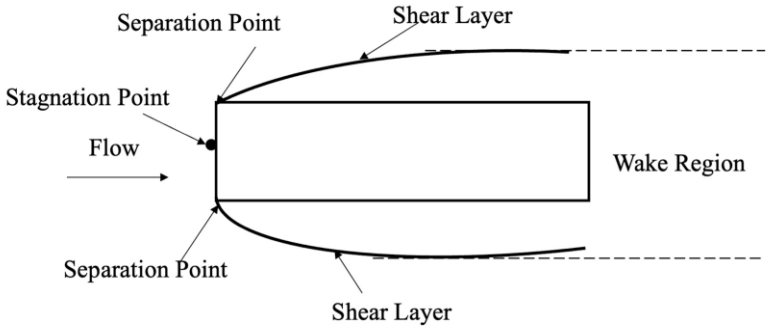

Fig. 3.1 Schematics of flow characteristics around rectangular bluff bodies (Adopted from Jempson 2000)

The magnitude of the drag force acting on a simple bluff body is proportional to the size of the wake region, i.e., the wider the wake the greater the drag force. Flow separation is also responsible for vortices or eddies in the wake region (Malavasi and Blois 2004, Bushra 2010). The formation and development of vortices tend to dominate the progression of the drag and lift on the bridge deck (Liaw 2005); however, the flow separation, reattachment, distribution of vortices along the surface of the deck, and hydrodynamic forces may depend on the incident flow conditions, deck submergence, geometry of the immersed body, and the downstream pressure distribution (Jempson 2000, Bushra 2010, Lin et al. 2012, Arslan et al. 2013).

Flow structure characteristics become more complicated with an increase in the complexity of the geometry of the submerged object. The bridge deck attachments (i.e., barriers, railings, and girders) disturb the boundary layer considerably and affect the hydrodynamic characteristics of the bridge deck. Naudascher and Medlarz (1983) measured the drag coefficient of a girder bridge and found that the wave motion and vortex formation between the girders created a peak loading on the bridge deck. An increase in the overall degree of bluffness of the bridge deck increases the drag force and decreases the lift force of streamlined bridge decks (Bruno and Mancini 2002, Laima et al. 2018). Therefore, it is imperative to investigate flow characteristics around submerged

bridge decks to determine the drag and lift coefficients and establish their relationship with the mean flow field.

In recent years, researchers used PIV techniques to explore the interaction of flow and submerged bridge decks, either by conducting flow field investigations on rectangular bluff bodies as an idealized shape of bridge decks, or by conducting flow field investigations on scale models of bridge decks with actual geometry. Table 3.1 presents a list of previous research related to the interaction between flood flow and bridge decks of any form.

Table 3.1 Summary of Studies Conducted on Velocity Fields around Bridge Decks using PIV

Authors	Bridge structure	Features studied	Measurements or analysis items
Lin et al. (2012)	Girder and rectangular bridge	Shear layer, vortices within the shear layer	• Flow structure under the bridge deck was categorized based on the flow parameters. • Non-dimensional mean streamwise velocity profiles were developed at different streamwise distances.
Bushra (2010)	Girder and streamlined bridge deck	Streamlines, velocity contours	• Simulated velocity contours were compared with the measured velocity contours from PIV. • Velocity profiles of 3- and 6-girder bridges were compared.
Malavasi and Blois (2007)	Rectangular cylinder	Mean flow structures	• Influence of the submersion on the dimension of the main vortex structure was determined. • Topological structure of the flow field was compared with the hydrodynamic loading of the cylinder.
Malavasi et al. (2004)	Rectangular cylinder	Large scale vortex, mean and time-averaged velocity fields	• Characteristics of the large-scale vortex were studied in the bridge wake. • Mean flow structure (i.e., separation bubble) was associated with the downward lift coefficient.

Despite the need for a solution to the problem, few researchers have investigated the flow field around rectangular bridge models and measured its effects on the hydrodynamic force coefficients.

Malavasi et al. (2004) investigated a flow field structure around a rectangular bridge deck and showed that the frequency of vortex formation is directly related to the frequency of lift force generation; however, they were unable to show a relationship between the hydrodynamic drag force coefficients and the behavior of the flow field. In another study, Malavasi and Blois (2007) demonstrated a line detection algorithm to represent the structural elements of the flow (i.e., velocity vectors, vortex structure), which established a good agreement between the kinematic parameters of the flow and the hydrodynamic force coefficients. No studies have been conducted, however, to investigate flow structures on actual bridge superstructures and estimate their effect on hydrodynamic force coefficients.

Understanding the hydrodynamic behavior of bridge superstructures under the effect of flood flow is an important consideration for the design of river-crossing bridges; however, the behavior of actual bridges has not been sufficiently studied. This research aims to investigate the flow characteristics of fully and partially submerged bridge superstructures under a variety of hydrodynamic and geometric conditions, focusing on three objectives: (i) determining the characteristics of the mean flow field for a submerged bridge deck, (ii) developing correlations between hydrodynamic force coefficients and dimensionless geometric parameters of flow kinematics, and (iii) studying the effect of flow structures on the geometric variations of bridge decks.

3.2 METHODOLOGY

3.2.1 Experimental Setup and Conditions

The experimental data used in this study were acquired from a plexiglass flume with dimensions of 4.88-m long, 0.3-m wide, and 0.5-m deep. A valve regulated the flow rate, and the flow was

measured with a digital SonoTrac ST30 ultrasonic flowmeter that had an estimated uncertainty of ± 0.5% and was attached to the flume's inlet line. The water depth was measured with a point gauge with a precision of ± 0.002m and was adjusted by a tailgate that was placed at the end of the flume. The water in the flume flowed from left to right. A photo of the experimental setup is shown in Fig. 3.2. Details of the maximum error associated with each measurement are illustrated in Appendix A. The upstream water level (h_u) was measured 0.3m upstream of the leading edge of the bridge deck, where the backwater effect due to the presence of the bridge was negligible. The upstream undisturbed velocity *(V*) was calculated using the flow rate (*Q*) and the flow cross-sectional area ($A = L \times h_u$) at the reference section (where *L* is the channel width).

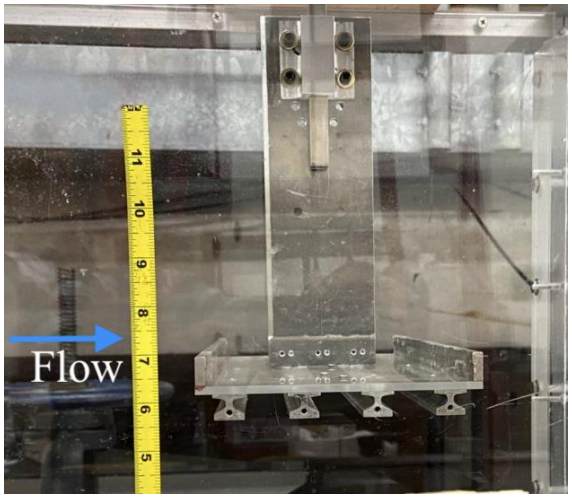

Fig. 3.2 Photo of the experimental setup

Different hydrodynamic conditions were applied to a superstructure model of a typical river-crossing bridge to investigate the flow characteristics around it. The application of physical modeling in any research requires that geometric and dynamic similarities be maintained. In this research, the geometric similarity was maintained by reducing the size of the bridge elements by 1/50 (i.e., 50 times smaller than the prototype). In open-channel flows, inertia and gravity forces

predominate over viscous forces, thus Froude number scaling was applied to obtain dynamic similarity. Reynolds number (*Re*) scaling cannot be satisfied simultaneously with the Froude number in modeling open channel flows, but the Reynolds number is sufficiently large in fully turbulent flows ($Re > 10^4$), such as in this experiment, that the force coefficients are relatively insensitive to variations of the Reynolds number (Oudenbroek 2018). Fig. 3.3 presents the schematic of the typical I-girder bridge model used in this study, in which bridge models were attached to a square rod that was connected to a crossbeam resting on top of the flume. A minimum gap between the deck sides and the flume walls prevented friction between the bridge and the flume walls.

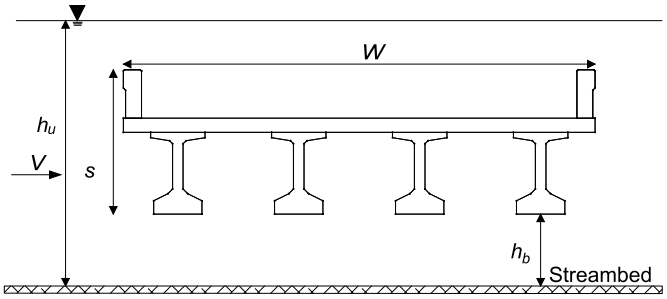

Fig. 3.3 Schematic of a bridge superstructure and definition of flow and bridge geometry parameters

Four hydraulic and geometric parameters were used for the experiments: (i) Froude number ($Fr = V/\sqrt{g h_u}$, where V is the average approach velocity, g is the gravitational acceleration, and h_u is the upstream flow depth; (ii) inundation ratio ($h^* = (h_u - h_b)/s$, where, h_b is the distance from the channel bottom to the girder soffit, and s is the height of the bridge superstructure); (iii) blockage ratio ($Br = s/h_u$); and (iv) aspect ratio ($Ar = W/s$, where W is the width of the bridge superstructure).

The different geometric parameters of the bridge superstructures were studied for two deck widths (26-ft. and 46-ft.), two girder heights (TX28 and TX54), and two girder shapes (I-girder and box

beam). Detailed drawings of the bridge models are presented in Appendix B. Table 3.2 describes the bridge models and their associated geometric parameters.

Table 3.2 Experimental Conditions for All Bridge Deck Scenarios

Model Description	*Ar*	*Br*
Four TX28 I-girders with 26-ft deck	4.5	0.18
Four TX54 I-girders with 26-ft deck	4.5	0.20
Five BB28 box beams with 26-ft deck	4.5	0.18
Six TX28 I-girders with 46-ft deck	7.9	0.18

The hydrodynamic forces on submerged bridges are usually presented in the form of dimensionless drag and lift coefficient. The drag force coefficient is a non-dimensional value that is the ratio of the drag force to the product of the free stream dynamic pressure and wetted area. Eqn. 3-1 can be used to calculate the drag force coefficient.

$$C_D = \frac{F_D}{(0.5\rho V^2)A_D} \tag{3-1}$$

where F_D is the drag force due to the dynamic pressure imbalance between the upstream and downstream of the deck, A_D is the wetted area in the direction of the flow, and ρ is the water density.

Similarly, the lift force coefficient (C_L) can be calculated using Eqn. 3-2.

$$C_L = \frac{F_L}{(0.5\rho V^2)A_L} \tag{3-2}$$

where, F_L is the lift due to the difference in the dynamic pressure between the top and bottom surface of the deck, and A_L is the wetted area perpendicular to the flow direction.

3.2.2 PIV Setup

PIV is a non-intrusive technique that is used to measure the flow velocity in fluids. A PIV system is usually composed of a continuous source of light, a highspeed camera, and seeding particles. This study developed a low-cost PIV system to investigate the flow characteristics around submerged bridges. The PIV system included a laser light, a GoPro camera, dust particles as seeding particles, and a mirror to reflect the light. Fig. 3.4 shows a schematic of the experimental setup with the PIV system.

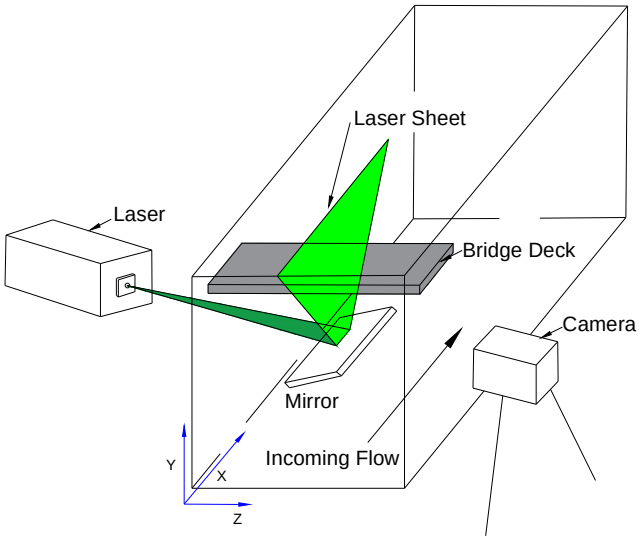

Fig. 3.4 Schematic of the experimental setup and PIV system

The light source was a 1-watt power green laser that was connected to a cylindrical lens and produced a laser sheet at the measurement section. The sheet was 2-mm thick and reflected towards the bridge test section. The images were captured with a GoPro action video camera equipped with 28-mm focal length and a narrow field of view (FOV). The maximum achievable frame rate for a narrow field of view is 240-Hz with a pixel resolution of 1280×720. The average acquisition time was kept at 30 seconds, which corresponds to 7200 images. Silver powder particles with a mean diameter of 47 microns and density of 2.04 g/cm^3 were used to evidence the fluid motion. The

settling velocity of the silver particles estimated from the Stokes' law was about 0.125 cm/s, which was much smaller than the average flow velocity used in the present study (250 cm/s).

A MATLAB extension tool, PIVLab, was employed to analyze the velocity data obtained from the video recording during the experiment. Two images (e.g., A and B) of the illuminated plane were captured at times t_0 and $t_0 + \Delta t$. Therefore, the velocity in the illuminated area was calculated from Δt and the distance that the particles traveled from image A to B. The particle displacement was calculated for a group of particles by evaluating the cross-correlation of many small-sub-images (interrogation areas) (Thielicke and Stamhuis 2014).

3.2.3 Flow Characterization Methods

The feature-based approach has been used in past research to study the flow characteristics around submerged bridge decks (Malavasi and Blois 2007, Perry and Chong 1987). The concept of a feature can be defined as a pattern found in data relevant to a specific research or engineering problem. It can be a phenomenon, a structure, or an object. Vortices, boundary layers, wake and recirculation flow regions, attachment points, and separation lines are examples of flow features. The main classification of features for a vector field is derived from topology and critical point theory (Malavasi and Blois 2007, Perry and Chong 1987). Critical points, i.e., points in the flow field where the velocity is zero and the streamline slope is indeterminate, can be used as a qualitative description of the topology of the velocity field and instantaneous streamline patterns (Chong and Perry 1994). With the use of feature lines, it is possible to visualize complex flow structures by simplifying and quantifying them as lines and points. The following method, used in this research to estimate the feature lines from the complex flow field, was adapted from the work of Malavasi and Blois (2007) and is described below.

The flow separation and re-attachment to a submerged solid body occurs when the flow abruptly leaves or returns to the submerged body. The separated region produces a wake of recirculating flow on the lateral regions of the submerged solid objects. Fig. 3.5 depicts the characteristic lines adopted for studying the recirculating flow within the wake region. Flow separation lines (*FSLs*) are defined by identifying the vertical profile of time-averaged velocity at locations such as upstream and downstream of the deck and between girders or girder chambers. The *FSL* connects the zero-velocity point on the velocity profile across the width of the deck on both the top and bottom and separates the reverse flow in the wake region from the upstream flow. The point in the lateral region where the *FSL* reattaches to the top or bottom of the deck is called the reattachment point (*RP*).

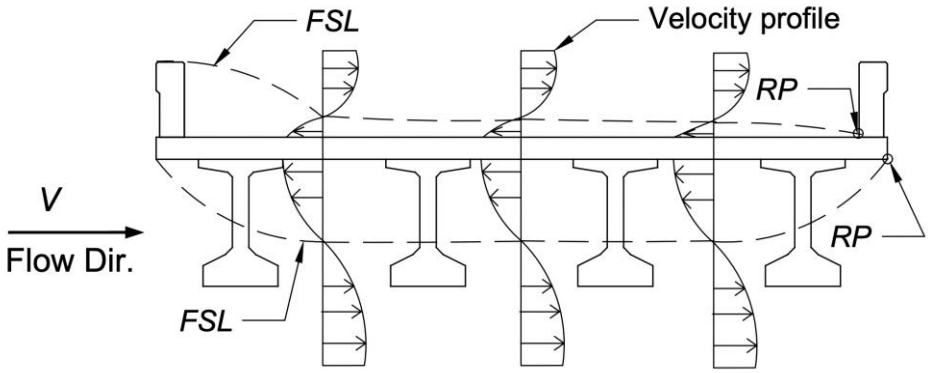

Fig. 3.5 Schematic representation of flow structure on top and bottom of a bridge deck

The parameters of flow kinematics can be identified by using the characterized flow feature lines and the point of reattachment. Several significant points in the *FSL's* graphical representation, such as the vertex point and the reattachment point, may be utilized to geometrically describe the flow structure. Fig. 3.6 shows the details of the flow separation lines and points (i.e., *VP* and *RP*).

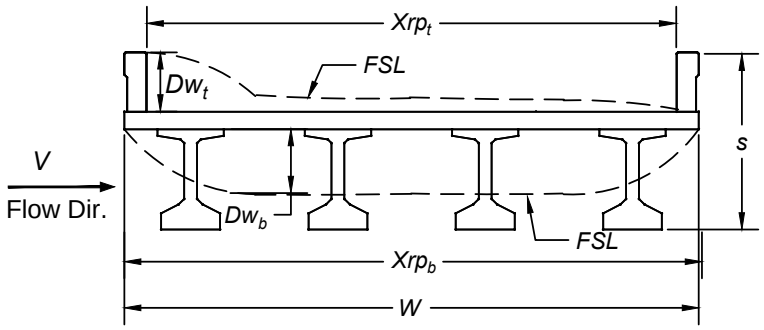

Fig. 3.6 Examples of flow lines and reattachment locations

Researchers have found that the vertical dimension of a wake correlates with the drag force coefficient (e.g., Malavasi and Blois 2007). The vertical dimension is the sum of two vertical distances: (i) the maximum vertical distance from the top face of the deck to the most external point (i.e., vertex point) of the *FSL* (Dw_t) and (ii) the maximum vertical distance from the bottom face of the deck to the most external point below (Dw_b). The vertical dimension of the wake region (Dw) can be expressed by Eqn. 3-3.

$$Dw = Dw_t + Dw_b \tag{3-3}$$

In order to normalize this transversal size of the wake, the width of the wake region (Dw) is divided by the height of the superstructure (s). The normalized wake width (d^*) can be expressed by Eqn. 3-4.

$$d^* = \frac{Dw}{s} \tag{3-4}$$

Similarly, the horizontal length of the wake region has been correlated with lift force coefficients (Malavasi and Blois 2004 & 2007). The horizontal dimension of the bubble formation or wake region length is calculated by determining the length of the flow reattachment (X_{RP}) on the top and bottom of the deck - the horizontal distance from the upstream edge of the railing to the

reattachment point (*RP*) on the deck surface. The difference between the horizontal extension of the wake region on the top and bottom of the deck can be calculated using Eqn. 3-5.

$$Rp = Xrp_t - Xrp_b \tag{3-5}$$

where *Rp* represents the difference in the horizontal distance between the leading edge and the reattachment point, X_{rp} is the x coordinate of the reattachment points, and the subscripts *t* and *b* represent the top and bottom of the deck, respectively. *Rp* is normalized by dividing it by the width of the deck (*W*). The dimensionless length of the recirculating flow in the separation region can be expressed by Eqn. 3-6.

$$R^* = \frac{Rp}{W} \tag{3-6}$$

3.3 RESULTS AND DISCUSSION

3.3.1 Flow Field Around Bridge Models

An analysis of the characteristics of a flow field generated by the interaction between free surface flow and typical bridge geometry is presented in terms of velocity vectors, streamlines, and the representation of velocity contours. This study aimed to estimate the minimum time required to achieve a stable velocity profile and evaluate the vortices or reverse flows that occur at various locations along the bridge, such as upstream and downstream from the bridge and between the girders or girder chambers.

3.3.1.1 Flow Structure Around Submerged Bridge Decks

The experimental data presented in this section evaluates the stability of streamlines around submerged bridge decks. The minimum period (timestep) is selected when the velocity contours and streamlines are stable. PIV images were used to extract the velocity contours around the bridge models in order to assess the stability of the streamlines around submerged decks. The streamlines were drawn from the velocity vector data in the PIVLab software. Fig. 3.7 shows the progression of the flow characteristics for four different time steps at approaching Fr number of 0.34 and $h^* = 1$. At the beginning of the recording at time 0.00417 second (1 frame), streaks of streamlines were observed (Fig. 3.7a). After 2 seconds (480 frames), the streamlines appeared to be well developed (Fig. 3.7b). The time-averaged velocity contours for 5 seconds (1200 frames) and 10 seconds (2400 frames) indicate that the streamlines around the submerged deck became visible and did not show any significant difference in the velocity distribution (Fig. 3.7c and 3.7d). Figs. 3.7b to 3.7c also demonstrate the steady nature of the flow. Therefore, for the convenience of the analysis and to reduce the time required to process the images, the analysis in this study was performed for 10 seconds, which is equivalent to 2400 frames.

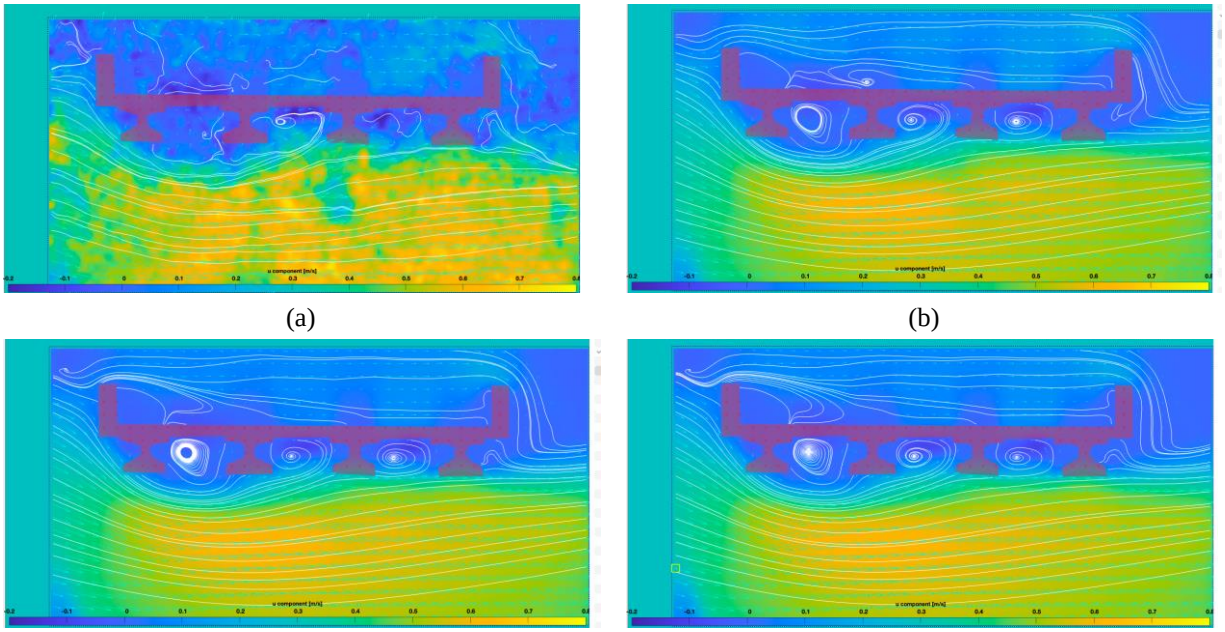

(a) (b)

(c) (d)

Fig. 3.7 Streamline representations of submerged bridge models at time (a) t = 0.004167 s (2 frames), (b) *t* = 2 s (480 frames), (c) *t* = 5 s (1200 frames), and (d) *t* =10 s (2400 frames)

3.3.1.2 Time-averaged Streamwise Velocity Distribution

Different vertical sections along the submerged bridge superstructure were identified to extract the spatial distributions of the streamwise velocity. Fig. 3.8 illustrates the time-averaged velocity field for 10 seconds and *Fr* of 0.34 and verticals where the velocity data were extracted. The velocity data were extracted from upstream and downstream of the bridge, as well as from three sections in the middle of the girder chambers (Fig. 3.8). The locations for extracting streamwise velocity profiles were selected at *x/W* of -0.03, 0.22, 0.47, 0.74, and 1.06, which covered the entire bridge width. Distance *x* was measured from the upstream edge of the railing, and *W* was the width of the bridge deck. The mean streamwise velocity (*v*) profiles were extracted from the PIV images for

different parts of the bridge deck and were normalized by dividing them by the mean approach velocity (V).

The time-averaged velocity distributions plotted in Fig. 3.9 to visualize the flow characteristics show that the distributions of the streamwise velocity along the flow are different in all the sections. The plot of the upstream section in Fig. 3.9a shows that the velocity increased towards the flume bed, which was the result of the downward contraction of flow caused by a reduction in the flow area due to the bridge deck and girders. Figs. 3.9b to 3.9e show a slight decrease in velocity as the y/hu decreased from 1 to 0.92, indicating a reduction in velocity after the flow crossed the top of the bridge deck. There was a reverse flow at section x/W = 0.22 on top of the deck (Fig. 3.9b), indicating that a vortex formed there. A negative velocity was observed for y/h_u = 0.88 – 0.85 at all three girder chambers (Figs. 3.9b to 3.9d), which were just below the bridge deck and between the girders. The negative velocity indicates that the flow was in an upstream (negative) direction and confirms the presence of a vortex between the bridge girder and the shear layer, which is also evident from the flow visualization images in Fig. 3.8. The larger values of the negative velocity and a sharp increase in the positive velocity shown in Fig. 3.9c and 3.9d indicate that the vortices in the second and third chambers were stronger than in the first chamber. Figs. 3.9b to 3.9d also demonstrate that the streamwise velocity increased as the flow passed below the deck when $y/hu < 0.85$ because of the area contraction imposed by the bridge. At the downstream section (x/W = 1.06), low velocity was observed right after the flow crossed the downstream

railing, where the flow reattached with the downstream flow. However, the velocity increased towards the channel bottom, as depicted in Fig. 3.9e.

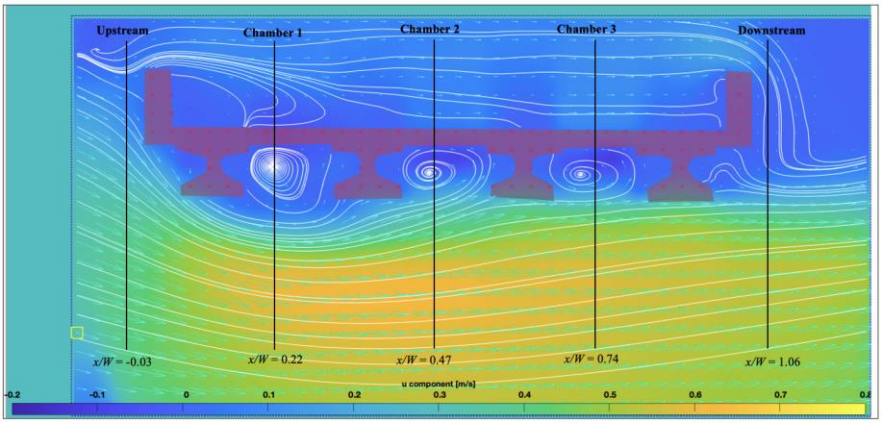

Fig. 3.8 Positions of vertical sections for velocity data extractions

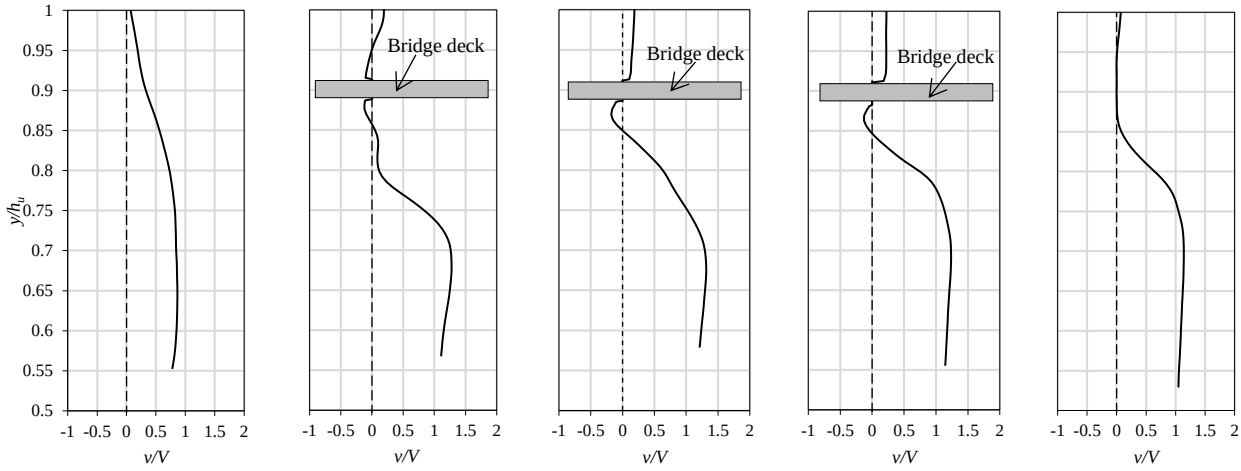

(a) x/W = -0.03 (b) x/W = 0.22 (c) x/W = 0.47 (d) x/W = 0.74 (e) x/W = 1.06

Fig. 3.9 Non-dimensional mean streamwise velocity (*v/V*) profile within the wake region at different non-dimensional streamwise distances (*x/W*): (a) -0.03, (b) 0.22, (c) 0.47, (d) 0.74, and (e) 1.06

3.3.2 Effect of Hydrodynamic Conditions on Flow Field

3.3.2.1 Effects of Froude Number

Figs. 3.10a and 3.10b depict the velocity vectors and streamlines around a submerged I-girder bridge for *Fr* = 0.20 and 0.34, where the shear layer separated and formed a recirculating region

after it crossed, upstream of the railing. The shear layer impinged directly on the second girder for both *Fr* numbers. For *Fr* = 0.3 and 4, the streamlines were higher on the top deck and progressed further downstream than in the flow scenario with *Fr* = 0.20. For *Fr* = 0.34 (Fig. 3.10b), the mean velocities above the bridge deck were larger than those for *Fr* = 0.20 (Fig. 3.10a). This observation is similar to the velocity distribution around a rectangular deck reported by Chu et al. (2016) for two different Froude numbers, i.e., *Fr* = 0.04 and 1.3. Counterclockwise vortices can be seen between the girder chambers for both *Fr* numbers. In the second and third chambers, the streamlines were closer to the bottom of the girders and produced a vortex in the space between the girders. The vorticity (1/s) estimated for the second and third chambers was 15.95 and 20.89, while in the first chamber, the streamlines were further away from the bottom of the girders, resulting in a weak vortex (i.e., vorticity (1/s) = 2.9). As shown in Fig. 3.10a, vortices were also visible downstream of the deck in the lower *Fr* case (= 0.20). Lin et al. (2012) observed similar streamlines and vortex formation for I-girder bridges in the same range of *Fr* number.

Velocity contours in Fig. 3.10a and 3.10b also indicate that the flow velocity increased below the deck after flow separation which, according to the Bernoulli's equation, creates an area of low pressure in the separated region. On the other hand, the velocity reduced resulting in the pressure increasing upstream of the deck at the stagnation point. Therefore, a pressure drag formed, due to the difference in the dynamic pressure upstream of the bridge and the wake region. Moreover, the increased velocity under the deck created an area of lower pressure, and the reduction of velocity over the deck created an area of higher pressure. The difference between the dynamic pressure on the top and below the deck created a suction (negative lift) or lift force below the deck.

Fig. 3.11a and 3.11b show the *FSL* and the critical points of separated mean flow fields on the top and bottom of the deck for flow with an inundation ratio of $h^* = 1$ and *Fr* = 0.20 and 0.34. The

FSL drawn for the top and bottom of the deck of every inundation ratio can be used to identify significant points, such as vertex points (*VP*) and reattachment points (*RP*). It was observed that the flow separation or wake region is wider for Fr = 0.20 than Fr = 0.34, as the blockage effect is more prominent for the lower Fr case. Table 3.3 summarizes the force coefficients and flow kinematic parameters for both Fr numbers. The kinematics parameters were calculated by using Eqn. 3-3 to 3-6. The dimensionless width of the wake region (d^*) was calculated as 0.68 for Fr = 0.20 and 0.60 for Fr = 0.34, which are similar; nevertheless, the vortices on the downstream side of the deck may result in a negative pressure or positive drag to the downstream face of the deck, leading to an increased drag coefficient (C_D) in the lower Fr case. The difference in the flow separation length (R^*) was larger for Fr = 0.34, producing more negative C_L values compared to Fr = 0.20.

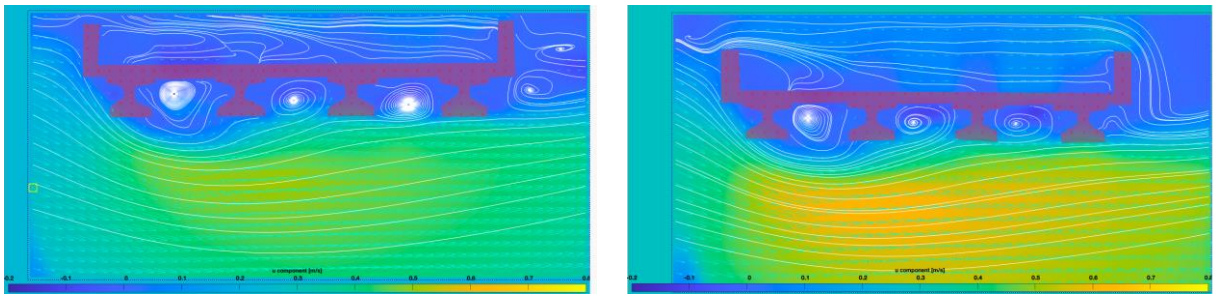

(a) (b)

Fig. 3.10 Time-averaged velocity distribution, streamlines and vortices for h^* of 1 and Froude number: (a) Fr = 0.20 and (b) Fr = 0.34

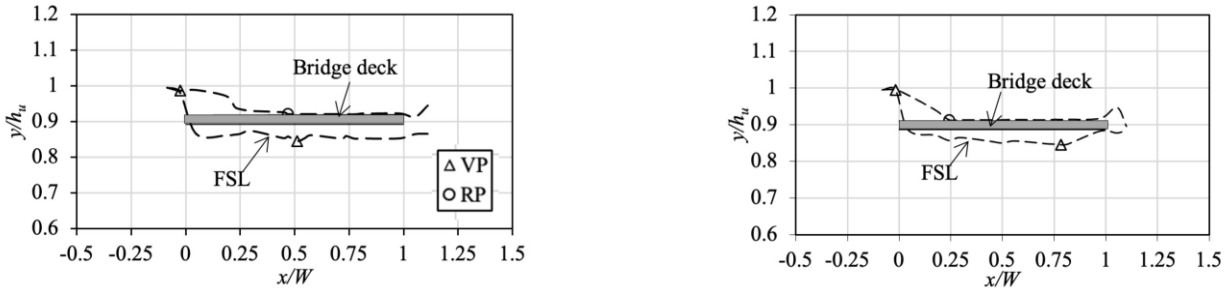

Fig. 3.11 Flow separation lines (FSL) for inundation ratio of h^* = 1 and Froude number of: (a) Fr = 0.20 and (b) Fr = 0.34 (VP = vertex point and RP = reattachment point)

Table 3.3 Hydrodynamic Force Coefficients and Geometric Parameters of Flow Kinematics for Different *Fr* Numbers

Fr	C_D	C_L	d^*	R^*
0.20	0.99	-1.74	0.68	-0.46
0.34	0.88	-2.04	0.60	-0.69

3.3.2.1 Effects of Inundation Ratio

The distributions of flow around the bridge deck for *Fr* = 0.34 and inundation ratios of 0.50, 1.00, and 1.50 are shown in Figs. 3.12 (a-c). The velocity distribution below the deck for all *h** values was similar; however, the presence of vortices in between the girder chambers varied with the *h** value. It was observed that as the bridge submergence increased, the number of vortices below the deck increased. It is also important to note that the flow separation region (Fig. 3.12) varied with the inundation ratio. Malavasi et al. (2007) also presented that the extent of the separation region varies at different submergence levels of a rectangular deck.

Flow separation lines were calculated from time-averaged flow fields at different values of *h** and plotted in Fig 3.13. The *FSL* reattached on the deck upper surface for *h** = 1 and 1.5, while below the deck, it reattached with the flow downstream for all the *h**. The *VP* and *RP* are highlighted for each line in Fig. 3.13. A correlation between flow kinematics and hydrodynamic parameters is shown in Fig. 3.14 by comparing the force coefficients calculated in Chapter 2 with the kinematic quantities determined in this study. At *h** =1, the width of the separation region (*d**) was the smallest and produced the lowest C_D, compared to the *d** values at *h** = 0.5 and 1.5 where the C_D values were higher. This phenomenon indicates that the C_D values increase as the transverse width of the flow separation region increases.

For h^* = 0.5, the flow reattachment distance was calculated by considering only the length of the flow recirculated area on the bottom surface, which resulted the smallest absolute R^* value. It can be seen from Fig. 3.13 that the C_L was the minimum (absolute value) for h^* of 1.0, and the absolute C_L reduced again at h^* of 1.50 and 0.50. For h^* of 0.5, 1.0 and 1.5, the R^* and C_L showed a linear relationship between the flow kinematics and hydrodynamic lift coefficients, indicating that as the difference between the flow circulation region on the top and bottom of the deck increases, the negative lift or suction below the deck increases. These results agree with the observations made by Malavasi and Blois (2007) for a rectangular cylinder.

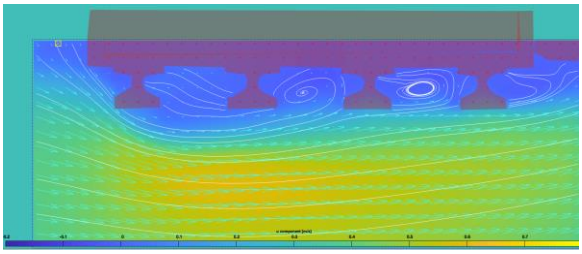

(a)

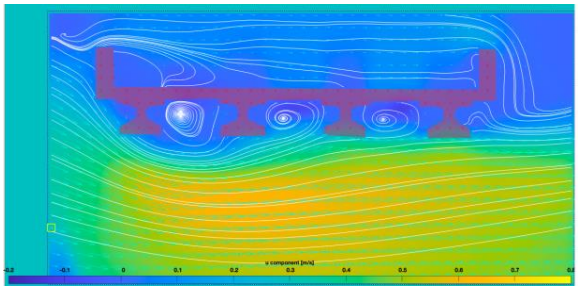

(b)

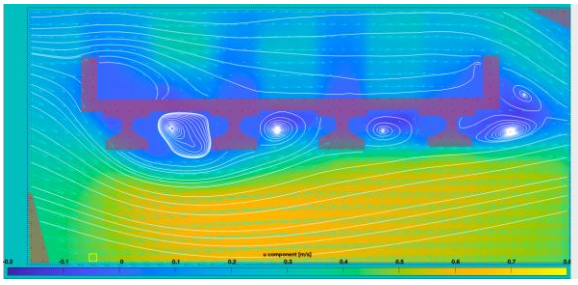

(c)

Fig. 3.12 Velocity contours, streamlines, and vortices for Fr = 0.34 with different inundation ratios: (a) h^*= 0.50, (b) h^*= 1, and (c) h^*= 1.50

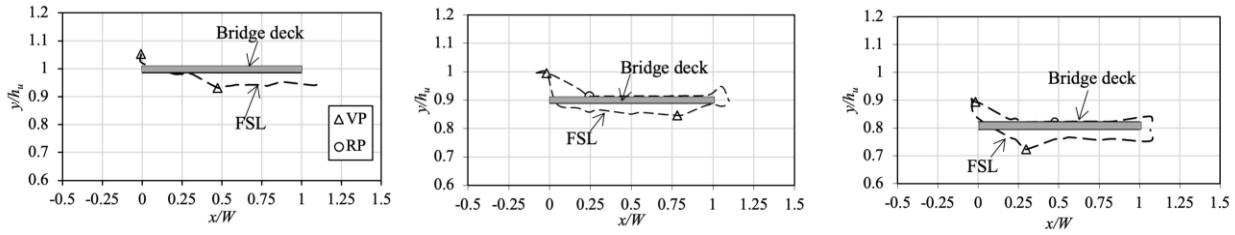

Fig. 3.13 Flow separation line (FSL) at different inundation ratios for top and bottom of the deck: (a) h^* = 0.50, (b) h^* = 1, and (c) h^* = 1.50

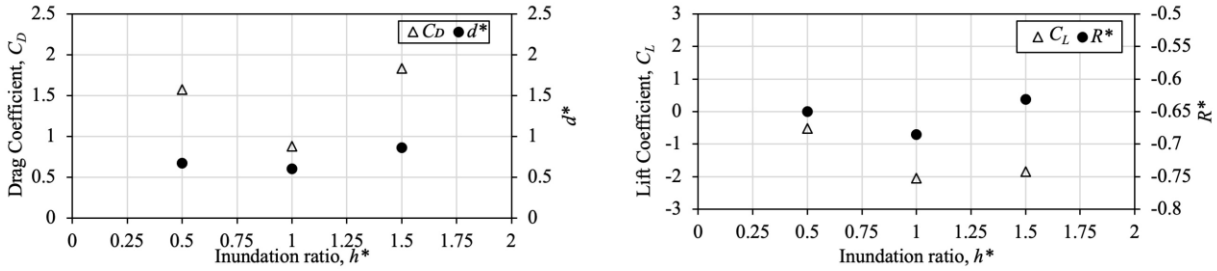

Fig. 3.14 Comparison of the relationships between: (a) dimensionless wake width, d^* and the drag coefficient, C_D with inundation ratio, h^* and (b) dimensionless reattachment length, R^* and lift force coefficient C_L with inundation ratio h^*

3.3.3 Effect of Bridge Geometry on the Mean Flow Field

3.3.3.1 Flow Blockage Ratio

This section presents the flow characteristics around two bridge superstructures of different heights. As a variation in bridge deck height causes different blockages against the incoming flow, it affects flow characteristics (Chu et al. 2016). Fig. 3.15 depicts the streamlines and time-averaged flow velocity contour for blockage ratios (*Br*) of 0.18 and 0.20 at h^* of 1, where it is evident that for the lower blocker ration, vortices formed between the girder chambers; for the higher blockage ratio, they formed below the second girder. Fig. 3.15 also indicates that the reverse flow or recirculating flow was more apparent below the deck than on top of it. This is because the flow below the deck was confined, whereas the flow over the deck was free flowing. In Fig. 3.16, the

FSL plotted for the top and bottom of the deck illustrates the nature of the wake region over the deck's width; *VP* and *RP* are used to calculate the dimensionless parameter of flow structures.

Due to the blockage effect, a wider reverse flow region or wake region (d^*) was observed for a higher blockage ratio (Br = 0.20). This led to increased pressure on the deck and resulted in a greater drag force. It was also discovered that the difference in the length of the flow separation bubble on the top and bottom of the deck was larger for Br = 0.20 than for Br = 0.18, which might be the reason for the slightly higher lift coefficient for Br = 0.20. Table 3.4 summarizes the force coefficients and dimensionless flow kinematic parameters.

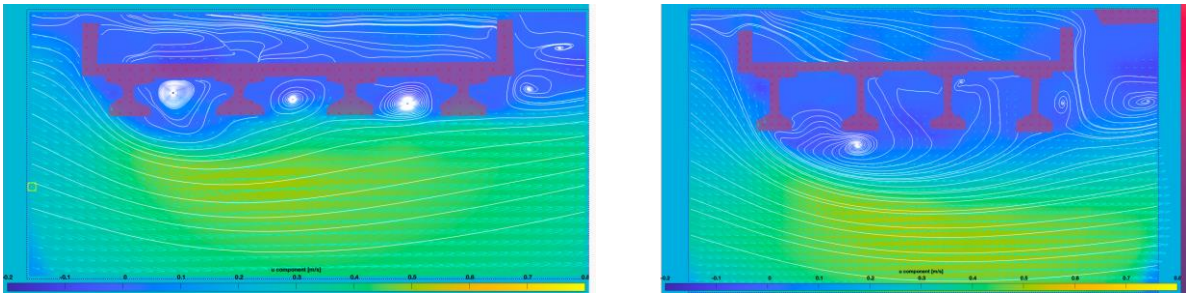

(a) (b)

Fig. 3.15 Velocity contours and streamlines around submerged bridges for Fr = 0.20 with blockage ratios of: (a) Br = 0.18, and (b) Br = 0.20

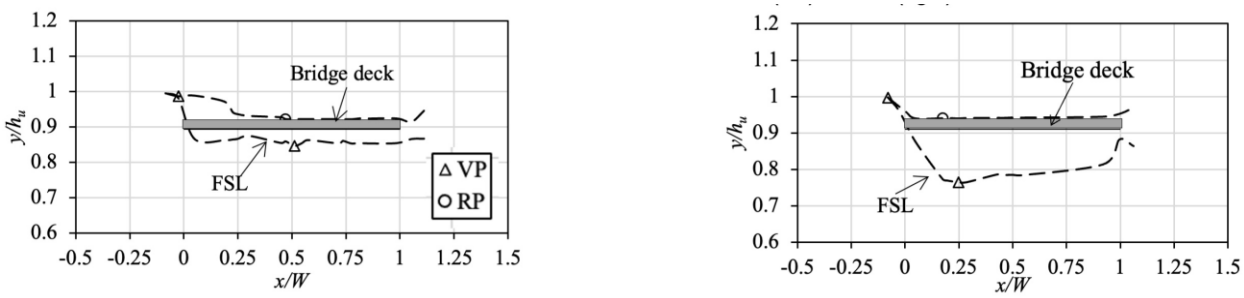

Fig. 3.16 Flow separation line (FSL) for flow blockage ratio of: (a) Br = 0.18 and (b) Br = 0.20

Table 3.4 Hydrodynamic Force Coefficients and Geometric Parameters of Flow Kinematics for Different Blockage Ratios (Br)

Br	C_D	C_L	d^*	R^*
0.18	0.99	-1.74	0.68	-0.46
0.22	1.13	-1.78	0.85	-0.75

3.3.3.2 Aspect Ratio

The streamlines and velocity vectors for aspect ratios of Ar = 4.5 and 7.9 and for h^* of 1 are shown in Figs 3.17a and 3.17b, respectively. In both aspect ratios, the flow separated from the upper corner of the railing and the upstream edge of the deck before reattaching at the top of the deck and downstream of the deck. The flow separation line is drawn both at the top and bottom of the deck in Fig. 3.18 in order to calculate the width of the dimensionless wake (d^*) and the length of the reattachment (R^*). These values are presented in Table 3.5, along with C_D and C_L values for the aspect ratios obtained from Chapter 2. It can be seen from this table that the dimensionless wake width (d^*) remained almost the same as the aspect ratio increased from 4.5 to 7.9, and the C_D increased slightly. The reason for greater C_D at Ar = 7.9 may be attributed to the increased vortex activity for the wider deck, as five vortices developed between the girder chambers (Fig. 3.17b) versus three vortices for the bridge deck with Ar = 4.5 (Fig. 3.17a). An increase in the hydrodynamic load due to the vortex formation between the girder chambers was also reported by Naudascher and Medlarz (1983). The difference between the reattachment length of the top and bottom surfaces of the deck affects the lift coefficient. Table 3.5 reports higher values of R^* and C_L for the narrow deck with an aspect ratio of 4.5. More recirculation activity takes place on top of the wider deck (Ar = 7.9) to reduce the negative lift.

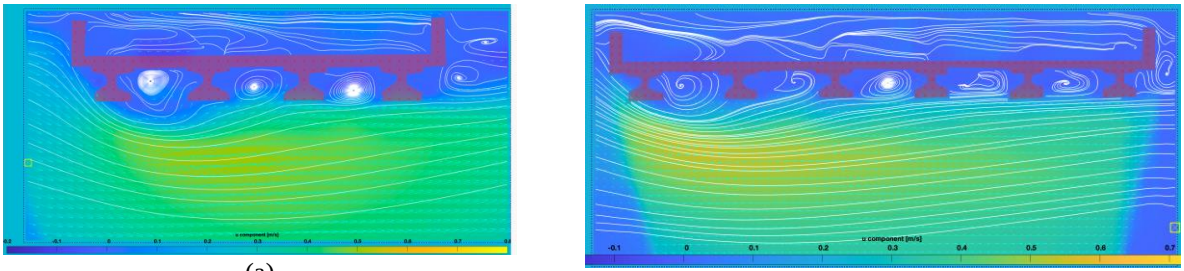

(a) (b)

Fig. 3.17 Velocity contours and streamlines around bridge superstructures for Fr of 0.20 with various aspect ratios: (a) Ar = 4.5, and (b) Ar = 7.9

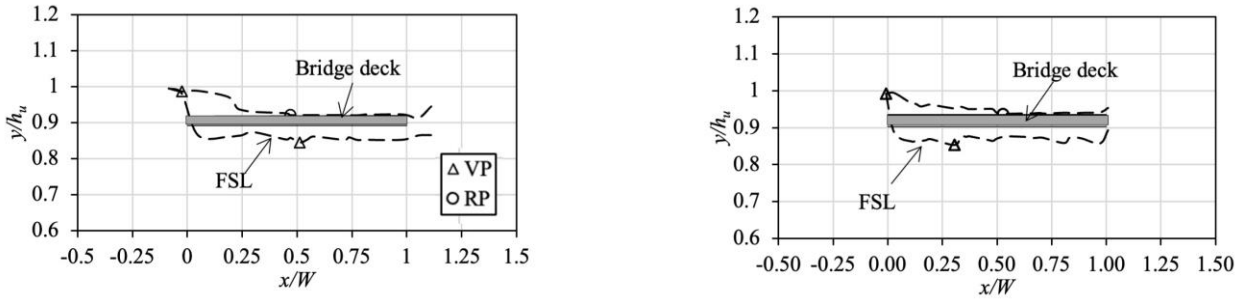

Fig. 3.18 Flow separation line (FSL) for aspect ratio of (a) *Ar* = 4.5 and (b) *Ar* = 7.9

Table 3.5 Hydrodynamic Force Coefficients and Geometric Parameters of Flow Kinematics with Different Aspect Ratios (*Ar*)

Ar	C_D	C_L	d^*	R^*
4.5	0.99	-1.74	0.68	-0.46
7.9	1.05	-1.65	0.60	-0.40

3.3.3.3 Girder Geometry

The effects of girder geometries on the flow field surrounding bridge superstructures are discussed for submerged I-girders and box beams in this section at *h** of 1.00. The flow streamlines and velocity vectors around submerged bridge models are presented in Fig. 3.19a and 3.19b. In addition, these figures show that vortices were generated in between the chambers of the I-girders, whereas only one vortex was evident at the soffit of the box beam immediately following flow separation.

The *FS*L lines were plotted, and the *VP* and *RP* points were marked in Fig. 3.20, based on the velocity profiles (i.e., streamwise velocity) at different vertical sections of the bridge. Based on these lines and points, the dimensionless parameters *d**, and *R** were calculated and reported in Table 3.6, which also presents the hydrodynamic force coefficients calculated in Chapter 2. For the fully submerged condition (*h** = 1), the difference in the C_D values of the I-girder and box

beam was probably due to the differences in the width of the wake regions, which is also supported by the dimensionless wake width parameter (d^*) reported in Table 3.6. The laser sheet could not pass through the top of the deck of the box beam bridge, which made it difficult to estimate the reattachment points. Therefore, the location of the reattachment points for the box beam could not be determined in this study, limiting the comparison of the C_L.

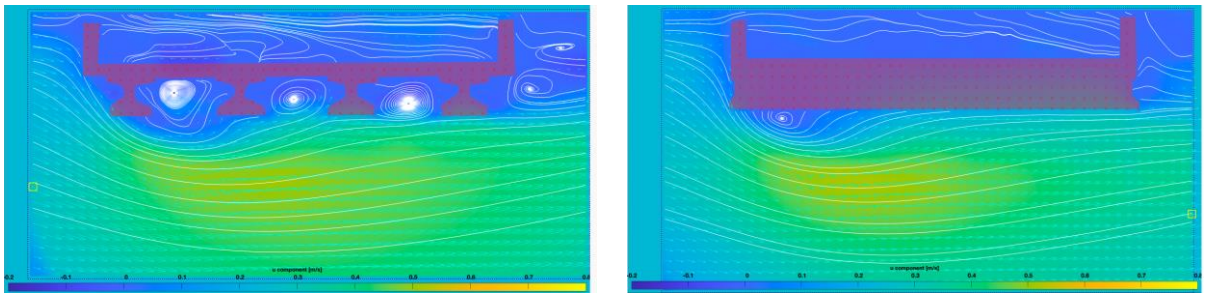

(a) (b)

Fig. 3.19 Velocity contours and streamlines around bridge superstructures for *Fr* of 0.20 with different geometries: (a) I-girders, and (b) box beams

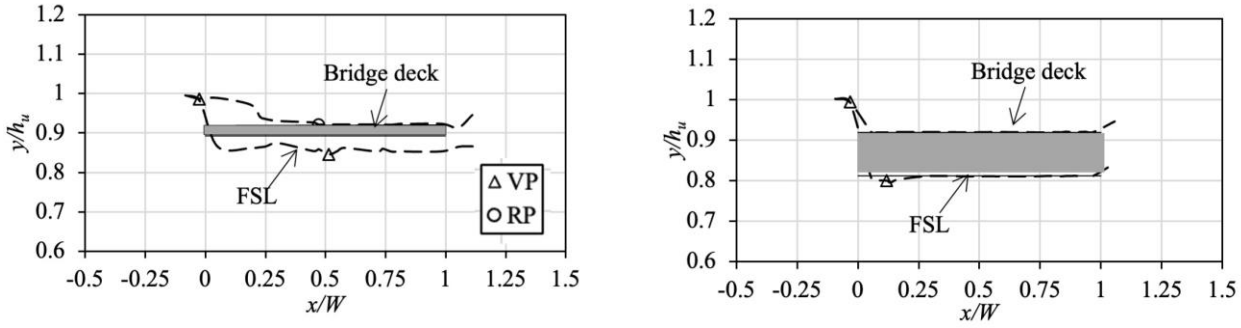

Fig. 3.20 Flow separation lines (FSL) for different bridge geometries: (a) I-girder, and (b) box beam

Table 3.6 Hydrodynamic Force Coefficients and Geometric Parameters of Flow Kinematics for I-girder and Box Beam Bridge Models

Girder type	C_D	C_L	d^*	R^*
I-girder	0.99	-1.74	0.68	-0.46
Box beam	0.70	-1.04	0.55	–†

†The opaque nature of the box beam did not allow the laser light to pass through the beams, so the R^* could not be calculated

3.4 CONCLUSION

A series of experiments was conducted to investigate the mean flow field around a typical stream-crossing bridge under different flow conditions and deck geometries. The flow fields were captured using the time-resolved PIV technique, and flow visualization and the distribution of streamlines at different time intervals were used to assess the stability of the velocity data. A period of 10 seconds or 2400 frames was found to be necessary for the streamlines and vortices to become stable. The flow structure was examined on the basis of estimating feature lines and detecting critical points (i.e., *VP* and *RP*) for typical submerged bridge structures. This study of flow characteristics on bridge models and their relation to hydrodynamic forces led to the following conclusions:

- The mean streamwise velocity profiles were determined at different non-dimensional streamwise distances for Fr = 0.32. The velocity profiles represent stronger vortices in bridge decks with I-girders by indicating a sharper increase in the positive velocity in the second and third chambers than in the first chamber. A weak vortex was observed in between the first and second girder, as a result of the wide wake region near the first chamber. The wake region narrowed in between the second and third chambers, creating a stronger vortex. This phenomenon is also evidenced by the vorticity values.
- Flow characteristics around submerged I-girder bridge models were investigated for Fr of 0.20 and 0.34 of the approaching flow. Although the wake region's dimensions were similar for both Fr numbers, the vortex generated on the downstream side of the deck for the lower Fr (= 0.20) slightly increased the drag force coefficient (C_D). Moreover, the differences in the length of the flow separation on the top and bottom of the deck were higher for Fr = 0.34, resulting in

a larger lift coefficient (C_L). This phenomenon is also evidenced by calculating the dimensionless parameters from flow kinematics and flow visualization images.

- The flow visualization images of all the inundation ratios show separation regions and vortex formations; however, low levels of submersion ($h^* = 0.5$) did not result in the number of vortex formations below the deck and between the girders experienced by high levels of submersion ($h^* = 1$ and 1.5). For $h^* = 1$, the drag coefficient and the width of the wake were minimal. In contrast, the C_D and d^* were higher for h^* of 0.50 and 1.50. As h^* increased, the magnitude of the dimensionless separation length (R^*) also increased for $h^* < 1$; however, the magnitude of downward lift force coefficient (C_L) reduced with the R^* for $h^* > 1$. The higher negative C_L at $h^* = 1$ might be due to the greater vortex generation below the deck, which resulted in significant suction or negative pressure.
- The experimental results in this study indicate that the blockage ratio, aspect ratio, and girder geometry affect the structure of the mean flow field. Variations in the mean flow velocity and flow structures were found to be more significant with a change in the blockage ratio than in the aspect ratio and girder shape. The hydrodynamic force coefficients, C_D and C_L, as well as the dimensionless wake width (d^*) and separation length (R^*), increased as the blockage ratio increased. As the aspect ratio increased, the C_D increased, but the width of the wake (d^*) remained almost unchanged. Vortex activity between the girders contributed to an increase in drag for the wider deck. The C_L and the dimensionless separation length parameter (R^*) decreased with the higher aspect ratio. It was also found that the C_D and d^* were higher for I-girders than for box beams, due to the wider flow separation. However, during the PIV experiments with the box beam, the laser sheet could not pass through the deck, limiting the ability to identify the flow region on top of the deck.

Finally, it can be concluded that hydrodynamic forces are significantly associated with the wake region and vortices that occur within it. This study focused only on the inundation ratios between 0.5 and 1.5, which is the most critical region based on previous research of hydrodynamic forces. Future research could cover a wider range of submergence ratios and develop a relationship between the geometry of the wake region and the hydrodynamic force coefficients for actual bridge superstructures. The experimental data of this study provides valuable information for validation of numerical models. It also demonstrates the applicability of low-cost PIV systems for similar applications in other water resource research studies.

Notations

The following symbols are used in this paper:

A= cross-sectional area of the flow

A_D = wetted area in the direction of flow

A_L = wetted area perpendicular to the flow direction

Ar = aspect ratio

Br = blockage ratio

C_D = drag force coefficient

C_L = lift force coefficient

d^* = normalized wake width

Dw = vertical dimension of the wake region

Dw_b = maximum vertical distance from the bottom face of the deck to the most external point of the flow separation line

Dw_t = maximum vertical distance from the top face of the deck to the most external point (i.e., vertex point) of the flow separation line

Fr = Froude number

F_D = drag force

F_L = lift force

g = gravitational acceleration

h^* = inundation ratio

h_b = distance from the channel bottom to the girder soffit

h_u = upstream water level

L = channel width

Q = flow rate

Re = Reynold number

R^* = dimensionless length of the recirculating flow in the separation region

Rp = difference in horizontal distance between the leading edge and the reattachment point

s = height of the bridge superstructure

V = upstream undisturbed velocity

W = width of the bridge superstructure

X_{rp} = x coordinate of the reattachment points

Xrp_p = x coordinate of the reattachment points at the bottom of the deck

Xrp_t = x coordinate of the reattachment points on the top of the deck

ρ = water density

References

Arslan, T., Malavasi, S., Pettersen, B., & Andersson, H. I. (2013). Turbulent flow around a semi-submerged rectangular cylinder. *Journal of Offshore Mechanics and Arctic Engineering*, *135*(4).

Bruno, L. and Mancini, G., 2002. Importance of deck details in bridge aerodynamics. Structural Engineering International, 12(4), pp.289-294.

Bushra, A., 2010. Computational fluid dynamic analysis of hydrodynamic forces on inundated bridge decks and the effect of scaling. The University of Nebraska-Lincoln.

Carnacina, I., Leonardi, N. and Pagliara, S., 2019. Characteristics of flow structure around cylindrical bridge piers in pressure-flow conditions. Water, 11(11), p.2240.

Gill, S.E.; Handley, J.F.; Ennos, A.R.; Pauleit, S. Adapting cities for climate change: The role of the green infrastructure. Built Environ. 2007, 33, 115–133. [CrossRef]

Hahn, E.M.; Lyn, D.A. Anomalous contraction scour? Vertical-contraction case. *J. Hydraul. Eng.* 2010, 136, 137–141.

Jempson, M., 2000. Flood and debris load on bridges. PhD dissertation, The University of Queensland, Australia.

Laima, S., Li, H., Chen, W. and Ou, J., 2018. Effects of attachments on aerodynamic characteristics and vortex-induced vibration of twin-box girder. *Journal of Fluids and Structures*, 77, pp.115-133.

Lin, C., Kao, M.J., Hsieh, S.C., Lo, L.F. and Raikar, R.V., 2012. On the flow structures under a partially inundated bridge deck. *Journal of Mechanics*, 28(1), pp.191-207.

Liaw, K.F., 2005. Simulation of flow around bluff bodies and bridge deck sections using CFD (Doctoral dissertation, University of Nottingham).

Lyn, D.A. Pressure-Flow Scour: A Reexamination of the HEC-18 Equation. *J. Hydraul. Eng*.

2008, 134, 1015–1020.

Malavasi, S., Franzetti, S. and Blois, G., 2004, June. PIV investigation of flow around submerged river bridge deck. In Proceedings of the International Conference of River Flows, Napoli, Italy (pp. 601-608).

Malavasi, S. and Blois, G., 2007. Influence of the free surface on the flow pattern around a rectangular cylinder. In Ninth International Symposium on Fluid Control, Measurements and Visualization, Tallahassee, FL.

Naudascher, E. and Medlarz, H.J., 1983. Hydrodynamic loading and backwater effect of partially submerged bridges. *Journal of Hydraulic Research*, 21(3), pp.213-232.

NRC. Potential Impacts of Climate Change on U.S. Transportation; National Research Council. Transportation Research Board: Washington, DC, USA, 2008.

Perry, A.E. and Chong, M.S., 1994. Topology of flow patterns in vortex motions and turbulence. *Applied Scientific Research*, *53*(3-4), pp.357-374.

Thielicke, W. and Stamhuis, E., 2014. PIVlab–towards user-friendly, affordable and accurate digital particle image velocimetry in MATLAB. *Journal of Open Research Software*, 2(1).

Yoon, K.S., Lee, S.O. and Hong, S.H., 2019. Time-averaged turbulent velocity flow field through the various bridge contractions during large flooding. Water, 11(1), p.143.

Wright, L.; Chinowsky, P.; Strzepek, K.; Jones, R.; Streeter, R.; Smith, J.B.; Mayotte, J.-M.; Powell, A.; Jantarasami, L.; Perkins, W. Estimated effects of climate change on flood vulnerability of U.S. bridges. Mitig. Adapt. Strat. Glob. Chang. 2012, 17, 939–955.

CHAPTER 4

CONTRIBUTION OF DEBRIS AND SUBSTRUCTURES TO HYDRODYNAMIC FORCE ON BRIDGES

ABSTRACT

The frequency and intensity of recent flood events demonstrate the need for investigating the forces exerted on inundated bridges. The hydrodynamic force coefficients for bridge superstructures are well established in the literature, but they can be significantly affected by the accumulation of debris upstream and the presence of substructures (e.g., piers, bent caps). The aim of this study is to evaluate the effects of debris-damming and substructures on hydrodynamic forces exerted on bridge superstructures. For this purpose, a series of laboratory experiments on small-scale bridge and debris models was performed, and the lift and drag forces and overturning moments on bridge decks with debris and substructures were measured and compared to the hydrodynamic forces generated by flow on superstructures without blockages. The total streamwise and vertical forces and overturning moment were used to investigate the effects of debris and substructures on superstructure forces. Results are also presented on drag, lift, and moment coefficients, as they revealed a considerable change in the hydrodynamic force and moment coefficients because of the additional flow blockages created by debris and substructures. Maximum drag coefficients were observed for a flat plate debris model, combined bridge model (i.e., superstructure, debris, and superstructure), partially submerged model, and a substructure-superstructure model of a fully submerged bridge. Maximum lift and moment coefficients occurred for the substructure and wedge debris models, respectively.

Keywords: Debris, Flood, Hydrodynamic Forces, Bridge Damage, Bridges Substructures

4.1 INTRODUCTION

Bridges are designed to withstand flood and debris loads; however hydraulic events, including floods, scours, debris, etc., cause more than 60% of the bridge failures in the United States (Ahamed 2020, Wardhana and Hadipriono 2003). During high flow events, bridges may become fully or partially submerged, and floodwater exerts significant hydrodynamic forces on them, resulting in shearing and overturning the bridge deck, and even bridge failure. Accurate estimation of flood-induced hydrodynamic loading is crucial for designing safe bridges and evaluating their vulnerability (Turner 2015); however, estimations of the hydrodynamic force on bridge superstructures are usually over-simplified and, in some cases, do not consider the effects of other factors such as debris and substructures (Oudenbroek et al. 2018).

Extensive accumulation of woody debris poses a chronic and severe problem for stream-crossing bridges and is considered one of the leading causes of bridge failures, contributing to approximately one-third of the bridge collapses in the U.S. (Diehl 1997, Benn 2013) and costing millions of dollars (Lassettre and Kondolf 2012). Debris accumulation aggravates flood hazards by increasing the backwater, blocking bridge openings, and forming a temporary reservoir (Lyn et al. 2003, Manners et al. 2007, Steeb et al. 2017, Macchione and Lombardo 2021).

Debris at a bridge section creates an obstruction to the flow that contracts the overall flow area, simultaneously decreasing the upstream flow velocity and increasing the upstream depth and pressure (Parola et al. 2000). Few studies have examined the effect of debris on the hydrodynamic forces of bridge superstructures and substructures. Parola et al. (2000) showed that the accumulation of debris on bridge piers and superstructures can create significant forces that must be considered during the design process to ensure that the structure is appropriately sized. Apelt

(1986) investigated the effect of idealized debris mats on drag forces and reported that the drag coefficient significantly depends on the type of debris and its porosity. Jempson (2000) investigated the impact of debris on five different superstructures and three types of piers and reported that the hydrodynamic force on bridge models with debris depends on the shape and roughness of the debris and the width of the wake or flow separation region created by the debris upstream. Kimura et al. (2017) investigated the flow pressure and water depth of flooding caused by the accumulation of wood at bridges and found that high flows and wood accumulations imply higher flow pressure upstream of the bridge, which increases with the length of the wooden obstruction. Oudenbroek et al. (2018) studied the effect of debris on hydrodynamic forces of bridges and found that debris is a large factor in the failure of bridge decks. The forces associated with the flow on submerged bridges are illustrated in Fig. 4.1 and are briefly discussed in the following.

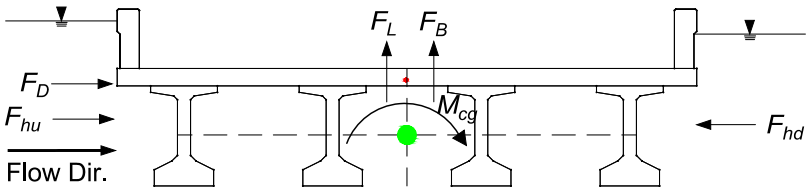

Fig. 4.1 Forces and moment acting on a submerged bridge deck

The variations in the flow depth and pressure created at bridge sections can be explained by considering a model that separates the total streamwise force on a bridge obstruction into two components: a hydrostatic component associated with the streamwise variation of flow depth, and a dynamic component associated with the flow velocity (Parola et al. 2000). According to Koch et al. (1926), the total streamwise force in a channel can be defined by Eqn. 4-1.

$$F_s = F_D + (F_{hu} - F_{hd}) \quad (4\text{-}1)$$

where F_s is the total streamwise force, F_D is the drag force, F_{hu} is the hydrostatic force on the upstream side of the bridge, and F_{hd} is the hydrostatic force on the downstream side of the obstruction.

Drag exerted by debris on a bridge lead to afflux (i.e., a rise of the upstream water level), which generates a difference in the hydrostatic pressure on the upstream and downstream sides of the deck and results in additional loadings. Due to the complexity of determining the hydrostatic force on a porous media such as debris jam, a simplified formula (Eqn. 4-2) is used to model forces on an idealized solid accumulation (Parola et al. 2000). The total force on the structure that is caused by the hydrostatic pressure difference is approximated by Eqn. 4-2.

$$F_h = \rho g(h_{cu}A_{hu} - h_{cd}A_{hd}) \quad (4\text{-}2)$$

where F_h is the horizontal hydrostatic force on the submerged area, h_{cu} is the vertical distance from the upstream water surface to the centroid of area A_{hu}, A_{hu} is the area of the vertically projected submerged portion of the bridge at the upstream section, h_{cd} is the vertical distance from the downstream water surface to the centroid of the area A_{hd}. A_{hd} is the area of the vertically projected submerged portion of the bridge at the downstream section, ρ is the density of water, and g is the gravitational acceleration.

The drag component applied to a bridge superstructure significantly increases as a result of the substantial increase in the obstructed flow area caused by accumulated debris, (Jempson 2000). The magnitude of the drag force is primarily a function of the geometry of the submerged area and the approach velocity and may be calculated using Eqn. 4-3.

$$F_D = \frac{1}{2}\rho C_D A_D V^2 \quad (4\text{-}3)$$

where F_D is the drag force, C_D is the dimensionless coefficient of drag, A_D is the projected area of the submerged object upon which the force is exerted and normal to the flow, and V is the reference velocity or depth-averaged approach flow velocity.

A bridge that is partially or fully submerged by water is subjected to buoyant force (F_B) that acts in an upward direction. F_B is a function of the volume of water displaced by a partially or fully submerged object. In order to calculate the hydrodynamic lift force (F_L), F_B must be removed from the measured vertical force. The hydrodynamic lift force (F_L) on bridges that is due to the dynamic pressure imbalance between top and bottom of the deck can be defined by Eqn. 4-4.

$$F_L = \frac{1}{2}\rho C_L A_L V^2 \quad (4\text{-}4)$$

where C_L is the hydrodynamic lift coefficient and A_L is the reference wetted area of the superstructure projected on a vertical plane normal to the flow.

The eccentricities of the hydrodynamic drag and lift forces with respect to the center of gravity of a bridge superstructure cause an overturning moment. The measured moment needs to be corrected to calculate the moment with respect to the centroid of the bridge superstructures. The centroidal moment with respect to the center of gravity of the superstructure can be calculated using Eqn. 4-5.

$$M_{cg} = \frac{1}{2}\rho C_M L W^2 V^2 \quad (4\text{-}5)$$

where C_M is the overturning moment coefficient, L is the length of the bridge deck, and W is the width of the bridge deck.

The hydrodynamic force and moment coefficients of typical bridge superstructures were reported by the FHWA in 2009; however, the presence of a substructure under a bridge deck poses an important challenge to their determinations, as bridge piers and bent caps can cause obstacles to flood flow by reducing the flow area and inducing local eddy currents and high flow velocities that may damage the bridge structures (Wang et al. 2019). Jempson (2000) reported an increase in the drag coefficients and a decrease in the lift and moment coefficients due to the presence of piers and pier headstocks (bridge elements similar to bent caps). However, the trend of hydrodynamic force coefficients with flow parameters due to the presence of piers and headstock was not consistent for different superstructures models.

The existing literature on hydrodynamic forces on bridge decks is comprehensive but lacks consideration of the effect of debris and substructures on the force coefficients of superstructures. Prior works focused on substructures and superstructures separately (Oudenbroek et al., 2018); this study investigates the interaction between the flood and superstructures when debris and substructures are present. The specific goals of this study are to investigate: (1) the effects of accumulated debris, (2) the effects of substructures (i.e., piers and bent caps), and (3) the effects of substructures and debris on the hydrodynamic force and moment coefficients of superstructures.

4.2 METHODOLOGY

4.2.1 Hydrodynamic Flow Parameters and Force Coefficients

Both the properties of the fluid and the geometric configuration of the bridge are important for determining the structural response of bridge decks, debris, and substructures, (Kerenyi et al., 2009). The hydrodynamic forces on bridge decks are mostly impacted by the flow velocity, depth, and bridge geometry. The flow depth in relation to the girder soffit's position can be expressed as

the inundation ratio (h*). As shown in Fig. 4.2, the inundation ratio measures the depth of the water over the low chord of the bridge girder ($h_u - h_b$) compared to the deck thickness (s). The effect of flow velocity (V) can be expressed by the dimensionless Froude number (Fr). Eq. 4-6 and 4-7 are used to calculate inundation ratio (h*) and Froude number (Fr). All the parameters in these equations are defined in Fig. 4.2.

$$h^* = \frac{h_u - h_b}{s} \tag{4-6}$$

$$Fr = \frac{V}{\sqrt{g h_u}} \tag{4-7}$$

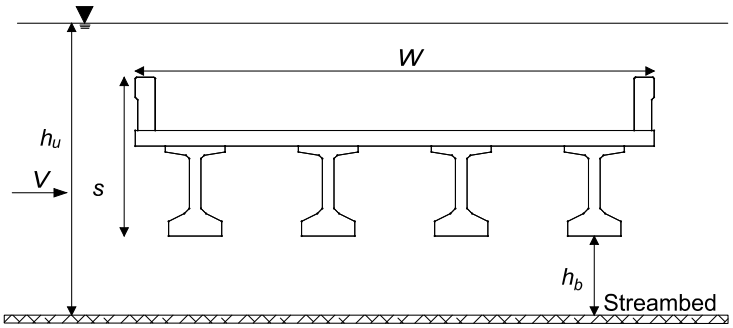

Fig. 4.2 Schematic representation of flow and geometric parameters

A submerged deck is affected by hydrodynamic forces such as drag (F_D) and lift (F_L) as well as overturning moments (M_{cg}), which are usually expressed in terms of nondimensional coefficients. The drag coefficient calculations can vary based on the inundation ratio of the bridge superstructure and can be derived from Eqn. 4-3 and expressed as Eqns. 4-8 and 4-9.

For partially submerged superstructures:

$$C_D = \frac{F_D}{\frac{1}{2}\rho V^2 L(h_u - h_b)} \quad ; \quad h^* < 1 \tag{4-8}$$

For fully submerged superstructures:

$$C_D = \frac{F_D}{\frac{1}{2}\rho V^2 Ls} \quad ; \quad h^* \geq 1 \tag{4-9}$$

The lift coefficient can be derived from Eq. 4-4 and expressed as

$$C_L = \frac{F_L}{\frac{1}{2}\rho V^2 (LW)} \tag{4-10}$$

The moment coefficient with respect to the center of gravity of the bridge deck is defined from Eqn. 4-5 and expressed as

$$C_M = \frac{M_{cg}}{\frac{1}{2}\rho V^2 (LW^2)} \tag{4-11}$$

4.2.2 Experimental Setup

The following experimental setup was designed to investigate the effects of debris and substructures on the forces of bridge superstructures. The experiments were conducted in a 4.90-m long, 0.30-m wide, and 0.45-m deep rectangular plexiglass flume that was set horizontally. A pumping system supplied the flow from an external reservoir and the water depth was controlled by an adjustable tailgate located at the downstream end of the flume. The depth was measured using a point gauge upstream of the bridge and double-checked with a sticky ruler attached to the side of the flume wall. An acoustic doppler velocimeter (ADV) probe was used to measure the point velocity of the flow.

The forces and moments on the bridge deck were measured by a load cell and torque cell system (Fig. 4.3), a three-axis load measurement system that measures force simultaneously in three perpendicular axes: X, Y, and Z. The maximum measurement uncertainty of the load cell is

± 0.15%; the accuracy of measurement for the torque cell is ± 0.02% for a full-scale model. The details of the measurement errors are discussed in Appendix A. The bridge deck model was attached to the measurement system with two vertical support plates, and the entire system was firmly attached to a mounting frame that was designed and constructed for this study and positioned on the flume railing.

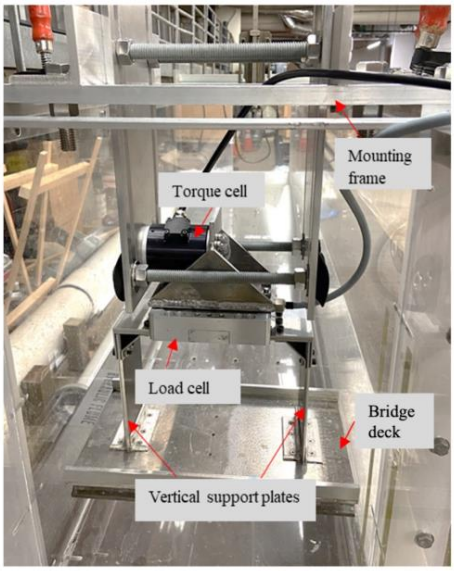

Fig. 4.3 Experimental setup for force and moment measurements on bridge superstructures

The physical modeling of any study requires maintaining geometric, kinematic, and dynamic similarities to ensure that the model replicates the behavior of the prototype when it is subjected to actual flows. This study used a geometric similarity of 1:50, in which the bridge elements were 50 times smaller than their actual sizes but maintained their shapes. The reduction scale of the geometric model was selected based on the flow capacity and flume dimension. The scale models of the bridge elements were made out of aluminum, as its specific weight (27 KN/m^3) is comparable to reinforced concrete (25 KN/m^3). Dynamic similarity requires maintaining the same forces ratio between models and prototypes where a dimensionless Froude number and Reynolds

number ($Re = \frac{\rho VD}{\mu}$) can be used to express the ratios of inertia forces, gravity forces, and viscous forces. Since it is not possible to simultaneously satisfy both the Reynolds number and the Froude number, Froude number scaling is used in laboratory experiments involving open channel flow. The neglect of the Reynolds number similitude is usually justified because *Re* is sufficiently large ($Re > 10^4$) both in the laboratory and in the field, and hydrodynamic force coefficients are relatively insensitive to the *Re* number (Jempson 2000).

4.2.3 Scale Models of Bridge Superstructure, Substructure, and Debris

The following three bridge models or combinations of these models were used in the laboratory experiments.

4.2.3.1 Superstructure Models

The model for the bridge superstructure represents a typical highway bridge deck with six girders and a railing. The 1:50 scale of the model enabled Froude numbers of between 0.20 and 0.32 and an inundation ratio of 0.25 to 1.50 that corresponded to actual flood flows interacting with bridges (Kerenyi et al. 2009). The schematic drawing of the scaled bridge superstructure model of a 46-ft wide deck with six TX54 I-girders and T221 solid guard rail is shown in Fig. 4.4. The details of the bridge elements are presented in Appendix B. Table 4.1 shows the dimensions of the bridge superstructure model and prototype.

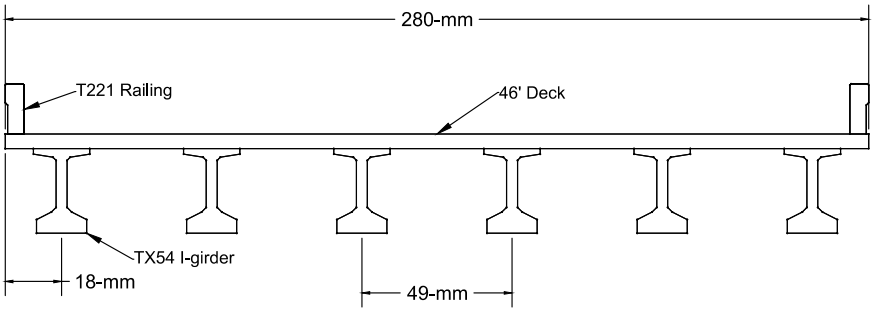

Fig. 4.4 Schematic of the bridge superstructure model

Table 4.1 Dimensions of the Bridge Superstructure Model and Prototype

Attribute	**Actual Dimension (cm)**	**Scaled Dimension (mm)**
Deck thickness	23.83	4.8
Bridge length (*L*)	1511	302
Deck width (W)	1402	280
Girder height	137	27
Railing height	81	16
Superstructure height (s)	218	43

4.2.3.2 Debris Models

One of the most complex aspects of estimating debris force is determining its size and characteristics. The geometry (size and shape), roughness, and permeability of debris against a superstructure or pier can vary widely from flood to flood and river to river (Jempson 2000). Two types of debris are found at bridge sites. The first is flat plate debris, which is smaller debris (grass, brushes, leaves, paper, clothing, etc.) that interlocks with the branches of trees that are wedged against a superstructure or pier, forming a large flat plate against the bridge. Another type of debris is a streamlined wedge that accumulates over time upstream of bridges. The following section discusses these debris models in detail.

Flat Plate Debris

Flat plate debris was modeled with a 3-mm thick steel plate that was rigidly affixed to the upstream side of a bridge deck. Its narrow thickness was intended to minimize the buoyant force while being stiff enough to prevent deformation under the streamwise force. It was 60-mm (3-m) high at 1:50 scale. (3-m is the maximum height of interlocking debris, such as tree limbs against a bridge superstructure, according to Wellwood and Fenwick, 1990) The plate's width matched the 0.3-m width of the bridge deck section to ensure an even channel constriction. The geometry of the flat plate debris is shown in Fig. 4.5.

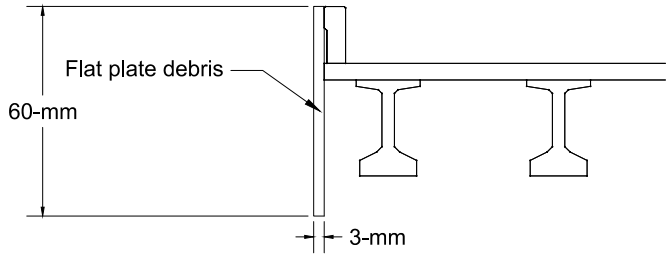

Fig. 4.5 Schematic of flat plate debris attached upstream of the bridge model

Wedge Debris

The wedge debris was made of pinewood dowels that were glued together with wood glue. The 19-mm (95-cm in prototype) diameter dowels represent the width of the trees in the southern forest region, U.S. (Diehl 1997). Smaller-diameter dowels were also added to better fill the cross-section of the wedge. The wedge debris was modeled with a flume-width triangular cross-section whose dimensions were 60-mm high and 178-mm wide at a 1:50 scale (3-m × 9-m in prototype). Positioning the wedge debris in front of the flat plate ensured better surface contact between it and the deck, thereby allowing all the forces generated by the wedge debris to be transferred to the deck. The geometry of the wedge debris is shown in Fig. 4.6.

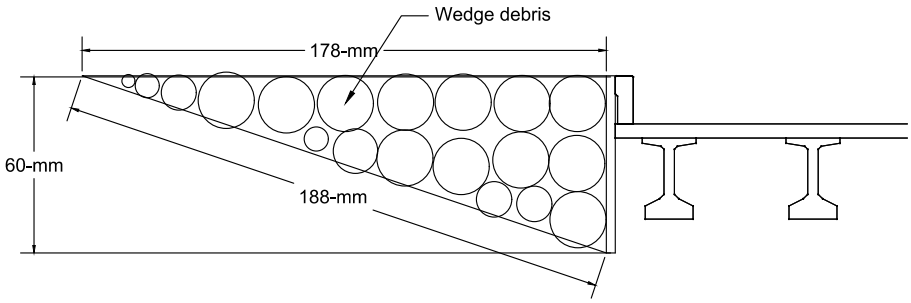

Fig. 4.6 Schematic of the wedge debris attached to the bridge model

4.2.3.3 Substructure Models

Bridge substructures usually consist of bent caps and piers. In this experiment, a standard layout of 3 bents caps and 12 piers was used to demonstrate their effect on the hydrodynamic forces of the bridge superstructure. The schematic of the substructure model is shown in Fig. 4.7. The height of the piers was selected so that the flow parameter could be achieved by using the maximum capacity of the experimental setup. The height and diameter of the pier model were selected as 82-mm and 19-mm, respectively (4.1-m and 95-cm in prototype). The piers were inserted inside the bent caps to hold them together by friction. A false bottom was used to hold the piers together in the flume (Fig. B.10 in Appendix B).

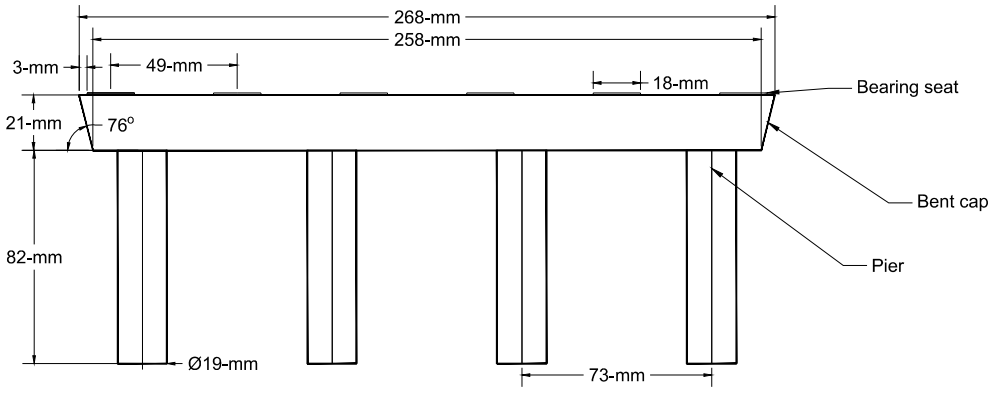

Fig. 4.7 Schematic of bridge substructure (i.e., piers and bent caps)

4.2.4 Experimental Procedure

4.2.4.1 Superstructure Experiments Without Debris

To measure the forces acting on the superstructure, the bridge model was attached to load and torque cells by two support plates and was placed inside the flume. The pumps were activated to provide the flow, and the valves of the flume's inlet pipes were opened until the desired flow rate was reached. Before recording the force data, the readings of the load and moment cells were zeroed, and the water level was kept below the bridge model. The tailgate was then set so that the smallest inundation ratio was reached. Once the model elevation and flow depth were set at the desired test conditions, the force and moment readings were recorded for two minutes. The tailgate was raised in steps, and the flow rate was increased accordingly to test the bridge model for higher inundation ratios and Froude numbers. The same procedure was followed for each inundation ratio between 0.25 to 1.50, at increments of 0.25.

4.2.4.2 Superstructure Experiments with Debris

The flat plate and wedge debris were attached to the upstream side of the bridge superstructure models, which were placed at the desired elevation. The procedure followed for superstructures without debris was replicated, with h^* ranging from 0.25 to 1 and a Fr number of 0.20.

4.2.4.3 Substructures Experiments

Substructure with Superstructure

The bridge superstructure was placed on top of the substructure so that there was a minimal gap between the girder's soffit and the top of the bent cap. This was done to ensure that there was no

resisting force, due to friction between the superstructure and substructure, and to mimic the space needed for the bearing pad in actual bridges. The gap between the superstructure and substructure models allowed the superstructure to move vertically in the direction of the flow while the substructure was affixed to the false bottom of the flume. The procedure that was followed to collect force and moment data for the superstructure experiments was also followed here. The experiments were performed for inundation ratios of 0.25 to 1.50, in increments of 0.25. The *Fr* was not held constant across the full range of h^* because of the insufficient capacity of the flume.

Superstructure, Substructure and Debris Experiments

In this experiment, wedge-shaped debris was attached to the upstream of the bridge deck. Similar to the substructure experiments, a minimum gap was maintained between the superstructures and substructures before recording the force and moment. The experiments were performed for inundation ratios of 0.25 to 1, in increments of 0.25, and a *Fr* number of 0.28.

4.3 RESULTS AND DISCUSSION

4.3.1 Hydrodynamic Force Coefficients of Bridge Superstructure

Experiments were conducted for a bridge deck with I-girders under different inundation ratios (h^*) ranging from 0.25 to 2, Froude number (*Fr*) of 0.20, and h^* = 0.25 to 1.5 for *Fr*= 0.32 (Fig. 4.4). Due to the limitations of the flume and insufficient flow depth during higher Froude number experiments (i.e., *Fr* = 0.32), the test series was limited to a maximum value of h^*=1.50. The hydrodynamic drag, lift, and moment were calculated from the measured streamwise force, vertical force, and overturning moment, respectively. Force and moment coefficients on the bridge deck were calculated using Eqns. 4-8 to 4-11. Details of the procedure used to calculate the force and moment coefficients, C_D, C_L, and $C_{M,}$ are illustrated in Appendix C.

The C_D, C_L, and C_M were plotted against the inundation ratio for Fr = 0.20 and 0.32 (Fig. 4.8), and the plot shows that the C_D decreased until h^* = 1 during partially submerged conditions (Fig. 4.8a). However, the C_D increased for fully submerged conditions (h^* > 1) when the flow separation region or wake region increased and the difference in the dynamic pressure between the upstream and downstream sides of the deck increased. A similar trend was reported by Kerenyi et al. (2009).

Fig. 4.8b displays the variations in the lift coefficient as the inundation increased. The experimental results revealed that C_L was negative for all inundation ratios tested, which means that the flowing water created a pull-down force on the bridge deck. A pull-down or negative lift occurs because of the dynamic pressure imbalance between the top and bottom of the deck (Malavasi et al. 2004). The maximum pull-down or negative lift occurred at h^* = 1 for both Fr = 0.20 and 0.34. At h^* > 1, water flowed over the deck, thus reducing the negative lift on the deck. Similar behavior of the lift coefficient was reported in separate experiments by Malavasi and Guadagnini (2005) and Patil et al. (2009).

The variation of the moment coefficient is shown in Fig. 4.8c. For both Fr values, the C_M was positive when h^* < 1.25, which corresponds to an anticlockwise moment (rotating the downstream side of the bridge up and the upstream side of the bridge down). However, as the inundation ratio increased (h^* > 1.25), a negative moment coefficient or clockwise moment was observed, which means that the bridge would turn over in the clockwise direction during higher inundation ratios. Kerenyi et al. (2009) reported a similar trend for the moment coefficient, though the positive peak at h^* = 1.25 was not present in their results. It should be noted that no significant difference in C_D, C_L, C_M values was observed, except in the critical region of the inundation (0.75 < h^* < 1).

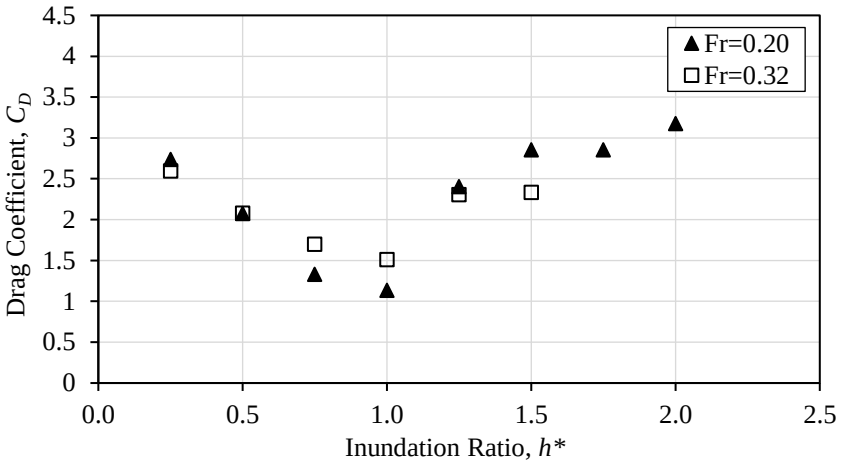

(a)

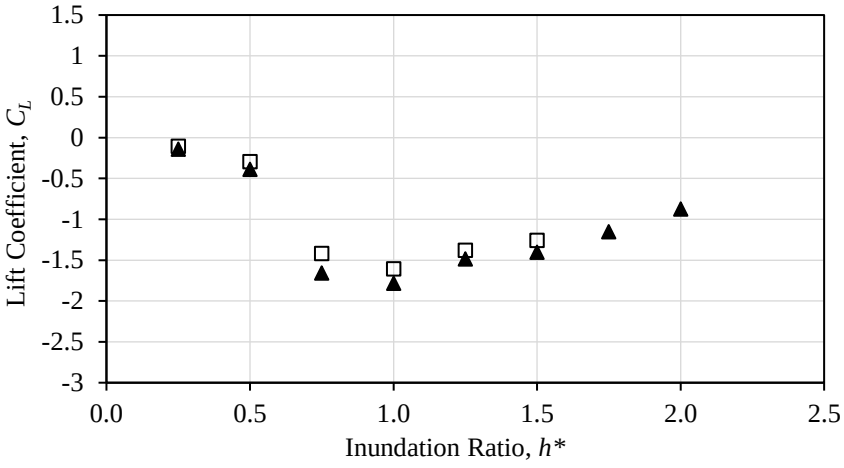

(b)

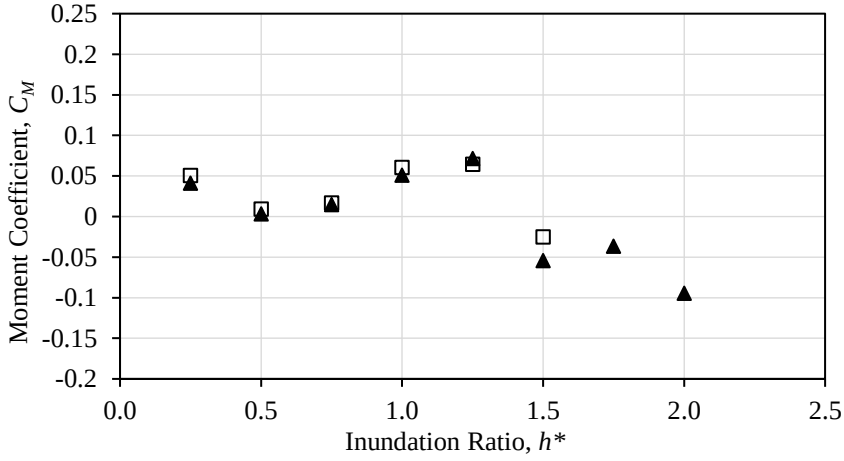

(c)

Fig. 4.8 Hydrodynamic force coefficients vs. inundation ratio for superstructure-only experiments: (a) drag coefficient (C_D), (b) lift coefficient (C_L), and (c) moment coefficient (C_M)

4.3.2 Effect of Debris on Force Coefficients of Bridge Superstructure

Several experiments were conducted to determine how debris affects hydrodynamic force coefficients. The hydrodynamic forces were measured on scale bridge models of two idealized debris mats for a Froude number of 0.20 and inundation ratios (h^*) of 0.25, 0.50, 0.75, and 1. Fig. 4.9 shows the experimental setup for the test series for wedge debris, flat plate debris, and for conditions with the absence of debris.

The force values on the bridge deck were compared to evaluate the effects of debris on bridge superstructures. Figures 4.10 (a-c) show that the horizontal force, which includes drag and hydrostatic forces, vertical force, and overturning moment increased as the inundation ratio increased. The total horizontal force was the highest for the flat plate debris and the lowest for no debris, and the forces for the wedge debris were in between the two, as depicted in Fig. 4.10a. Fig. 4.10b demonstrates that the vertical forces for the wedge debris were significantly higher than the forces for the flat plate debris and for the scenario without debris, and they increased considerably as the inundation ratio increased from 0.5 to 0.75. Fig. 4.10c indicates that the wedge debris produced larger moment values than the bridge models with flat plate debris and without debris.

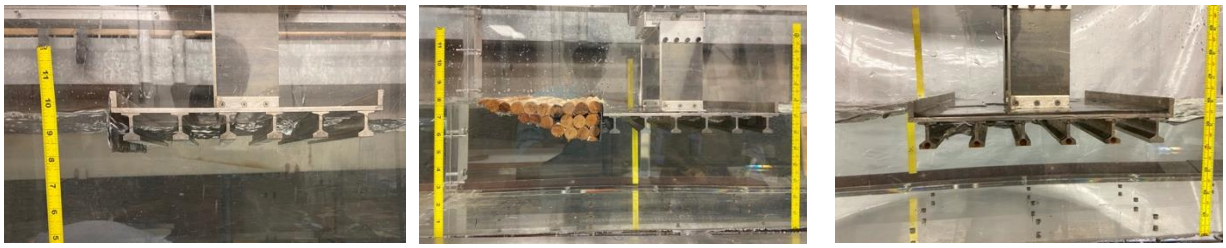

(a) (b) (c)

Fig. 4.9 Experimental setup for the test scenarios with $h^* = 0.75$: (a) flat plate debris, (b) wedge debris, and (c) without debris

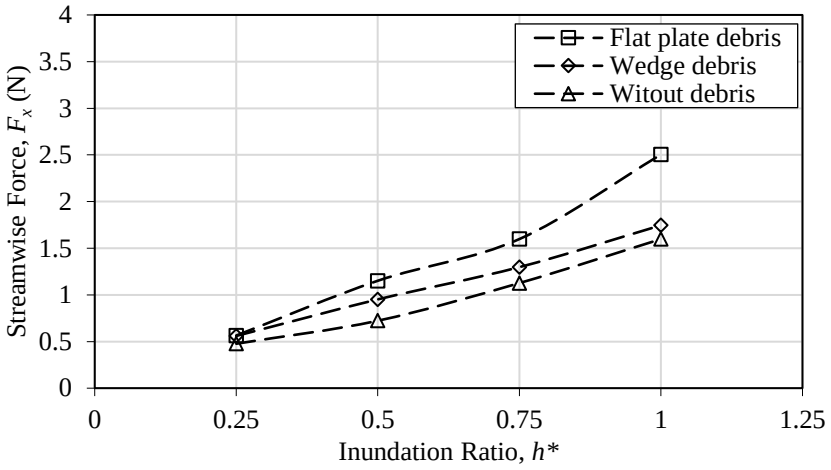

(a)

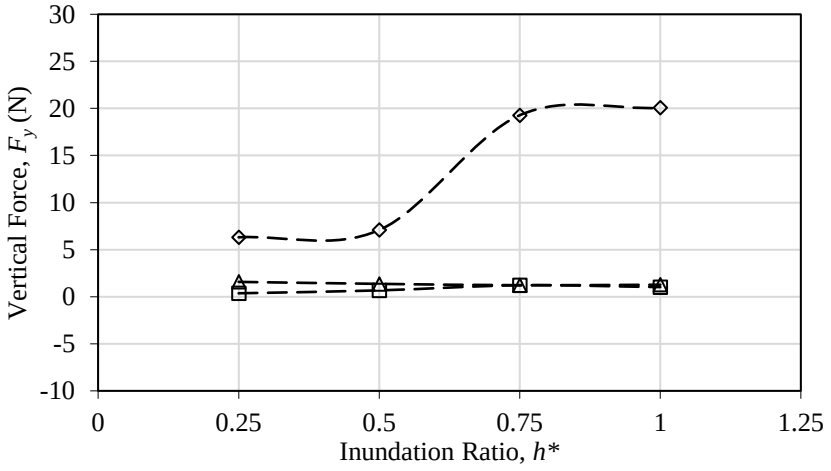

(b)

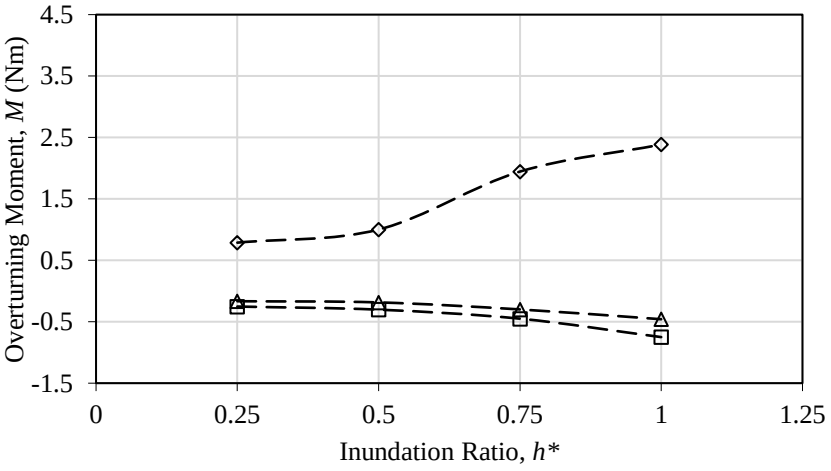

(c)

Fig. 4.10 Force and moment vs. inundation ratio for experiments with and without debris: (a) streamwise force (F_x), (b) vertical force (F_y), and (c) overturning moment (M)

Fig. 4.11 shows the variations of the drag, lift, and moment coefficients with inundation ratio, h^*. The C_D value decreased with h^* (Fig. 4.11a) in both types of debris and for the condition without debris; however, the total streamwise force increased with h^* for the partially submerged deck ($h^* < 1$) with and without debris (Fig. 4.10a). This is because the submerged area increases for partially submerged decks (Eq. 4-8), making the C_D smaller as the level of inundation increases. The results also indicated that the flat plate debris produced the largest horizontal streamwise force (Fig. 4.10a) and had the largest C_D (Fig. 4.11a). There was no significant difference between the C_D values for the wedge debris and the models without debris. Jempson (2000) found that flat plate debris produces more drag, while wedge debris causes smaller drag because of its streamlined shape.

Fig. 4.11b presents the lift coefficient (C_L) variations for the experiments conducted on models with both types of debris and without debris. The C_L values for both types of debris increased (become more negative) as the inundation ratio increased, which can be attributed to the generation of a larger wake region or a decrease in the size of the fluid-structure interaction area. The fluid-structure interaction area was smaller for the flat plate debris and without debris conditions (Fig. 4.9), which created negative pressure and consequently more negative lift. However, the streamlined shape of the wedge debris reduced the size of the wake region and increased the fluid-solid interaction area (Fig. 4.9). Therefore, it can be concluded that the negative lift is smaller in bridge models with wedge debris.

The changes in the moment coefficient (C_M) due to the degree of bridge inundation for the models with and without debris are shown in Fig. 4.11c. The C_M values for the superstructure without debris and for the flat plate did not vary significantly with the inundation ratio; however, it increased (became more negative) with h* for the bridge model with wedge debris. The increase in C_M can be attributed to the change in the location of the line of action of hydrodynamic forces

caused by the addition of the wedge-shaped debris, which produced an additional clockwise moment on the superstructure.

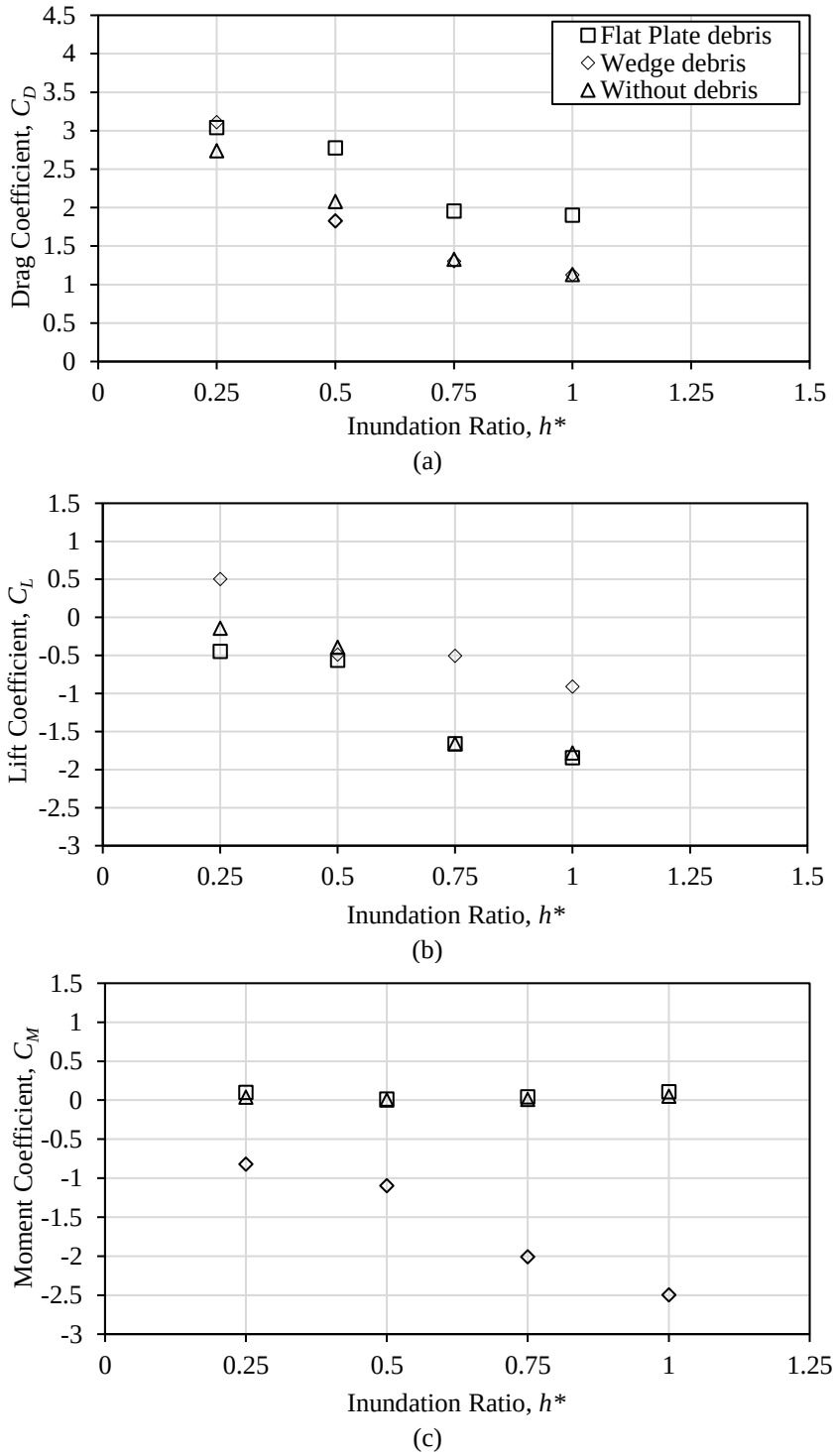

Fig. 4.11 Hydrodynamic force coefficients vs. inundation ratio for experiments on models with and without debris: (a) drag coefficient (C_D), (b) lift coefficient (C_L), and (c) moment coefficient (C_M)

4.3.3 Effect of Substructure on Force Coefficients of Bridge Superstructure Force

The bridge superstructure was tested with piers and bent caps in place to determine its effect on the force coefficients. The bent cap was not attached to the superstructure; therefore, a comparison with the superstructure alone experiment was justified by limiting the transfer of forces from substructures to superstructures. These experiments were performed for h^* = 0.25 - 1.50. The *Fr* number was not held constant across the range of inundation ratio because of the insufficient pump capacity; however, a similar range of *Fr* numbers (0.26 - 0.29) was maintained during both test series. Fig. 4.12 shows the experimental setup of this test series.

Fig. 4.13 displays the total forces and moments measured for the bridge models with and without substructures. As shown in Fig. 4.13a, the horizontal streamwise force increased with the inundation ratio. Moreover, it was observed that the horizontal streamwise force was greater for the substructure-superstructure model compared to the superstructures-only model. The overall vertical force and overturning moment also increased (more-negative values) with an increase in the inundation ratio (Figs. 4.13b and 4.13c). The vertical force and overturning moment were higher in the model with the substructure. It should be noted that as the inundation ratio increased beyond h^* = 1, the horizontal and vertical forces, and overturning moments were significantly different.

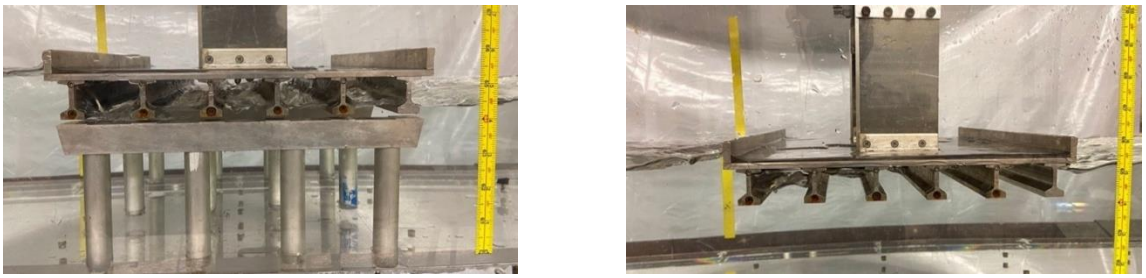

(a) (b)

Fig. 4.12 Experimental setup for the test series with h^* = 0.75: (a) with substructure and (b) without substructure

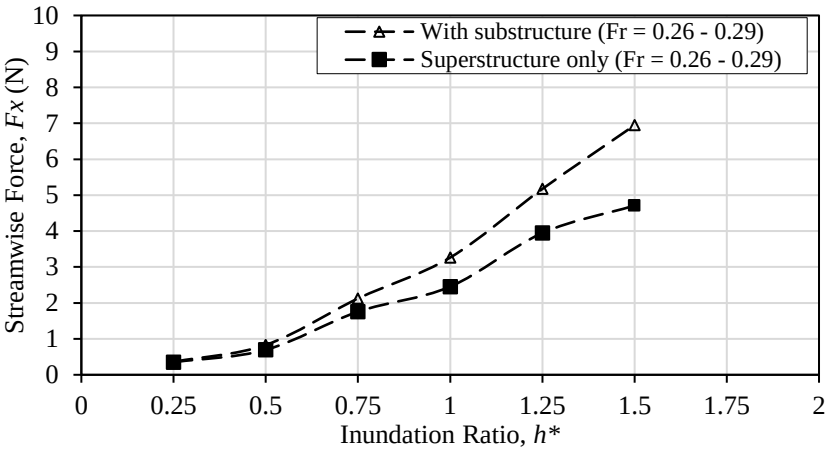

(a)

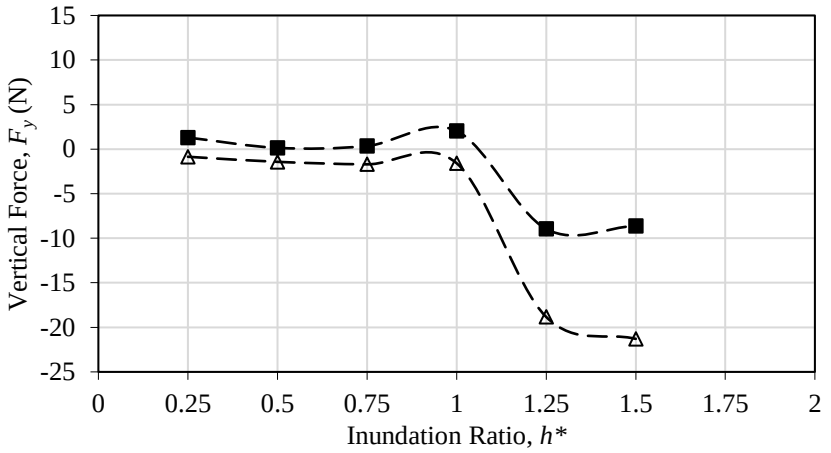

(b)

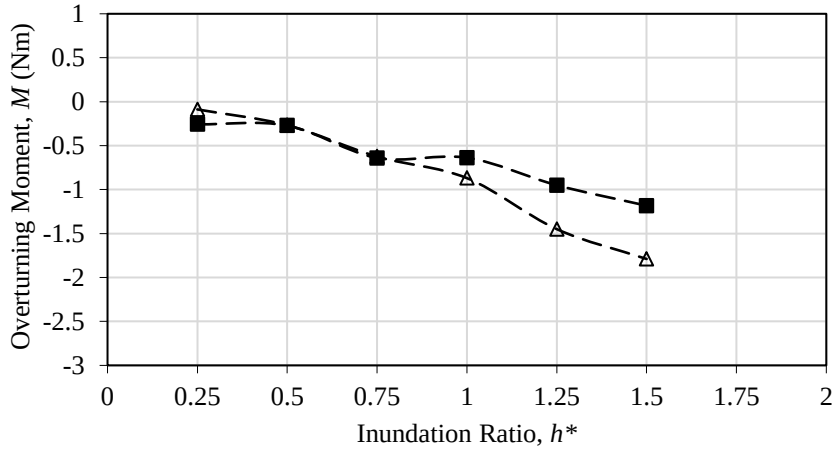

(c)

Fig. 4.13 Force and moment vs. inundation ratio for bridge superstructures with or without substructures: (a) streamwise force (F_x), (b) vertical force (F_y), and (c) overturning moment (M)

Fig. 4.14 illustrates the variations of the drag, lift, and moment coefficients with various inundation ratios. The plots of the drag coefficients show an increasing trend, with C_D being larger for the fully submerged substructure-superstructure ($h^* > 1$) (Fig. 4.14a). The C_D values were similar for both models when they were partially submerged ($h^* <1$). Although the wake region was larger for the bridge superstructure model with a substructure when $h^* < 1$, the C_D values did not increase accordingly because of the higher contribution from the hydrostatic forces to the total streamwise force.

Fig. 4.14b illustrates the lift coefficient values for different inundation ratios of bridge models with and without a substructure and shows that no significant difference was observed between the C_L values, except for the fully submerged models ($h^* > 1$). The presence of piers and bent caps, as indicated in Fig. 4.12a, generated a larger difference between the water depths upstream and downstream of the deck at all inundation ratios. The difference in water depth indicates a region of low pressure after flow separation and subsequently a higher dynamic pressure imbalance between the top and bottom of the deck, leading to a more negative C_L. Generally, the presence of piers made the C_L more negative, which is consistent with the results obtained by Jempson (2000).

Fig. 4.14c plots the overturning moment coefficients (C_M) against the inundation ratio and compares the C_M values for with- or without-superstructure conditions. It can be seen that the presence of a substructure did not cause a consistent shift in the C_M values, but the scattered nature of the C_M data made it difficult to definitively establish the influence of the substructure on the moment coefficients.

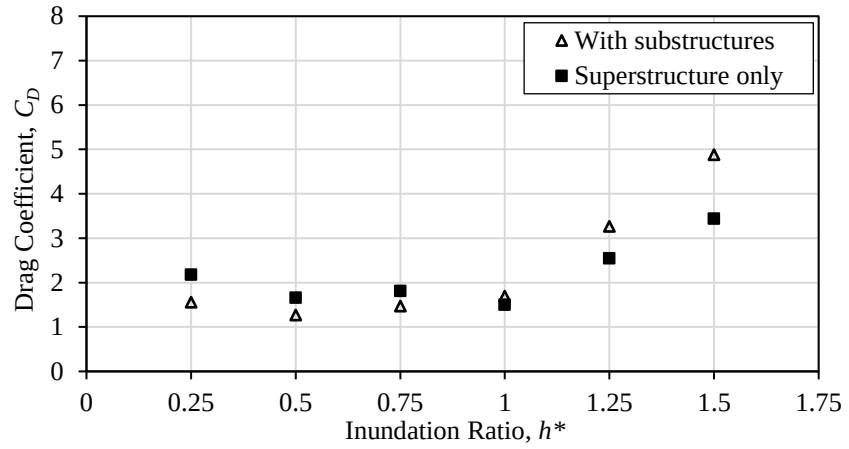

(a)

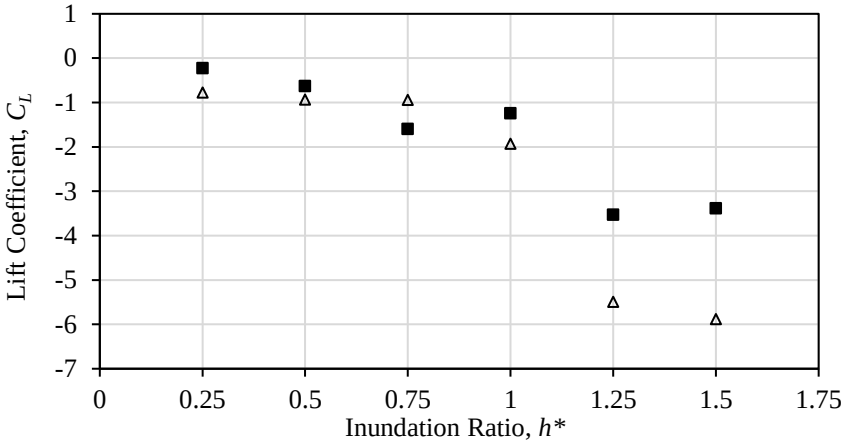

(b)

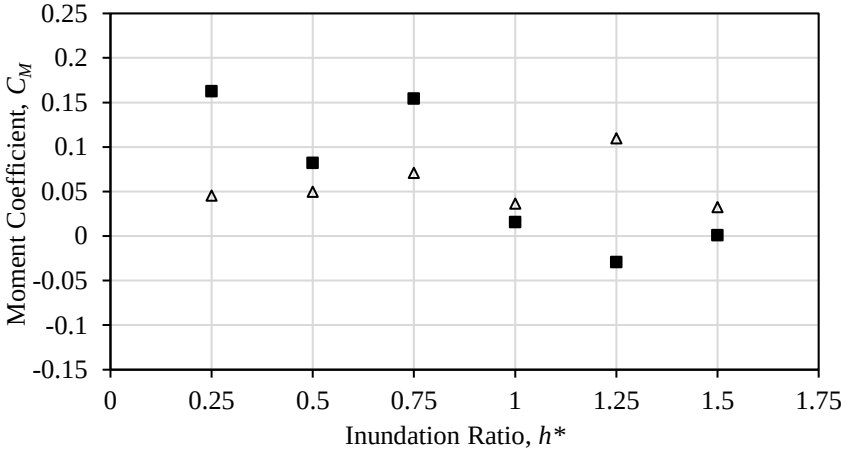

(c)

Fig. 4.14 Hydrodynamic force and moment coefficients vs. inundation ratio for experiments on bridge models with and without substructures: (a) drag coefficient (C_D), (b) lift coefficient (C_L), and (c) moment coefficient (C_M)

4.3.4 Combined Effects of Substructure and Debris on Force Coefficients of Superstructure

The bridge superstructure model was tested with the substructure placed underneath and the wedge debris positioned upstream of the deck. The experiments were conducted with inundation ratios from 0.25 to 1 and an Fr = 0.28. The flow capacity of the flume did not allow experiments to be performed with Fr higher than 0.28; therefore, the results of these tests were compared with the forces and force coefficients for the superstructure-only experiments with Fr = 0.32. For these tests, the piers were not connected to the superstructure; thus, the comparison with the superstructure results is valid. Fig. 4.15 compares the experimental setup of the superstructure-debris-substructure (SDS) and superstructure-only (SO) bridge models.

Fig. 4.16 shows the combined effects of debris and substructures on the streamwise force, vertical force, and overturning moment and compares them with the forces and moment on a superstructure bridge model without a substructure. Higher magnitude of streamwise forces were observed in the SDS experiments than in the SO experiments (Fig. 4.16a), but the streamwise forces increased in both experiments with an increase in the inundation ratio. The total vertical force was positive (upward) in the SDS experiment but decreased as the h^* increased. The force was positive in the SO experiment for $h^* < 0.5$; it became zero at $h^* = 0.5$ and negative (downward) for higher inundation ratios (Fig. 4.16b). The variation of the overturning moment for the SDS and SO bridge models is depicted in Fig. 4.16c. The SDS and SO models resulted in the same magnitude of overturning moment when $h^* \leq 0.5$ but showed opposite directions. The moment of the SDS model was in a clockwise direction and the moment of the SO model was in a counterclockwise direction.

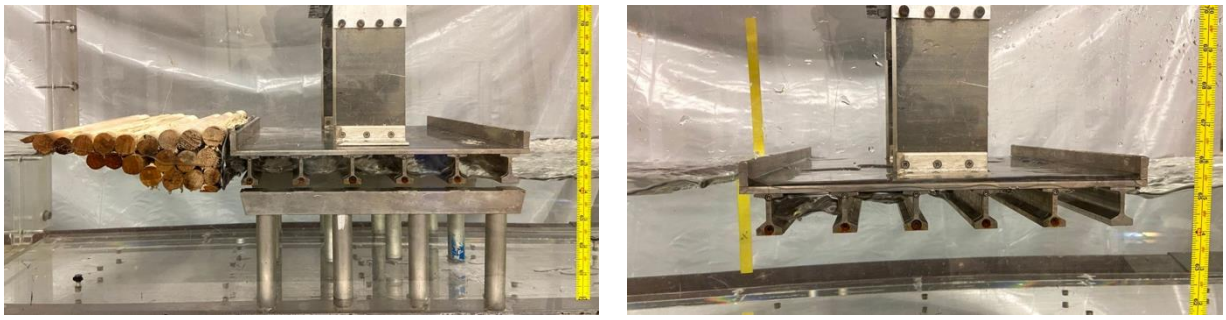

(a) (b)

Fig. 4.15 Experimental setup for test series: (a) substructure-debris-superstructure (SDS) and (b) superstructure-only (SO)

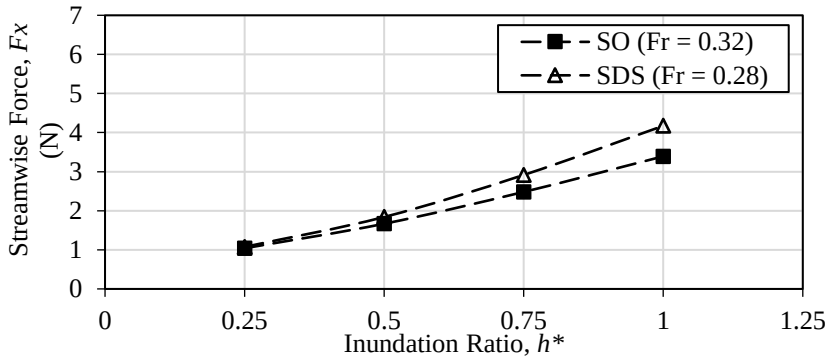

(a)

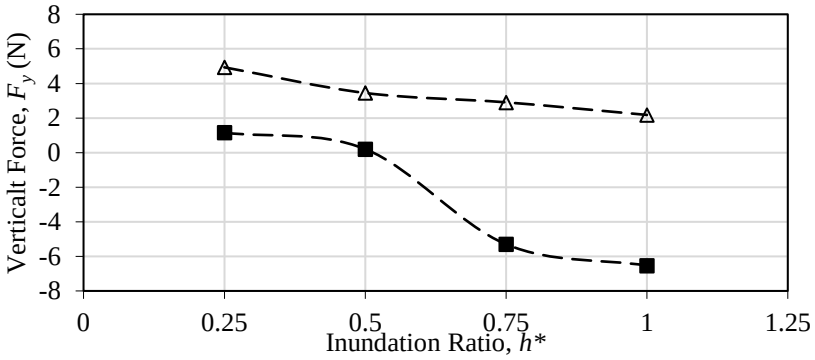

(b)

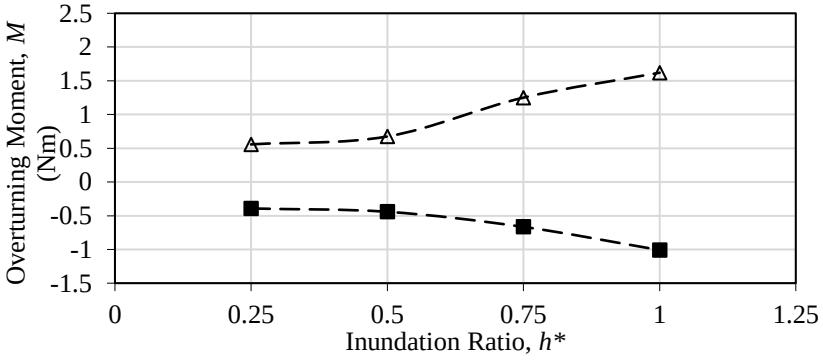

(c)

Fig. 4.16 Force and moment variations for superstructure-only (SO) and superstructure-debris-substructure (SDS) models: (a) streamwise force (F_x), (b) vertical force (Fy), and (c) overturning moment (M)

The variances of C_D, C_L, and C_M with the inundation ratio (h^*) are shown in Fig. 4.17. The C_D for the substructure-debris-superstructure (S*DS*) model was greater than the superstructure-only (SO) model for all the inundation ratios (Fig. 4.17a). As previously explained, the presence of wedge debris increases the size of the fluid-structure interaction area and reduces the wake region and the drag force on the deck. However, piers and bent caps add to the flow blockage, reducing the fluid-structure interaction area, making it smaller than that of the superstructure without a substructure (Fig. 4.15a). Due to this combined effect, the overall values of C_D for were higher for the SDS test than for the SO experiment at all inundation ratios; however, the difference between the C_D values of the two models decreased with an increase in h^*.

Fig. 4.17b shows that the C_L for both models varied with h^* and the decreasing trend was consistent for the SO and SDS models. The h^* of both models increased as the C_L became more negative, but the C_L of the SDS model was more negative than that of the SO model. Nonetheless, the difference between the C_L values of the two models was more pronounced when $h^* \geq 0.75$, as the SDS model created a larger difference in the dynamic pressure at the top and bottom of the deck due to additional blockage caused by the presence of a pier below the deck. Jempson (2000) also reported that the presence of piers and bent caps results in a more negative C_L.

The C_M for the SDS model was negative (clockwise) for all the inundation ratios, primarily due to presence of the wedge debris, while it was positive (counterclockwise) for SO model (Fig. 4.17c). The minimum value of the C_M was observed at $h^* = 0.50$ for both models. In both experiments, the absolute values of C_M were higher for $h^* < 0.50$.

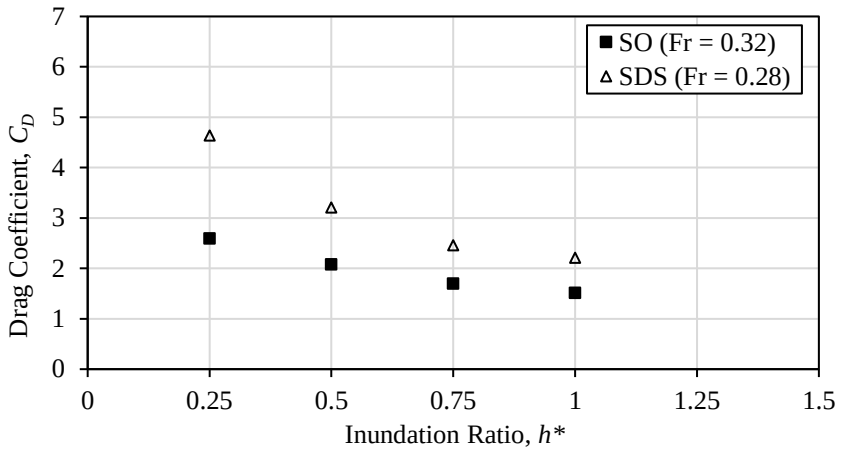

(a)

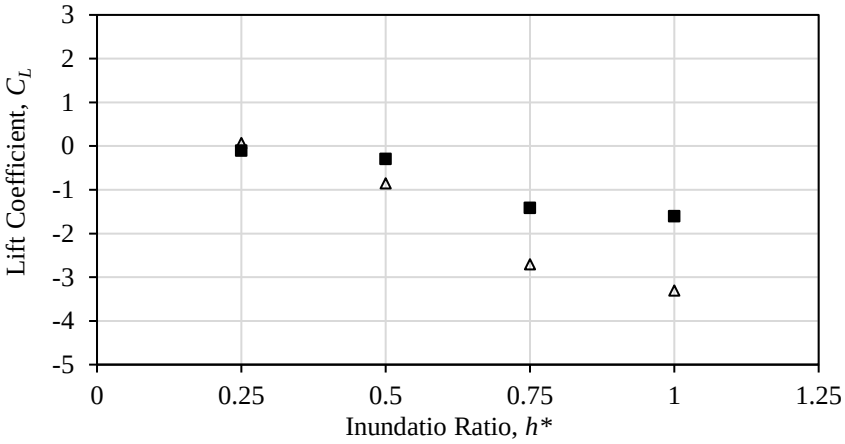

(b)

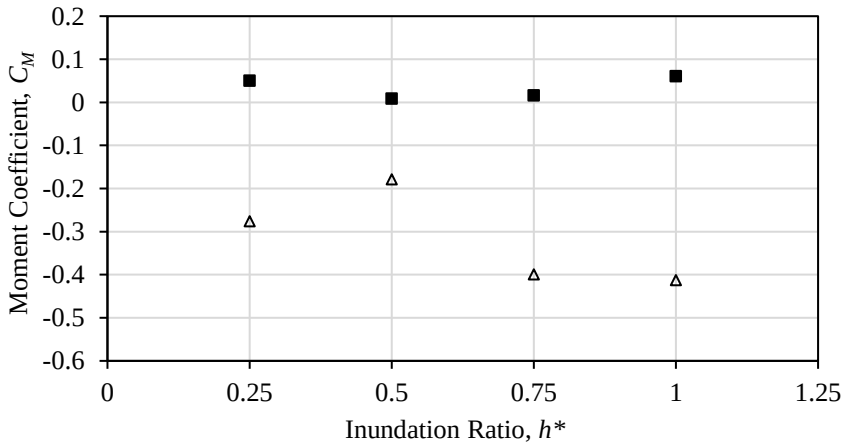

(c)

Fig. 4.17 Hydrodynamic force coefficients vs. inundation ratio for superstructure-only (SO) and superstructure-debris-substructure (SDS) models: (a) drag coefficient (C_D), (b) lift coefficient (C_L), and (c) moment coefficient (C_M)

4.4 CONCLUSIONS

A series of laboratory experiments was conducted to investigate the effect of debris and substructures on the hydrodynamic forces on bridge superstructures. Experiments were conducted for two types of debris, flat plate and wedge, and substructures (piers and bent caps). Load and torque cells were employed to measure the total streamwise force, vertical force, and overturning moment. The drag, lift, and moment coefficients were calculated for each bridge model and the results revealed that debris and substructures significantly affect the forces and moments exerted on bridge superstructures. The magnitudes and coefficients of hydrodynamic forces and overturing moments were calculated for superstructures with and without debris or substructures, and the following conclusions were drawn:

- The presence of flat plate debris increased the C_D significantly, while the wedge debris reduced the negative lift coefficient. The C_M of the flat plate debris did not vary much from the C_M of the superstructure-only bridge model; however, the wedge debris significantly increased the CM (clockwise moment). The clockwise moments in the wedge debris experiments can be attributed to the change to the location of the line of action of lift force towards the upstream side of the bridge.
- Substructures (i.e., piers and bent caps) increased the C_D values and decreased the C_L for fully submerged conditions, but no specific pattern was observed in the C_M . The effects of substructures on the C_D and C_L were attributed to a reduction in the size of the fluid-structure interaction area that was caused by a blockage in the flow created by the presence of the piers and bent caps.
- The combined effects of the debris and substructures increased the C_D and decreased the C_L and C_M. The variations in the C_D and C_L can be attributed to the greater wake region

below the deck due to the presence of the substructure. Moreover, the superstructure-debris-substructure model generated greater (more negative) C_M compared to the superstructure-only model. The increase in C_M can be attributed to a shift in the location of the line of action of forces to the more upstream side, due to the addition of wedge debris.

In summary, the experiments conducted on the debris and substructures demonstrated that using design coefficients estimated based on the bridge superstructure-only may underestimate forces exerted by flood on bridges, especially where a blockage is created by debris and substructures. For these cases, the results presented in this paper will be useful to bridge designers, but further work is needed to generalize the results for a greater range of bridge deck and debris geometry.

Acknowledgments: The authors are grateful to the Texas Department of Transportation (TxDOT) for providing the necessary information about bridge design and for funding this project.

Notations

The following symbols are used in this paper:

A_D = projected area of the submerged object upon which the force is exerted and normal to the flow

A_L = reference wetted area of the superstructure projected on a vertical plane normal to the flow

A_{hd} = area of the vertically projected submerged portion of the bridge at the downstream section

A_{hu} = area of the vertically projected submerged portion of the bridge at the upstream section

C_D = dimensionless coefficient of drag

C_L = hydrodynamic lift coefficient

C_M = hydrodynamic moment coefficient

F_B = buoyant force

F_D = drag force

F_h = horizontal hydrostatic force on the submerged area

F_s = total streamwise force

Fr = Froude number

F_{hd} = hydrostatic force on the downstream side of the bridge

F_{hu} = hydrostatic force on the upstream side of the bridge

g = gravitational acceleration

h^* = inundation ratio

h_b = depth of the girder soffit from the flume bed

h_u = water depth upstream

h_{cd} = vertical distance from the downstream water surface to the centroid of the area

h_{cu} = vertical distance from the upstream water surface to the centroid of area

M_{cg} = centroidal moment with respect to the center of gravity of the superstructure

Re = Reynolds number

V = reference velocity or depth-averaged approach flow velocity

ρ = density of water

Reference

Ahamed, T., Duan, J.G. and Jo, H. 2020. Flood-fragility analysis of instream bridges–consideration of flow hydraulics, geotechnical uncertainties, and variable scour depth. Structure and Infrastructure Engineering, pp.1-14.

Benn, J., 2013. Railway bridge failure during flooding in the UK and Ireland. Proceedings of the Institution of Civil Engineers-Forensic Engineering, 166(4), pp.163-170.

Bricker, J.D. and Nakayama, A., 2014. Contribution of trapped air, deck superelevation, and nearby structures to bridge deck failure during a tsunami. *Journal of Hydraulic Engineering*, 140(5), p.05014002.

Diehl, T.H., 1997. Potential drift accumulation at bridges. McLean, VA, USA: US Department of Transportation, Federal Highway Administration, Research and Development, Turner-Fairbank Highway Research Center.

De Cicco, P. N., Paris, E., Ruiz-Villanueva, V., Solari, L., & Stoffel, M. (2018). In-channel wood-related hazards at bridges: A review. *River Research and Applications*, *34*(7), 617-628.

Jempson, M., 2000. Flood and debris loads on bridges.

Koch, A. and Hainz, L., 1926. Von der Bewegung des Wassers und den dabei auftretenden Kräften: Grundlagen zu einer praktischen Hydrodynamik für Bauingenieure, nach Arbeiten von... Alexander Koch.. J. Springer.

Kerenyi, K., Sofu, T. and Guo, J., 2009. Hydrodynamic forces on inundated bridge decks (No. FHWA-HRT-09-028). Turner-Fairbank Highway Research Center.

Manners, R.B., Doyle, M. and Small, M.J., 2007. Structure and hydraulics of natural woody debris jams. Water Resources Research, 43(6).

Macchione, F. and Lombardo, M., 2021. Roughness-based method for simulating hydraulic consequences of both woody debris clogging and breakage at bridges in basin-scale flood modeling. Water Resources Research, 57(12), p.e2021WR030485.

Lassettre, N.S. and Kondolf, G.M., 2012. Large woody debris in urban stream channels: redefining the problem. River Research and Applications, 28(9), pp.1477-1487.

Lyn, D. A., Cooper, T. J., Yi, Y. K., Sinha, R. N., & Rao, A. R. (2003). Debris accumulation at bridge crossings: laboratory and field studies.

Panici, D., Kripakaran, P., Djordjević, S., & Dentith, K. (2020). A practical method to assess risks from large wood debris accumulations at bridge piers. *Science of The Total Environment*, *728*, 138575.

Parola, A.C., Apelt, C.J. and Jempson, M.A., 2000. *Debris forces on highway bridges* (No. 445). Transportation Research Board.

Steeb, N., Rickenmann, D., Badoux, A., Rickli, C. and Waldner, P., 2017. Large wood recruitment processes and transported volumes in Swiss mountain streams during the extreme flood of August 2005. Geomorphology, 279, pp.112-127.

Turner, D., 2015. Fragility assessment of bridge superstructures under hydrodynamic forces (Doctoral dissertation, Colorado State University).

Oudenbroek, K., Naderi, N., Bricker, J.D., Yang, Y., Van der Veen, C., Uijttewaal, W., Moriguchi, S. and Jonkman, S.N., 2018. Hydrodynamic and debris-damming failure of bridge decks and piers in steady flow. Geosciences, 8(11), p.409.

Wang, W., Zhou, K., Jing, H., Zuo, J., Li, P. and Li, Z., 2019. Effects of bridge piers on flood hazards: a case study on the Jialing River in China. Water, 11(6), p.1181.

Wardhana, K. and Hadipriono, F.C. 2003. Analysis of recent bridge failures in the United States. *Journal of Performance of Constructed Facilities*, 17(3), pp.144-150.

Wu, T. R., Wang, H., Ko, Y. Y., Chiou, J. S., Hsieh, S. C., Chen, C. H., ... & Chuang, M. H. (2014). Forensic diagnosis on flood-induced bridge failure. II: Framework of quantitative assessment. *Journal of Performance of Constructed Facilities*, 28(1), 85-95.

CHAPTER 5

GENERAL CONCLUSIONS AND FUTURE RESEARCH RECOMMENDATIONS

Understanding the interaction of flood flow with bridge superstructures is crucial for estimating the hydrodynamic forces on bridges. The two most important aspects to consider are the flow parameters and the geometry of the bridge, the effects of which were investigated in this study in terms of drag, lift, and moment coefficients. The effects of debris and substructures on the hydrodynamic forces of bridge superstructures were also investigated. Small-scale bridge models were developed to simulate typical geometrical and flow conditions in the laboratory, and load and torque cells were used to measure the total streamwise force, vertical force, and overturning moment for bridge superstructures; force equations were used to calculate the drag, lift, and centroidal moment coefficients. Hydrodynamic forces and moment coefficients were examined with respect to the proximity ratio, inundation ratio, Froude number, aspect ratio, blockage ratio, and girder shapes. PIV techniques were employed to visualize the mean flow field around the submerged decks. The following section concludes the findings and achievements of this research and offers suggestions and recommendations for future work.

5.1 CONCLUSIONS

The following findings correspond to the objectives of this study:

- The proximity ratio experiment conducted on typical I-girder (*Br*=0.18) bridge superstructures confirmed that the position of the bridge deck in relation to the streambed greatly influences the force and moment coefficients. C_L, C_M and C_D were minimally affected by proximity ratios of 3 or greater.

- A reduction in the wake area or flow separation region resulting from an increase in *Fr* reduced the hydrodynamic force coefficients (C_D and C_L) in the transition region ($h^* = 1$), but a scatter in the moment coefficient (C_M) was observed. The C_D, C_L, and C_M were significantly affected by the inundation ratio, especially when the inundation ratio changed from partially submerged to fully submerged, i.e., from 0.75 to 1.25.
- Greater aspect and blockage ratios resulted in larger variations in the relative water depth between the areas upstream and downstream of the deck, which indicated a pressure imbalance on the deck and produced higher drag force coefficients (C_D). I-girders with similar geometric and flow parameters showed greater drag force and C_D than the box beams. The lift coefficient (C_L) varied slightly with a change in the aspect ratio (*Ar*), where more negative C_L values were observed for a smaller *Ar*. The shape of the girder/beam had no significant impact on the C_L, due to similar dynamic pressure variations on the upper and lower sides of the deck; however, the C_L varied with changes in the *Br*. A narrow deck (Ar = 4.5) produced a higher moment coefficient (C_M) around the center of gravity of the superstructure due to the combined actions of the drag and lift forces, with slight dominance by the lift force. The blockage ratio showed no significant variation for C_M; however, the box beam produced greater C_M than the I-girder, due to the combined actions of the drag and lift coefficient on the box beam deck.

- Flow characteristics around submerged I-girder bridge models were investigated for *Fr* of 0.20 and 0.34 of the approaching flow and h^* of 1. Although the dimensions of the wake regions were similar for both *Fr*, the vortex generated on the downstream side of the deck by the lower *Fr* (= 0.20) increased the C_D slightly. The differences in the length of the flow separation at the top and bottom of the deck were higher for *Fr* of 0.34, resulting in a larger C_L.
- For all h^* values, the flow visualization images showed the presence of separation regions and formation of vortices. However, low levels of submersion ($h^* = 0.5$) resulted in fewer formations below the deck and between the girders than high levels of submersion ($h^* = 1$ and 1.5). For $h^* = 1$, the drag coefficients were minimum, as was the width of the wake (d^*). In contrast, the C_D and d^* increased for h^* of 0.50 and 1.50 from h^* of 1.0. As h^* increased, the dimensionless separation length (R^*) and C_L decreased for $h^* \geq 1$. For $h^* < 1$, the magnitude of the C_L and R^* was smaller as fewer circulated region formed to generate suction below the deck.
- The variations in the mean flow field were more significant for changes in the blockage ratio (*Br*) than in the aspect ratio (*Ar*) and girder shape. The hydrodynamic force coefficients, C_D and C_L, as well as the dimensionless d^* and R^*, increased as the *Br* increased. As *Ar* increased, the C_D increased, but d^* remained almost unchanged. The vortex activity between the girders contributed to an increase in drag for the wider deck (*Ar* =7.9*)*; however, the C_L and the R^* decreased for the wide deck (*Ar* =7.9). It was also found that C_D and the d^* were higher for I-girders than for box beams.

- The presence of flat plate debris increased C_D significantly, while the wedge debris reduced the negative C_L. The C_M of the flat plate debris did not vary significantly from the C_M of

the superstructure-only bridge model; however, the wedge debris significantly increased the C_M (clockwise moment), making the bridge more vulnerable to failure.

- The presence of substructure(s) (i.e., piers and bent caps) increased the C_D values and decreased the C_L for fully submerged conditions, but no specific pattern was observed in the C_M change. The effects of substructures on C_D and C_L were attributed to the reduction of the fluid-structure interaction area due to the additional flow blockage caused by the piers and bent caps.
- The combined effects of debris and substructures increased the C_D and decreased the C_L and C_M. The variations in the C_D and C_L can be attributed to the greater wake region below the deck that was caused by the presence of the substructure. The superstructure-debris-substructure model generated greater (more negative) C_M compared to the superstructure-only model, which can be attributed to a shift in the location of the line of action of forces to the upstream side, due to the addition of wedge debris and the substructures.

5.2 RECOMMENDATION FOR FUTURE RESEARCH

- Due to the limitations of the experimental facility, the *Fr* number was restricted to 0.34, which is considered as subcritical flow. Further investigations could be extended to supercritical flow regions by using a larger flow capacity or numerical modeling techniques. The hydrodynamic forces and moments obtained from the physical experiments in this research can be used to validate the numerical modeling, and the numerical modeling can be used to upscale the results of the experiments to field scale.

- Experiments should be conducted on other shapes of girders or beams (i.e., slab beams, U-beams, flat beams, etc.) to investigate their effect on force and moment coefficients since it has been proven that are greatly influenced by the shape of girders and beams.
- The PIV experiments focused on submergence regions ranging from 0.50 to 1.50, which are the most critical regions for the generation of hydrodynamic forces and the interactions of flood water with river crossing bridges. However, further research could be conducted on a wider wide range of submergence ratios to develop a more comprehensive relationship between the geometry of a wake region and the hydrodynamic force coefficients for actual bridge superstructures.
- The significant increase in velocity observed below the deck may have a significant effect on the riverbed scouring and needs to be considered in future research to understand its effect on the hydrodynamic forces of bridge superstructures.
- This study did not investigate the effects of storm surges on the hydrodynamic forces of coastal bridges, but a combination of currents and waves can be observed in many coastal and oceanic locations. Their interaction creates complex and potentially hazardous situations, and future research could examine how they affect a bridge's vulnerability.
- This study only examined the effects of two generalized shapes of debris. Other types of debris could be identified and their impacts on hydrodynamic forces and moments examined. The present study only considered the force generated by accumulated debris at the bridge upstream, and additional research is needed to determine the impact of floating debris on bridge superstructures.

APPENDIX A

MEASUREMENT UNCERTAINITY

Load and Torque Cells:

The manufacturer of the 3A120 3-AXIS Force load cell used in this research states that the accuracy class is ±0.15%, which means that effects such as creep, non-linearity, and hysteresis cause the measured force to deviate from the actual force by no more than 0.15% of the measured value at the load cell. This corresponds to a maximum error of 0.15 N for each axis of the 3-axis load cell when the load cell reaches its capacity, which is 100 N. Similarly, the manufacturer of the MRT2 miniature torque transducer, which can measure torque within the range of 0 – 10Nm, warns that it could produce an error as high as ±0.02%, resulting in a maximum error of 0.002 Nm at its full capacity of 10 Nm. The precision of the load cells was also double checked by putting the known weight on the load cell, performing 17 measurements, and comparing them with the load recorded at the cell. Fig. A.1 and Table A.1 illustrate the statistical relations between a measured load at the cell and a load inserted by known weights.

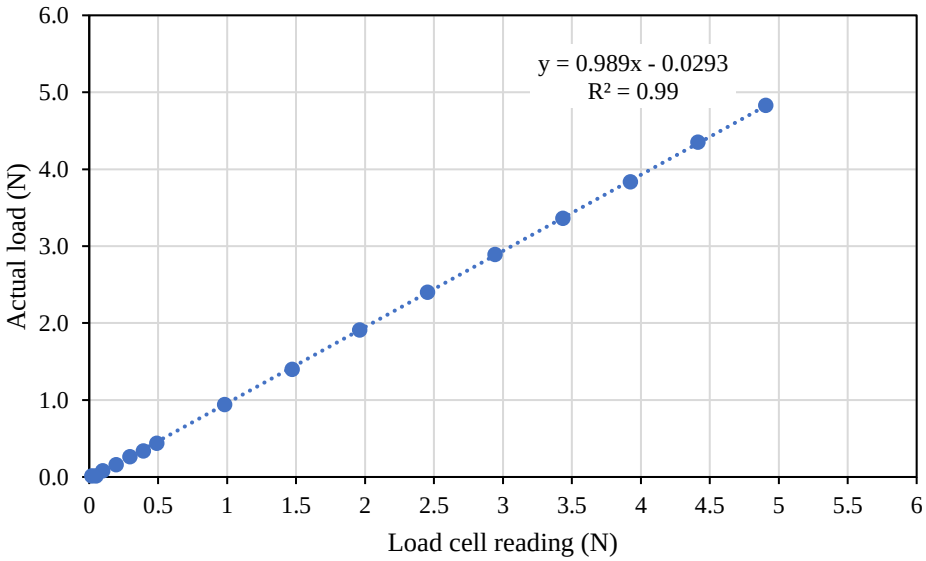

Fig. A.1 Actual load vs. load cell readings

Table A.1 Regression Statistics for Load Cell Accuracy

Regression Statistics	
Multiple *R*	0.99
R^2	0.99
Adjusted R^2	0.99
Standard Error	0.0095
No. of Observations	17

Velocity and Discharge:

The velocity range for the SonTek ADV is ± 0.001 – 4.5 m/s and the accuracy is ±1% of the measured velocity. This study used an ultrasonic Sono-Trak flowmeter that is capable of measuring flow with an accuracy of ± 0.5%.

Water Level Measurement

The water depth was determined by a pointy gauge located upstream of the bridge section at the centerline of the flume and was double-checked by sticky gauge attached to the flume wall. The

water depth at the centerline of the flume and the side of the flume wall was estimated at several locations upstream and downstream of the deck. It is estimated an error of ± 0.002-m could occur.

Froude number

The Froude number, *Fr*, can be calculated by using the following equation:

$$Fr = \frac{V}{\sqrt{gh_u}} = \frac{Q/Bh_u}{\sqrt{gh_u}} \quad \text{A.1}$$

where Q is total discharge, B is the width of the flume, and h_u is upstream flow depth.

The estimated error in *Fr* can be calculated according to the equation provided by the International Organization of Standardization-GUM (1995) (Malavasi and Guadagnini 2003). If X is a quantity depending on y_i parameters, the uncertainty of X can be evaluated as:

$$uX = \sqrt{\sum_i \left(\frac{\partial x}{\partial y}\right)^2 uy_i{}^2} \quad \text{A.2}$$

Using this method, the estimated error in *Fr* can be calculated as:

$$u(Fr) = \sqrt{\left(\left|\frac{\partial Fr}{\partial Q}\right| u(Q)\right)^2 + \left(\left|\frac{\partial Fr}{\partial B}\right| u(B)\right)^2 + \left(\left|\frac{\partial Fr}{\partial h_u}\right| u(h_u)\right)^2} \quad \text{A.3}$$

where $u(Q)$ is the error of the device measuring the flow and determined to be approximately $\pm$ 0.5% of the measured flow; $u(B)$ is the error in the width measurement, and the width of the flume was measured quite accurately; 304.8 $\pm$ 2 mm. g was assumed to exactly 9.81 m/s^2 without error.

Table A.2 Measured Values and Errors for Flow Parameters

Parameter	Measured value	Error
Q	0.016 m^3/s	$\pm 8.13\times10^{-7}$ m^3/s
B	304.8 mm	± 2 mm
h_u	19.4 cm	± 0.2 cm

Using Eqn. A.1 and A.3, the *Fr* number and the error in *Fr* estimation can be calculated as:

Fr = 0.20 and *u(Fr)* = 0.001.

Another source of measurement errors could be the vibrations of the flume caused by the pump. Fig. A.2 illustrates the order of precision for the recorded force data at the load cell, where every column represents the mean force value for two minutes of measured data. The consistency of the measured data was plotted by representing the mean force data for three separate time intervals at the same flow conditions. The difference in the data was only about 0 to 3%.

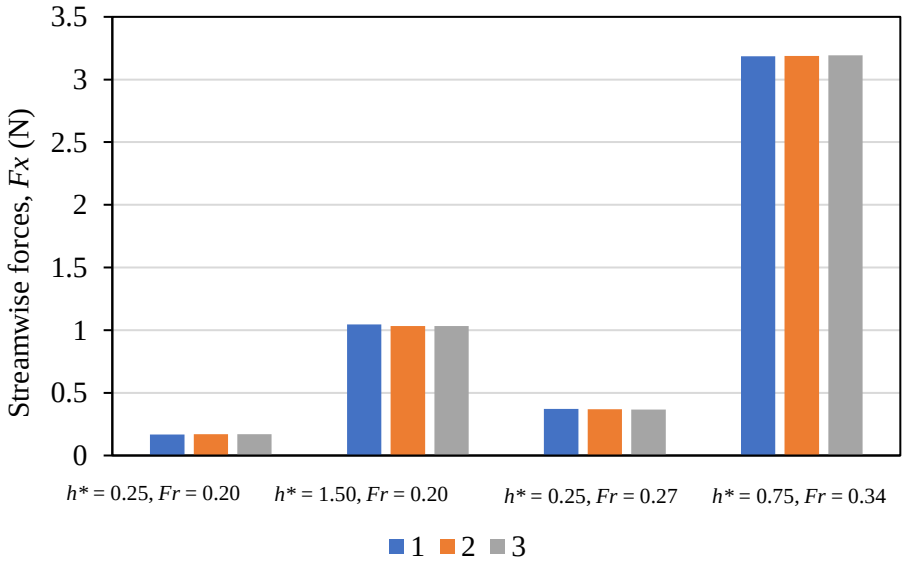

Fig. A.2 Streamwise forces on a bridge deck at different time intervals

APPENDIX B

DETAILS OF BRIDGE MODEL

The bridge models were built at a scale of 1:50 of the bridge prototypes and were made of aluminum because it has a weight that is similar to that of reinforced concrete. The cross-sections of the superstructures are shown in Figs. B1 to B10, and the dimensions of the TX54 and TX28 I-girders and 5B28, 4B28 and T221 railings are illustrated below.

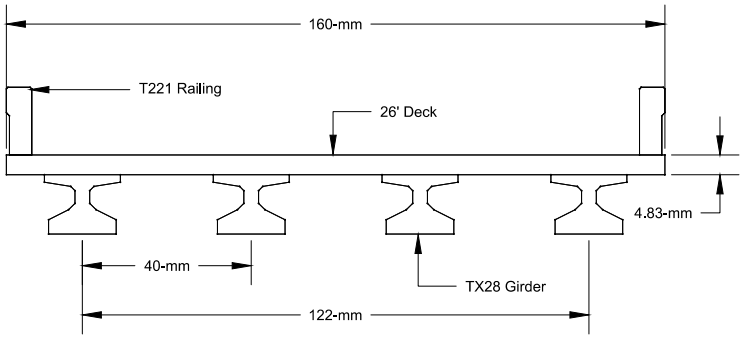

Fig. B.1 Schematic of the bridge model for *Ar* = 4.5 (four TX-28 girders) and *Br* = 0.18

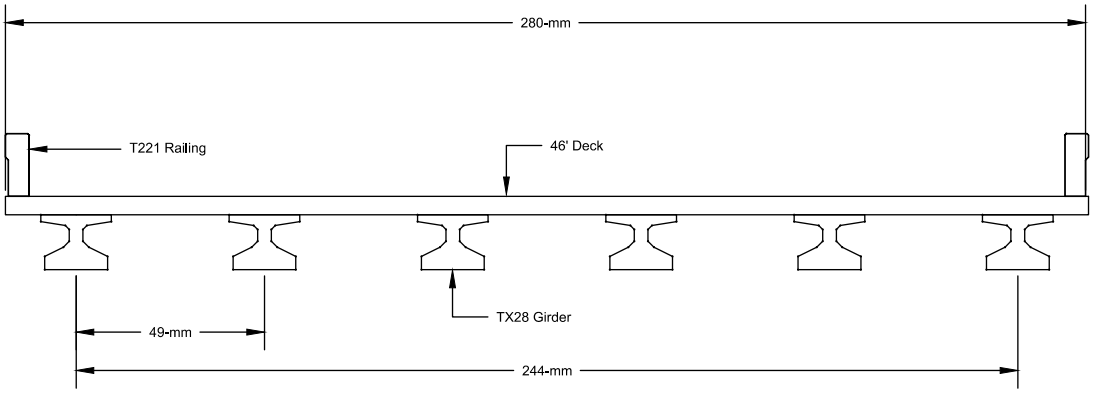

Fig. B.2 Bridge Model for *Ar* = 7.9 (six TX-28 girders) and *Br* = 0.18

Table B.1 Model and Prototype Dimensions for Model *Ar* = 4.5 and *Ar* = 7.9

Attribute	Prototype Dimension (cm)	Model Dimension (mm)
Deck thickness (*s*)	24	4.8
Bridge length (*L*)	1510	302
Width (*W*) - 26 ft deck	800	160
Width (*W*) - 46 ft deck	1400	280
Girder height	70	14
Railing height	80	16
Superstructure height (*S*)	174	34.8

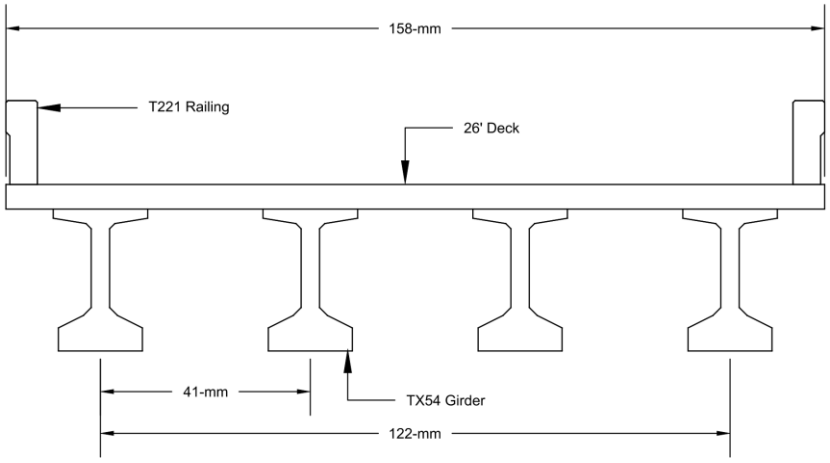

Fig. B.3 Schematic of the bridge model for *Ar* = 4.5 and *Br* = 0.20

Table B.2 Model and Prototype Dimensions for *Ar* = 4.5 and *Br* = 0.20

Attribute	Prototype Dimension (cm)	Model Dimension (mm)
Deck thickness (*s*)	24	4.8
Bridge length (*L*)	1510	302
Width (*W*) - 26 ft deck	800	160
Girder height	135	27
Railing height	80	16
Superstructure height (*S*)	215	43

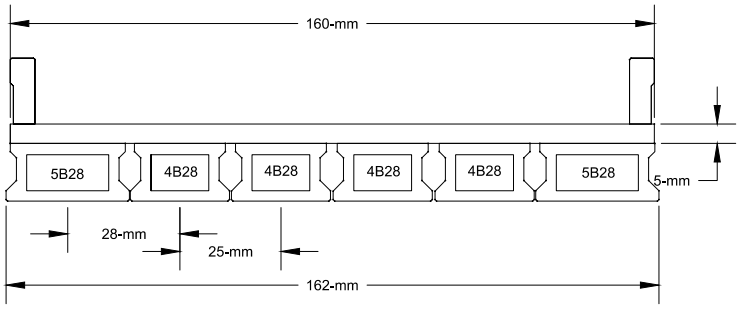

Fig. B.4 Schematic of the bridge model for box beam *Br* = 0.18 and *Ar* = 4.5

Table B.3 Scale Dimensions for Bridge Model (*Br* = 0.20)

Attribute	**Prototype Dimension (cm)**	**Model Dimension (mm)**
Deck thickness (*s*)	24	4.8
Bridge length (*L*)	1510	302
Width (*W*) - 26 ft deck	800	160
Beam height	70	14
Railing height	32	16
Superstructure height (*S*)	155	31

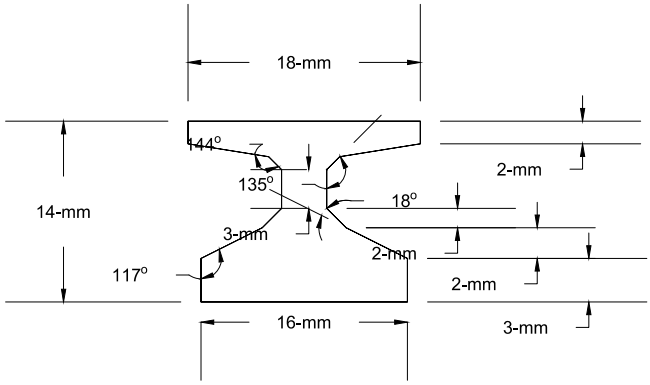

Fig. B.5 Details of the TX28 girder

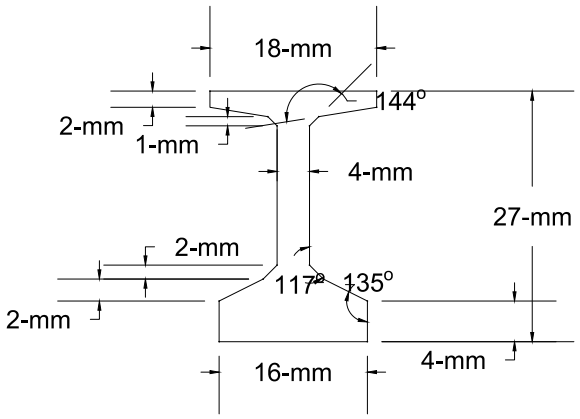

Fig. B.6 Details of the TX54 girder

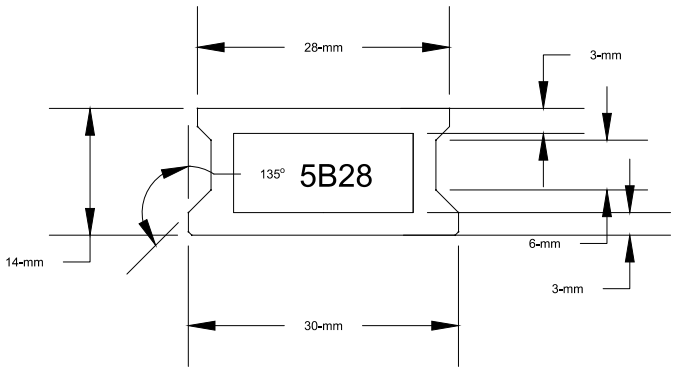

Fig. B.7 Details of the TX54 girder

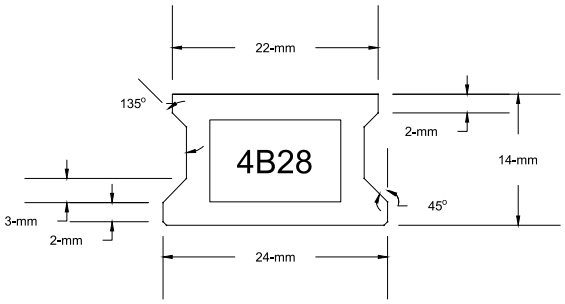

Fig. B.8 Details of 4B28 box beam

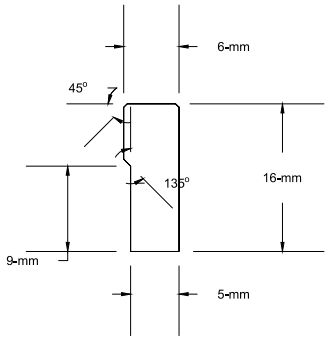

Fig. B.9 Details of T221 railing

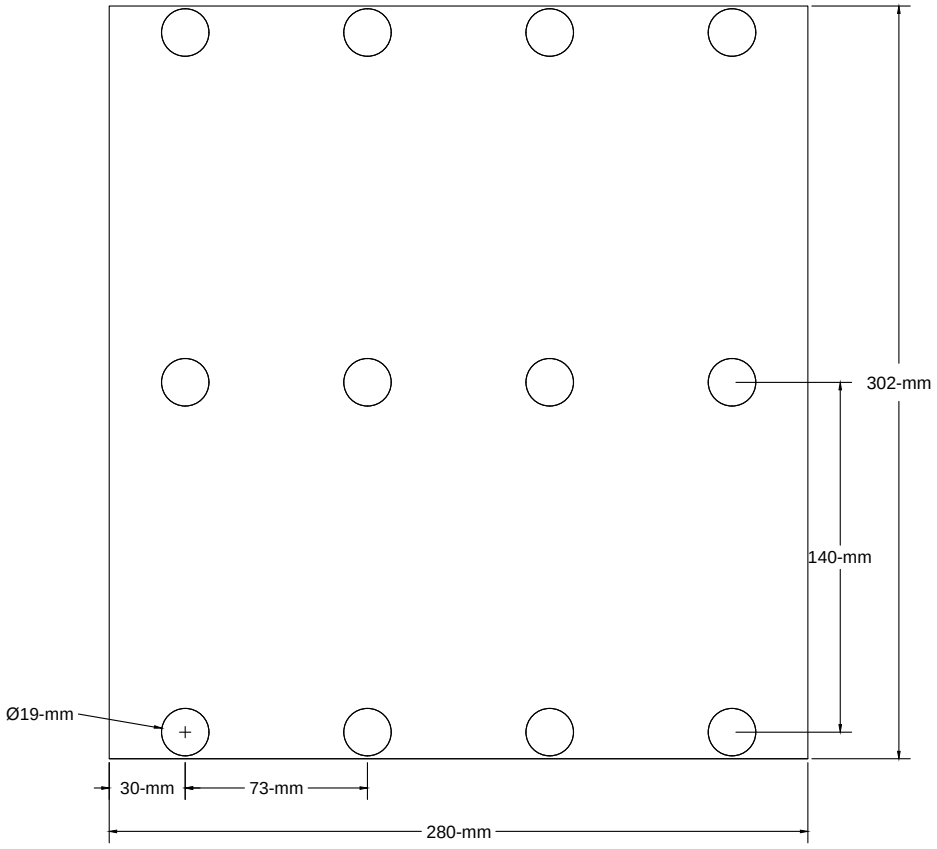

Fig. B.10 False bottom layout

APPENDIX C

SAMPLE CALCULATIONS

A sample calculation is provided below for an inundation ratio of h^* of 1.0 and *Fr* of 0.20.

Table C.1 Bridge Model Details (*Ar* = 4.5 and *Br* = 0.18)

Attribute	Prototype Dimension (m)	Model Dimension (m)	Model Dimension (in)
Deck thickness	0.24	0.0048	0.19
Deck length (*L*)	15	0.302	11.9
Deck width (*W*)	8	0.16	6.24
Girder height	0.7	0.014	0.56
Railing height	0.8	0.016	0.64
Low chord elevation (h_b)	8	0.16	6.24
Superstructure height, *s*	1.75	0.035	1.39

Table C.2 Flow Data

Attribute	Value
Discharge (m^3/s)	0.016
Upstream water depth, h_u (m)	0.194
Average velocity, *V* (m/s)	0.276
Froude number	0.20

Table C.3 Supporting Plate Dimensions

Attribute	Value (in)	Value (m)
Vertical plate height	5.5	0.14
Plate thickness	0.1875	0.005
Length of the plate	3	0.08

The following calculation steps are presented for h^* of 1.0 and *Fr* of 0.20.

Step 1: Water depth and bridge height for h of 1.0*

Inundation ratio, $h^* = \frac{(h_u - h_b)}{s}$

h_u = upstream water depth (m) = 0.194

h_b = bridge low chord elevation (m) = 0.159

s = superstructure height (m) = 0.035

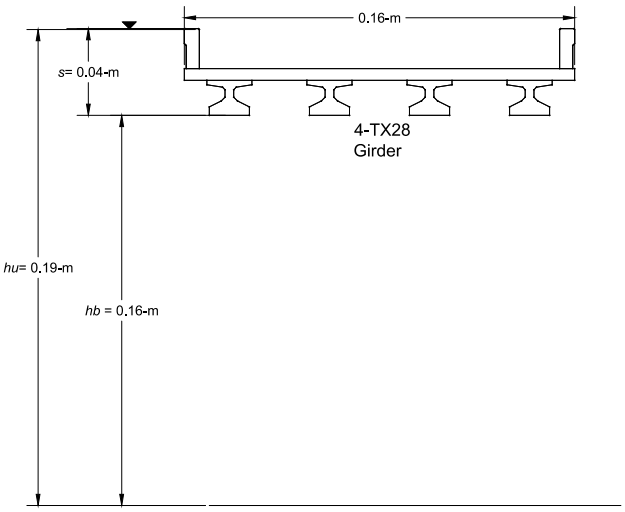

Fig. C.1 Schematic of bridge submergence for $h^* = 1$

Step 2: Calculate the submerged area of the bridge model for buoyant force calculation.

Fig. C.2 indicates the submerged portion of the bridge superstructure and the vertical plate.

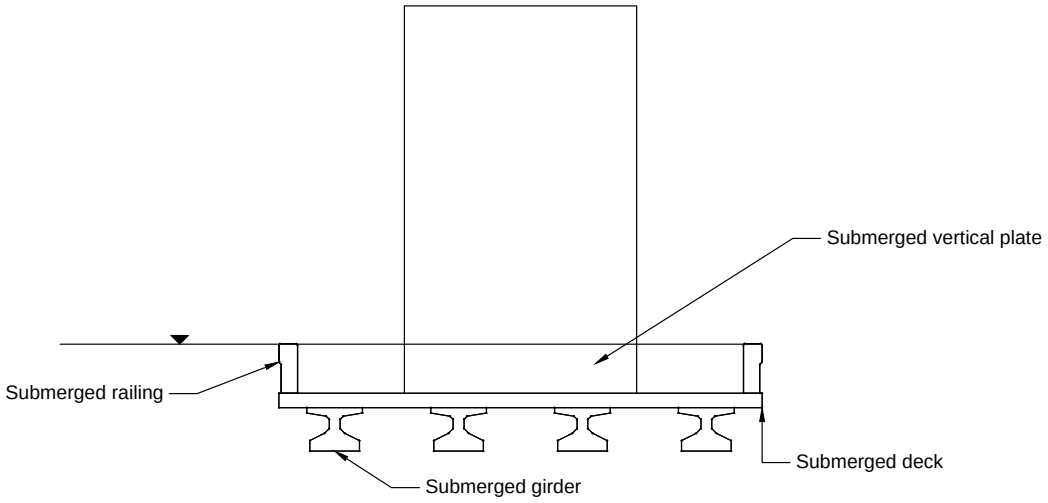

Fig. C.2 Submerged portion of the bridge models and vertical plates

The total submerged superstructure area can be calculated as:

Total submerged superstructure area, A*ss* = 4×Sub. girder area (*Ag*) + Sub. deck area (*Ad*) + 2×Sub. railing area (*Ar*)

Sub. girder area, *Ag* (m^2) = 1.51×10^{-4}

Sub. deck area, *Ad* (m^2) = 9.15×10^{-5}

Sub railing area, Ar (m^2) = 7.55×10^{-4}

Total submerged superstructure area A_{ss}(m^2) = $4\times1.51\times10^{-4} + 9.15\times10^{-5} + 2\times7.55\times10^{-4} = 1.54\times10^{-3}$

Submerged area for the vertical plate (A_V) can be calculated as:

For h^* = 1, the height of the submerged plate normal to flow (Fig. C2) = 0.019 m

$A_V = 2 \times$ height of the submerged plate (normal to flow) $\times$ thickness of the plates

A_V (m^2) =$2\times0.019\times0.005=1.85\times10^{-4}$

Buoyant Force - F_B (N)

Volume of the submerged superstructure, V_{ss} (m^3)

V_{ss}=A_{ss} $\times$ length of the Bridge = $1.54\times10^{-3}\times0.302 = 4.6\times10^{-4}$

Volume of the submerged vertical plate V_{sp} (m^3)

V_{sp}=A_V $\times$ length of the plate in the flow direction $=1.84\times10^{-4}\times0.076 = 1.4\times10^{-5}$

The buoyant force can be calculated as,

$F_B = \rho g V$

V =Total volume of the submerged elements (m^3) = V_{ss} + V_{sp}

$F_B = 9810 \times (4.6\times10^{-4}+1.4\times10^{-5})$

$F_B = 4.70$ N

Step 3: Calculation of hydrostatic force - F_h (N)

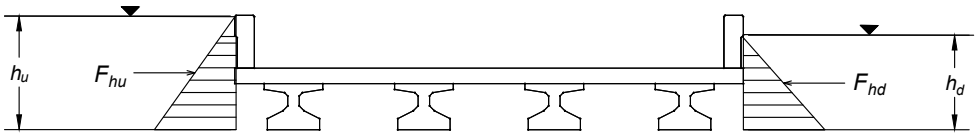

Fig. C.3 Schematic of the hydrostatic force at h^* = 1

The total hydrostatic component of force on the upstream face can be calculated as:

$F_{hu} = \gamma h_{cu} A_{hu}$

F_{hu} = hydrostatic force on the upstream side of the railing

h_{cu} = vertical distance from the water surface to the centroid of the area, A_{hu}

h_u = upstream submerged superstructure depth (m)

$h_{cu} = (h_u - h_b) - 0.5s$

$h_u(m) = 0.197$

$h_b(m) = 0.159$

$h_{cu} = 0.197 - 0.159 - 0.5 \times 0.035$

$h_{cu} = 0.0205\ m$

$A_{hu} = sL$ (Area for fully submerged upstream face of the deck)

$F_{hu} = 9810 \times 0.0205 \times 0.035 \times 0.302$

F_{hu}= 2.16 N

The total hydrostatic component of force on the downstream face can be calculated as:

$F_{hd} = \gamma h_{cd} A_{hd}$

$h_{cd}(m) =$ vertical distance from the water surface to the centroid of the area A_{hd}

$A_{hd}(m^2)$ = projected area of the submerged superstructure on the downstream side

h_d(m) = downstream submerged superstructure depth

$$h_{cd} = \frac{h_d - h_b}{2}$$

$A_{hd} = (h_d - h_b)L$ (area for partially submerged downstream face of the deck)

The downstream water level determined from observation, h_d = 0.193 m

$$F_{hd} = \frac{\gamma h_{cd}}{2} h_{cd} L$$

$$F_{hd} = \frac{\gamma (h_d - h_b)^2}{2} L$$

$$F_{hd} = \frac{9810 \times (0.193 - 0.159)^2 \times 0.302}{2}$$

$F_{hd} = 1.71\ N$

Step 4: Drag force calculation on the vertical plate

Viscous drag calculation of the vertical plate adapted from Jempson (2000):

$F_{DV} = 2.656 d_p \rho \sqrt{V^3 \vartheta l}$

$d_p =$ depth of the wetted plate (m) = $h_u - h_b -$ girder height $-$ deck thickness

= 0.194 - 0.159 - 0.014 - 0.005 = 0.016 m

ϑ = the kinematic viscosity (m^2/s) = 1.05×10^{-6}

$l =$ length of the plate in the direction of the flow (m) = 0.076

V = average approach velocity (m/s) = 0.276

$F_{DV} = 2.656 d_p \rho \sqrt{V^3 \vartheta l}$ = $2.656 \times 0.016 \times 1000 \sqrt{0.276^3 \times 1.05 \times 10^{-6} \times 0.076}$

F_{DV} = 1.77×10^{-3} N

Pressure drag calculation on the vertical plate adapted from Jempson (2000)

$F_{DP} = 0.5\ C_p \rho V^2 A_v$

$C_p = 1$ (Assuming pressure drag on the plates is typically 1% of the measured drag force)

A_v= Projected wetted area of the submerged vertical plate (m^2) = 1.55×10^{-4}

$F_{DP} = 0.5 \times 1 \times 1000 \times 0.276^2 \times 1.55 \times 10^{-4}$

$F_{DP} = 0.0069$ N

Step 5: Hydrodynamic drag force - F_D (N) and drag coefficient on the deck

The drag force on the bridge deck can be calculated using the following formula:

$F_D = F_X - F_{DV} - F_{DP} - (F_{hu} - F_{hd})$

$F_D(\mathrm{N}) =$ Drag force

$F_x(\mathrm{N}) =$ Streamwise force in flow direction and the other forces are defined before

$F_x(\mathrm{N}) = 0.86$

$F_D = 0.86 - 0.0017 - 0.0069 - (2.16 - 1.71)$

$F_D = 0.401$ N

Drag coefficient (C_D)

$$C_D = \frac{2F_D}{\rho V^2 A}$$

A = projected area on the bridge superstructure normal to flow direction (m^2)

$A = (h_u - h_b)L$

$$C_D = \frac{2 \times 0.401}{1000 \times 0.276^2 \times (0.194 - 0.159) \times 0.302}$$

$C_D = 0.99$

Step 6: Hydrodynamic lift force F_L (N) and lift coefficient (C_L) on the deck

$F_L = F_y - F_B$

F_L(N) = Lift force (Positive upwards)

F_y(N) = Vertical force readout by the loadcell

F_B(N) = Buoyant force

$F_L = 1.53 - 4.70$

$F_L = -3.17$ N

Lift coefficient (C_L)

$$C_L = \frac{2F_L}{\rho V^2 A}$$

A = Projected area on the bridge superstructure (m^2) (along the flow direction)

$A = WL$

$$C_L = \frac{2 \times (-3.17)}{1000 \times 0.276^2 \times 0.159 \times 0.302}$$

$C_L = -1.74$

Step 7: Moment coefficient calculation and correction of the measured moment at the torque cell

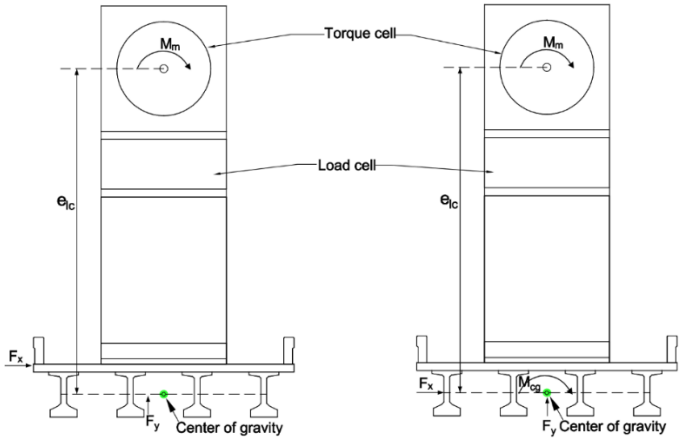

Fig. C.4 Free-body diagram of the scale model for calculating the centroidal moment (*Mcg*) from the measured moment (*Mm*) at the torque cell

$M_{cg} = M_m - F_x e_{lc}$

M_{cg}(Nm) = Moment measured around the center of gravity (positive clockwise)

M_m (Nm) = Moment readout by loadcell = - 0.23

F_x (N) = Streamwise force = 0.86

e_{lc} (m) = Moment arm between the center of gravity of the bridge and the center of the load cell

e_{lc} = Distance from the center of the torque cell to the girder soffit – centroid of the superstructure from the girder soffit

$e_{lc} = 0.260 - 0.014 = 0.246\ m$

$M_{cg} = 0.86 \times 0.246 - 0.23$

M_{cg} = - 0.02 Nm (positive clockwise)

Moment Coefficient (C_M)

$$C_M = \frac{-2M_{cg}}{\rho V^2 L W^2}$$

$$C_M = \frac{2 \times (-1) \times (-0.02)}{1000 \times 0.276^2 \times 0.302 \times 0.158^2}$$

$C_M = 0.08$ (Positive moment coefficient means counterclockwise moment)